REPORT No. TRC-EM-CAB-0001

ADVANCED ELECTROMAGNETIC METHODS FOR AEROSPACE VEHICLES

Final Report
(January 1, 1990 - December 31, 1999)

by
Constantine A. Balanis
Anastasis Polycarpou
Craig R. Birtcher
Stavros Georgakopoulos
Dong-Ho Han
Gerasimos Ballas

Sponsored by

National Aeronautics and Space Administration (NASA)
Langley Research Center (LaRC)
Hampton, VA 23681
Grant No. NAG-1-1082

Prepared by

Telecommunications Research Center
College of Engineering and Applied Sciences
PO Box 877206, Tempe, AZ 85287-7206

Contents

I. EXECUTIVE SUMMARY

The imminent destructive threats of *Lightning* on helicopters and other airborne systems has always been a topic of great interest to this research grant. Previously, the lightning induced currents on the surface of the fuselage and its interior were predicted using the finite-difference time-domain (FDTD) method as well as the NEC code. The limitations of both methods, as applied to lightning, were identified and extensively discussed in the last meeting. After a thorough investigation of the capabilities of the FDTD, it was decided to incorporate into the numerical method a subcell model to accurately represent current diffusion through conducting materials of high conductivity and finite thickness. Because of the complexity of the model, its validity will be first tested for a one-dimensional FDTD problem. Although results are not available yet, the theory and formulation of the subcell model are presented and discussed here to a certain degree.

Besides lightning induced currents in the interior of an aircraft, penetration of electromagnetic fields through apertures (e.g., windows and cracks) could also be devastating for the navigation equipment, electronics, and communications systems in general. The main focus of this study is understanding and quantifying field penetration through apertures. The simulation is done using the FDTD method and the predictions are compared with measurements and moment method solutions obtained from the NASA Langley Research Center.

Cavity-backed slot (CBS) antennas or slot antennas in general have many applications in aircraft-satellite type of communications. These can be flushmounted on the surface of the fuselage and, therefore, they retain the aerodynamic shape of the aircraft. In the past, input impedance and radiation patterns of CBS antennas were computed using a hybrid FEM/MoM code. The analysis is now extended to coupling between two identical slot antennas mounted on the same structure. The predictions are performed using both the hybrid FEM/MoM and the FDTD NEWS code. The results are compared with each other as well as with measurements performed in the ElectroMagnetic Anechoic Chamber (EMAC) of ASU. In addition to self and mutual impedances versus frequency, the comparisons include mutual coupling S_{12} as a function of distance for various slot orientations.

The FDTD NEWS code was upgraded from second-order accurate in time and

space, e.g. FDTD(2,2), to second-order accurate in time and fourth-order accurate in space, e.g. FDTD(2,4). It was shown in the previous report that the higher-order FDTD scheme is more accurate for the same discretization size and exhibits smaller dispersion errors. This was illustrated for a one-dimensional wave propagation problem. In this report, an in-house developed three-dimensional version of FDTD(2,4) is used to predict radiation patterns of electrically large helicopter problems. Specifically, the radiation patterns of a monopole on the NASA scale helicopter model at 9.18 GHz are predicted and compared with the FDTD(2,2) NEWS code and measurements.

A new iterative algorithm is formulated in conjunction with the hybrid FEM/MoM approach to solve effectively for the coupling parameters of multiple cavity-backed slot antennas on the surface of a platform. Each radiating element is solved independently to find the governing field distribution in the aperture of the cavity. The interaction among these cavities is accounted for through an iterative procedure which continuously updates the fields in each finite element domain until convergence is achieved. The validity of the method is tested by calculating the mutual coupling between two similar cavity-backed slot antennas mounted on an infinite ground plane. This approach is not only accurate but also extremely powerful and efficient both in terms of memory storage and solution time.

The hybridization of FEM with high-frequency methods such as the physical optics (PO) has been a focus of this project for the last few years or so. In this report, the FEM is formulated for two-dimensional scattering and radiation problems in conjunction with either absorbing boundary conditions or the boundary integral approach. The validity of the method has been tested against MoM solutions. For radiation problems, the finite element domain is coupled (using a one-way interaction) to a physical optics formulation to compute scattered fields by a nearby large object.

Spectral methods are applied for the first time to the solution of one-dimensional problems. The great potential of these methods in the area of electromagnetics is demonstrated through numerical experimentation. Conclusions are obtained by comparing results with the standard FDTD algorithm. Furthermore, the PML concept has been applied to spectral methods to simulate open-space propagation problems.

II. INTRODUCTION

The major research topics addressed in this report are the ones which have been identified and recommended by the Advisory Task Force of the Advanced Helicopter Electromagnetics (AHE) program. Although some of these topics provide a continuation of previous work, emphasis was placed on research areas that are of special interest to the program. Some of these subjects were brought to our attention in the Annual Conference held at the Boeing plant in Philadelphia, PA, on May 26-27, 1999. The main topics of focus in this report are the following:

- Lightning and its numerical modeling
- Field penetration through apertures
- Analysis of cavity-backed slot antennas
- Mutual coupling of cavity-backed slot antennas
- Higher-order FDTD schemes
- Hybrid methods
- Spectral methods

Each of the above topics is addressed in sequence in this document, reporting on progress already made primarily during the period after the May 1999 meeting and outlining future work to be accomplished.

The topic of lightning is now being studied in a more systematic way. Two different numerical methods have been used to predict the diffusion of currents in the interior of a conducting enclosure of finite skin thickness and conductivity. One of these two methods was the NEC code which models the structure using a wire-grid model. The thickness of the walls was taken into account implicitly through the radius of the wires. Although the results predicted by NEC agreed well with results obtained from an independent study performed by Dr. Jack Nachamkin at Boeing in Philadelphia, the NEC analysis does not account for the *skin depth* of the wall, which is known to be a function of frequency and conductivity. A more accurate approach to predict the diffusion of currents in the interior of a conducting structure is to use a more robust

technique such as the FDTD method. The FDTD method is accurate provided the discretization inside the thickness of the walls is adequate enough. Unfortunately, it was determined in previous reports that the cell size of the grid inside the conductor has to be extremely small to achieve accuracy in the solution. In addition, the larger the conductivity of the wall, the smaller the cell size should be. This will increase the computational domain substantially, therefore limiting the use of the FDTD to only small problems.

In this report, the FDTD scheme is augmented by introducing a subcell model to accurately represent field and current variation inside the thickness of the walls. This subcell model assumes a one-dimensional variation of the fields of the slab in a direction normal to the wall. This assumption is valid provided, first, the thickness of the wall is much smaller than its radius of curvature and its transversal direction and, second, the conductivity of the material is sufficiently high so that the waves propagate in a direction normal to the wall. Because of its complexity, this model will be first implemented for a one-dimensional problem. At this stage, numerical results are not available; thus, emphasis will be directed toward the formulation and the theory behind the subcell model.

Penetration of field intensity into the the interior of an aircraft through apertures is an EMI issue with great relevance to the AHE project. When an aircraft is flying near high-power transmitting antennas, the external threat might couple through apertures with sensitive control equipment thereby resulting in severe malfunctioning. The ability to predict the amount of power that couples through an aperture at a given frequency is of great interest to us. In this report, the FDTD method is used to compute field penetration inside a moderately sized cavity with three aperture configurations: a single large aperture, two large apertures, and a single small aperture. The object is excited with a normally incident Gaussian pulse with spectrum up to 1 GHz. The electric field shielding, which is the relation between the field in the interior of the box relative to the field outside the box, is plotted for all three cavity configurations as a function of frequency. The FDTD predictions are compared with numerical data obtained using the method of moments. Although at first this problem might seem trivial for a method such as the FDTD, there are for sure numerical difficulties associated with the highly resonant nature of the cavity as

well as the electrically small size of the aperture. These problems can be alleviated by introducing a loss mechanism into the computational domain to accelerate the decay of the late-time fields.

Antenna technology as applied to helicopters was always of special interest to the AHE project. During the last few years, emphasis was placed on the numerical analysis of cavity-backed slot (CBS) antennas which can be conveniently flushmounted on the surface of a fuselage thereby retaining the aerodynamic profile of the aircraft. Prediction of input impedance and radiation patterns of a single CBS antenna on an infinite ground plane was achieved through a hybridization of the FEM and the spectral/spatial domain method of moments. This hybridization offers numerous advantages since the free-space region does not need to be descritized; this saves memory space and speeds up computational time. The FDTD is also used in this report to predict the input impedance of a single CBS antenna. Although this problem may seem trivial, it is actually difficult since the time-domain fields propagating inside the cavity decay with a very slow rate. As is discussed in this report, the source modeling has been augmented with a source resistance which helps dissipate the time-domain fields inside the highly resonant structure.

Both the hybrid FEM/MoM method and the FDTD method have then been applied to compute the mutual coupling of two identical CBS antennas mounted onto a ground plane. For such a problem, the FDTD has a severe drawback compared to the hybrid approach. Using the FDTD, the free-space exterior-to-the-cavities region needs to be discretized and terminated properly with some type of absorbing boundary conditions. This approach creates large computational domains which, in turn, generate large errors primarily due to dispersion. The hybrid FEM/MoM approach, on the other hand, does not discretize the exterior region; thus, placing the two CBS antennas farther away presents no significant challenges to the method. Predictions on mutual coupling using the hybrid FEM/MoM approach are shown versus frequency and distance and compared with measurements performed in the EMAC facility of ASU.

This hybrid FEM/MoM approach was then improved to further speed up the computational time as well as to further reduce memory requirements. Specifically, instead of treating the two CBS antennas as a tightly coupled system which can be

solved directly using the hybrid method, they are rather perceived as two non-coupled antennas placed in close proximity to each other. For mutual coupling computations, one antenna is always excited using a current or voltage source, whereas the second antenna is left as an open circuit. The field distribution for the transmitting antenna is obtained in the absence of the second antenna. Through a coupling matrix, which basically represents the governing transfer function, the induced field in the aperture of the second antenna is computed. This field acts as an excitation to the second antenna problem which can be solved to obtain the field distribution everywhere including the cavity. Using this field, a first-order approximation to the mutual impedance may be computed. The same coupling matrix can be used to compute the induced by the second antenna field in the aperture of the first antenna. The iterative process repeats until convergence is achieved. Results based on this algorithm are presented in this report for the coupling of two identical CBS antennas placed at some distance apart. The predictions are compared with data obtained using the hybrid FEM/MoM direct approach. Results of mutual coupling as a function of distance are also included in the report.

Higher-order techniques in the context of the FDTD method have been one of our research topics during the last year. In the last couple of reports, we have introduced the concept of higher-order FDTD schemes. Specifically, a second-order accurate scheme in time and fourth-order accurate in space [FDTD(2,4)] was introduced for the solution of one-dimensional wave propagation problems. The results obtained using FDTD(2,4) were compared with results from a standard FDTD(2,2) scheme. It was shown in a previous report that the higher-order scheme exhibits significantly lower dispersion error for the same discretization. As a result of this observation, the higher-order scheme can be used to more accurately solve for electrically large problems, which are of special interest to the AHE project. Although there may seem at first that the implementation of FDTD(2,4) into a generic three-dimensional code is straightforward, there are few challenging problems that still need to be overcome. For example, for a fourth-order accurate scheme in space, the accurate enforcement of Dirichlet boundary conditions on PEC walls and around discontinuities is not easy.

The FDTD(2,4) has recently been implemented into a three-dimensional code to more accurately solve radiation problems at higher frequencies. For the truncation

of the computational domain, the anisotropic PML was used. This new higher-order code is very similar to the NEWS FDTD(2,2) code with the exception that scattering has not yet been implemented. This is the first version of FDTD(2,4) which is still under validation. As part of this validation process, the radiation patterns of a monopole mounted on the NASA helicopter are computed at 9.18 GHz. Numerical results are compared with the FDTD(2,2) (NEWS code) method and measurements.

For electrically large radiation problems, it is almost impossible though to obtain an accurate solution within a reasonable amount of time. One solution to electrically large problems is the implementation of a robust hybrid method. In this report, we have already introduced a hybrid FEM/MoM approach which computes mutual coupling through an iterative mechanism. The same ideas in now under investigation for the hybridization of FEM with PO to solve antenna radiation problems for helicopter communications. In other words, the fields of the transmitting antenna will be solved at the first iteration using the FEM. The PO surface currents on the surface of the fuselage will be computed based on the radiated fields by the antenna. These surface currents produce scattered fields that are affecting the first-iteration field intensity in the vicinity of the antenna. This perturbation field will be considered at the second iteration to correct the governing fields in the antenna domain. The iteration continues on until convergence is achieved. To implement this idea, it was decided to begin with a two-dimensional finite element code which uses either ABC's or BI methods for the truncation of the computational domain. This code has been written and validated against other numerical solutions in this report. A first-order hybridization with the PO is also shown here. This means that, at this stage, there is only one-way interaction between the antenna and the object; i.e., the fields scattered by the object are not allowed yet to change the field distribution in the vicinity of the antenna. This feature will be implemented in the next AHE report.

An alternative to hybrid methods approach to solving electrically large computational problems is the use of spectral methods. Spectral methods are very powerful due to their impressive accuracy, exponential convergence, and negligible dispersion and dissipation. These are all desirable features for the solution of radiation problems involving helicopters. In the previous report, we presented and discussed the basic formulation of spectral methods. Some of the feature of spectral methods were

demonstrated through numerical experiments and comparison with finite difference methods. In this report, the spectral methods are applied for the first time to one-dimensional propagation problems. The accuracy and future potential of these methods in electromagnetics is demonstrated through numerical experiments.

Chapter 1

Thin Conducting Layer Subcell Modeling

I. Introduction

Problems concerning numerical accuracy may arise when someone tries to simulate, using FDTD, structures that contain elements such as sheets, slots and wires which are too fine to be resolved by the smallest affordable cell size. The problem becomes more serious when the material is of high conductivity which must be distinguished from a perfect conductor. In this section, we present a subcell modeling for thin conducting sheets [1]. This model assumes a one dimensional variation of the fields within the slab in a direction normal to the sheet. This assumption is a good approximation under the following conditions:

- The thickness of the sheet is much smaller than its radius of curvature and its transversal dimensions
- The conductivity of the material is sufficiently high so that the waves propagate in a direction normal to the sheet.

II. Analysis

We start the analysis by examining the role of the second condition mentioned in section I.. For this purpose, the problem in Fig. 1.1 is examined. In this figure, a uniform plane wave is incident from free space on a conductive material half space.

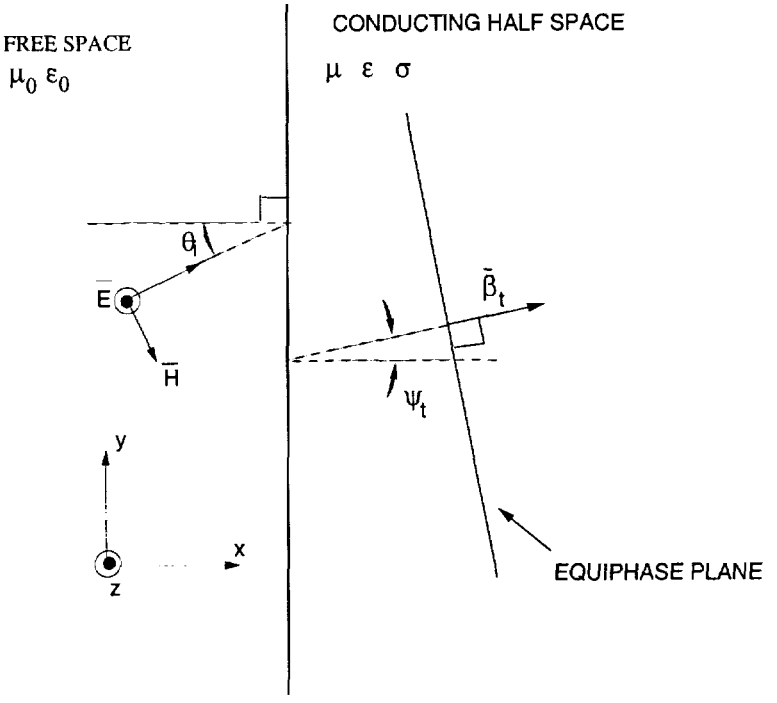

Figure 1.1: Wave incident from free space on a conductive half space

The incident wave electric field $\bar{E}_i$ is described by:

$$\bar{E}_i = \bar{a}_z E_0 e^{-j\beta_0(x\cos\theta_i + y\sin\theta_i)} = \bar{a}_z E_0 e^{-j\bar{\beta}_0\cdot\bar{r}} \tag{1.1}$$

where

$$\beta_0 \equiv \omega\sqrt{\mu_0\epsilon_0} \tag{1.2}$$

The transmitted wave is given by:

$$\bar{E}_t = \bar{a}_z E_{t0} e^{-\gamma_x x - \gamma_y y} = \bar{a}_z E_{t0} e^{-\bar{\gamma}\cdot\bar{r}} \tag{1.3}$$

The coefficients γ_x, γ_y satisfy the constraint equation:

$$\gamma_x^2 + \gamma_y^2 = \gamma^2 \equiv -\omega^2\mu\epsilon\left(1 - j\frac{\sigma}{\omega\epsilon}\right) \tag{1.4}$$

Since the continuity of the tangential fields at the interface $x = 0$ must hold for any value of y, the coefficients of y at the exponentials of the incident (1.1), reflected and transmitted (1.3) fields must be the same; hence:

$$\gamma_y \equiv \alpha_y + j\beta_y = j\beta_0\sin\theta_i \tag{1.5}$$

From (1.4) and (1.5) we obtain γ_x :

$$\gamma_x = \sqrt{\gamma^2 - \gamma_y^2} = \sqrt{-\omega^2\mu\epsilon\left(1 - j\frac{\sigma}{\omega\epsilon}\right) + \beta_0^2 \sin^2\theta_i} \tag{1.6}$$

For a highly conducting material ($\sigma \gg \omega\epsilon$), (1.6) and (1.2) give:

$$\begin{aligned} \gamma_x &= \sqrt{j\omega\mu\sigma + \beta_0^2 \sin^2\theta_i} \\ &= \frac{1+j}{\sqrt{2}}\sqrt{\omega\mu\sigma}\sqrt{1 - j\left(\frac{\omega\epsilon_0}{\sigma}\right)\left(\frac{\mu_0}{\mu}\sin^2\theta_i\right)} \end{aligned} \tag{1.7}$$

If $\sigma \gg \omega\epsilon_0$ and μ is of the same order as μ_0 then by writing $\gamma_x \equiv \alpha_x + j\beta_x$, we obtain:

$$\alpha_x = \beta_x = \sqrt{\frac{\omega\mu\sigma}{2}} \tag{1.8}$$

From Fig. 1.1, it is seen that $\tan\psi_t = \beta_y/\beta_x$. Hence, under the same assumptions as above and using (1.8), (1.5) and (1.2), we obtain:

$$\begin{aligned} \tan\psi_t &= \frac{\beta_y}{\beta_x} \simeq \sqrt{2}\frac{\beta_0 \sin\theta_i}{\sqrt{\omega\mu\sigma}} \\ &= \sqrt{2}\sqrt{\left(\frac{\omega\epsilon_0}{\sigma}\right)\left(\frac{\mu_0}{\mu}\right)}\sin\theta_i \simeq 0 \end{aligned} \tag{1.9}$$

From (1.5) and (1.9), it is seen that not only the constant amplitude planes but also the constant phase planes in Fig. 1.1 are approximately parallel to the interface. This means that the fields within the conducting material vary only in the x-direction, which is normal to the interface. The same is true for the case of the conducting layer shown in Fig. 1.2. Hence, the electric field within the layer satisfies the one dimensional wave equation:

$$\begin{aligned} \nabla^2\bar{E} - \gamma^2\bar{E} &= 0 \Leftrightarrow \\ \bar{E} &= \bar{A}^- e^{\gamma x} + \bar{A}^+ e^{-\gamma x} \end{aligned} \tag{1.10}$$

where $\bar{A}^-$, $\bar{A}^+$ are arbitrary constants and γ is given by:

$$\gamma = \sqrt{-\omega^2\mu\epsilon\left(1 - j\frac{\sigma}{\omega\epsilon}\right)} \tag{1.11}$$

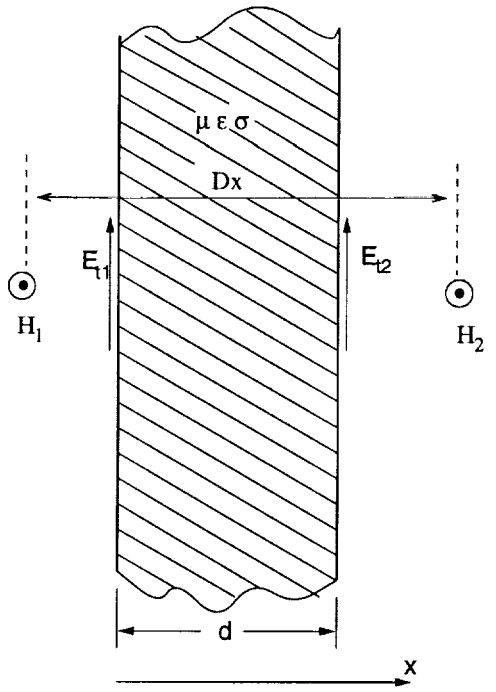

Figure 1.2: Thin conductive layer

The square root in (1.11) is the one with the positive imaginary part so that the first term in (1.10) represents a wave traveling in the negative x-direction and the second a wave traveling in the positive. Using the Maxwell-Faraday equation combined with (1.10), we obtain the magnetic field:

$$\begin{aligned} \bar{H} &= -\frac{j}{\omega\mu} \nabla \times \bar{E} \\ &= \frac{j\gamma}{\omega\mu} \bar{a}_x \times \left(\bar{A}^- e^{\gamma x} - \bar{A}^+ e^{-\gamma x} \right) = \bar{H}_t \end{aligned} \tag{1.12}$$

This field has only components along y and z axes, and is denoted as $\bar{H}_t$. The purpose of the present derivation is to express the electric fields at the two faces of the slab shown in Fig. 1.2 in terms of the magnetic fields, thus producing a "two-port network" representation of the slab in Fourier transform domain. In order to achieve this, the electric and magnetic fields in (1.10) and (1.12) are evaluated at the two faces of the slab (x=0 and x=d):

$$\bar{E}(0) = \bar{A}^- + \bar{A}^+ \tag{1.13}$$

$$\bar{E}(d) = \bar{A}^{-}e^{\gamma d} + \bar{A}^{+}e^{-\gamma d} \tag{1.14}$$

$$\bar{H}(0) \equiv \bar{H}_{t1} = \frac{j\gamma}{\omega\mu}\bar{a}_x \times \left(\bar{A}^{-} - \bar{A}^{+}\right) \tag{1.15}$$

$$\bar{H}(d) \equiv \bar{H}_{t2} = \frac{j\gamma}{\omega\mu}\bar{a}_x \times \left(\bar{A}^{-}e^{\gamma d} - \bar{A}^{+}e^{-\gamma d}\right) \tag{1.16}$$

where the subscript t indicates that the magnetic fields have only components tangential to the faces of the slab. Taking the cross product of $\bar{a}_x$ with both sides of (1.15) gives:

$$\begin{aligned}
\bar{a}_x \times \bar{H}_{t1} &= \frac{j\gamma}{\omega\mu}\bar{a}_x \times \left(\bar{a}_x \times \left(\bar{A}^{-} - \bar{A}^{+}\right)\right) \\
&= \frac{j\gamma}{\omega\mu}\left[\left(\bar{a}_x \cdot \left(\bar{A}^{-} - \bar{A}^{+}\right)\right) - \left(\bar{A}^{-} - \bar{A}^{+}\right)\right] \\
&= \frac{j\gamma}{\omega\mu}\left(\bar{A}_t^{+} - \bar{A}_t^{-}\right)
\end{aligned} \tag{1.17}$$

where $\bar{A}_t^{+}$, $\bar{A}_t^{-}$ are the tangential components of $\bar{A}^{+}$, $\bar{A}^{-}$ respectively. The same procedure but for (1.16) gives:

$$\bar{a}_x \times \bar{H}_{t2} = \frac{j\gamma}{\omega\mu}\left(\bar{A}_t^{+}e^{-\gamma d} - \bar{A}_t^{-}e^{\gamma d}\right) \tag{1.18}$$

Solving the system of (1.17) and (1.18), we find:

$$\bar{A}_t^{+} = \frac{\omega\mu}{j\gamma}\,\frac{-e^{\gamma d}\left(\bar{a}_x \times \bar{H}_{t1}\right) + \bar{a}_x \times \bar{H}_{t2}}{e^{-\gamma d} - e^{\gamma d}} \tag{1.19}$$

$$\bar{A}_t^{-} = \frac{\omega\mu}{j\gamma}\,\frac{-e^{-\gamma d}\left(\bar{a}_x \times \bar{H}_{t1}\right) + \bar{a}_x \times \bar{H}_{t2}}{e^{-\gamma d} - e^{\gamma d}} \tag{1.20}$$

Substituting (1.19) and (1.20) into (1.13) and (1.14), the desired two-port network relationship is obtained:

$$\begin{bmatrix} \bar{E}_{t1} \\ \bar{E}_{t2} \end{bmatrix} = \begin{bmatrix} Z_{11} & Z_{12} \\ Z_{21} & Z_{22} \end{bmatrix} \begin{bmatrix} \bar{n} \times \bar{H}_{t1} \\ \bar{n} \times \bar{H}_{t2} \end{bmatrix} \tag{1.21}$$

where,

$$Z_{11} = Z_{22} = -\frac{j\omega\mu}{k}\frac{1}{\tan(kd)} \tag{1.22}$$

$$Z_{12} = Z_{21} = -\frac{j\omega\mu}{k}\frac{1}{\sin(kd)} \tag{1.23}$$

and k is such that $\gamma = jk$ so that the expressions in (1.22) and (1.23) are of the same form as in [1]. The unit vector $\bar{n}$ is normal to the slab and directed outwards in both faces:

$$\bar{n} = \begin{cases} -\bar{a}_x & \text{for } x = 0 \\ \bar{a}_x & \text{for } x = d \end{cases} \tag{1.24}$$

For good conductors ($\sigma \gg \omega\epsilon$), k in (1.4) becomes:

$$k = -j\gamma = -j\sqrt{-\omega^2\mu\epsilon\left(1 - j\frac{\sigma}{\omega\epsilon}\right)} \simeq -j\sqrt{j\omega\mu\sigma} = (1-j)\sqrt{\frac{\omega\mu\sigma}{2}} \tag{1.25}$$

$$k^2 = -j\omega\mu\sigma \tag{1.26}$$

The implementation of (1.21) in time domain starts by expanding the trigonometric functions of (1.22) and (1.23) in power series and keeping a finite number of terms:

$$Z_{11} = -\frac{j\omega\mu}{k}\frac{\cos(kd)}{\sin(kd)} = -\frac{j\omega\mu}{k}\frac{\sum_{n=0}^{\infty}\frac{(kd)^{2n}(-1)^n}{(2n)!}}{\sum_{n=0}^{\infty}\frac{(kd)^{2n+1}(-1)^n}{(2n+1)!}}$$

$$= -\frac{j\omega\mu}{k^2 d}\frac{\sum_{n=0}^{\infty}\frac{(kd)^{2n}(-1)^n}{(2n)!}}{\sum_{n=0}^{\infty}\frac{(kd)^{2n}(-1)^n}{(2n+1)!}}$$

$$= \frac{1}{\sigma d}\frac{\sum_{n=0}^{\infty}\frac{(kd)^{2n}(-1)^n}{(2n)!}}{\sum_{n=0}^{\infty}\frac{(kd)^{2n}(-1)^n}{(2n+1)!}}$$

$$= \frac{1}{\sigma d}\frac{\sum_{n=0}^{\infty}\frac{\left(-j\omega\mu\sigma d^2\right)^n(-1)^n}{(2n)!}}{\sum_{n=0}^{\infty}\frac{(-j\omega\mu\sigma d^2)^n(-1)^n}{(2n+1)!}}$$

$$= \frac{1}{\sigma d}\frac{\sum_{n=0}^{\infty}\frac{\left(j\omega\mu\sigma d^2\right)^n}{(2n)!}}{\sum_{n=0}^{\infty}\frac{(j\omega\mu\sigma d^2)^n}{(2n+1)!}}$$

$$= \frac{1}{\sigma d} \frac{\sum_{n=0}^{\infty} \frac{(j\omega')^n}{(2n)!}}{\sum_{n=0}^{\infty} \frac{(j\omega')^n}{(2n+1)!}}$$

$$\simeq \frac{1}{\sigma d} \frac{\sum_{n=0}^{M} \frac{(j\omega')^n}{(2n)!}}{\sum_{n=0}^{N} \frac{(j\omega')^n}{(2n+1)!}} \tag{1.27}$$

where,

$$\omega' = \omega\mu\sigma d^2 \tag{1.28}$$

Similarly, Z_{12} is written as:

$$Z_{12} \simeq \frac{1}{\sigma d} \frac{1}{\sum_{n=0}^{N} \frac{(j\omega')^n}{(2n+1)!}} \tag{1.29}$$

Now (1.27) and (1.29) are expanded in a partial fraction sum:

$$Z_{11} = \frac{1}{\sigma d} \left\{ \sum_{n=1}^{m} \frac{A_{11,n}}{j\omega' + B_n} + \sum_{k=1}^{l} \frac{C_{11,k}\, j\omega' + D_{11,k}}{(j\omega')^2 + E_k\, j\omega' + F_k} \right\} \tag{1.30}$$

$$Z_{12} = \frac{1}{\sigma d} \left\{ \sum_{n=1}^{m} \frac{A_{12,n}}{j\omega' + B_n} + \sum_{k=1}^{l} \frac{C_{12,k}\, j\omega' + D_{12,k}}{(j\omega')^2 + E_k\, j\omega' + F_k} \right\} \tag{1.31}$$

where the first sums correspond to the real roots in the denominator of (1.27) and (1.29), and the second sums to the pairs of complex conjugate roots. The above expansion should be modified by including a polynomial if $M \geq N$. Substituting (1.30) and (1.31) into (1.21), we obtain:

$$\bar{E}_{t1} = \frac{1}{\sigma d} \left\{ \sum_{n=1}^{m} \bar{X}_{11,n} + \sum_{k=1}^{l} \bar{X}_{11,k} + \sum_{n=1}^{m} \bar{X}_{12,n} + \sum_{k=1}^{l} \bar{X}_{12,k} \right\} \tag{1.32}$$

$$\bar{E}_{t2} = \frac{1}{\sigma d} \left\{ \sum_{n=1}^{m} \bar{X}_{21,n} + \sum_{k=1}^{l} \bar{X}_{21,k} + \sum_{n=1}^{m} \bar{X}_{22,n} + \sum_{k=1}^{l} \bar{X}_{22,k} \right\} \tag{1.33}$$

where the auxiliary variables $\bar{X}_{ij,n}$, $\bar{X}_{ij,k}$ are defined as:

$$\bar{X}_{11,n} \equiv \frac{A_{11,n}}{j\omega' + B_n} \bar{n} \times \bar{H}_{t1} \tag{1.34}$$

$$\bar{X}_{11,k} \equiv \frac{C_{11,k}\, j\omega' + D_{11,k}}{(j\omega')^2 + E_k\, j\omega' + F_k} \bar{n} \times \bar{H}_{t1} \tag{1.35}$$

$$\bar{X}_{12,n} \equiv \frac{A_{12,n}}{j\omega' + B_n} \bar{n} \times \bar{H}_{t2} \tag{1.36}$$

$$\bar{X}_{12,k} \equiv \frac{C_{12,k}\, j\omega' + D_{12,k}}{(j\omega')^2 + E_k\, j\omega' + F_k} \bar{n} \times \bar{H}_{t2} \tag{1.37}$$

and so on for the rest of them. These equations are transformed in time domain giving auxiliary differential equations. From (1.34) and (1.35), for example, we obtain using also (1.28):

$$\mu\sigma d^2 \frac{d}{dt} \bar{X}_{11,n}(t) + B_n \bar{X}_{11,n}(t) = A_{11,n}\, \bar{n} \times \bar{H}_{t1}(t) \tag{1.38}$$

$$\left(\mu\sigma d^2\right)^2 \frac{d^2}{dt^2} \bar{X}_{11,k}(t) + \mu\sigma d^2 E_k \frac{d}{dt} \bar{X}_{11,k}(t) + F_k \bar{X}_{11,k}(t) =$$

$$\mu\sigma d^2 C_k \frac{d}{dt} \left(\bar{n} \times \bar{H}_{t1}(t)\right) + D_k\, \bar{n} \times \bar{H}_{t1}(t) \tag{1.39}$$

These differential equations are then discretized in time using a finite difference scheme and update equations are derived and combined with the usual Yees' FDTD algorithm as follows: First, the magnetic fields $\bar{H}_{t1}$, $\bar{H}_{t1}$ are advanced using the last values of $\bar{E}_{t1}$, $\bar{E}_{t2}$. Since the tangential magnetic fields at the faces of the slab are not included in the normal FDTD scheme, they can be approximated by the nearby available components H_1, H_2 as shown in Fig. 1.2. If the thickness of the layer d is much smaller than the cell size Δx then $\bar{E}_{t1}$, and $\bar{E}_{t2}$ can be both assumed to reside midway between $\bar{H}_{t1}$ and $\bar{H}_{t1}$, therefore the ordinary FDTD update equations can be used. Then, the auxiliary variables $\bar{X}_{ij,n}$, $\bar{X}_{ij,k}$ are advanced in time and finally the new electric fields $\bar{E}_{t1}$, $\bar{E}_{t2}$ are obtained using the time domain equivalent of (1.32) and (1.33).

Currently, the implementation of the above procedure in one dimension is in progress.

Chapter 2

FDTD Predictions of Penetration Through Apertures in Conducting Enclosures

The penetration of electromagnetic fields into conducting enclosures via apertures is an EMI issue that is relevant to all of aviation. The stories are numerous, of disrupted communications, disabled navigation equipment, and worse; due to the effects of EM sources external to the aircraft.

Although there are many possible mechanisms for the penetration of fields into an aircraft (including direct penetration through composites, penetration through cracks and joints, conduction along cabling, etc.), it is usually the windows which admit the greatest. Consequently, it is of greatest importance to understand and be able to predict the field penetration through apertures.

In this report, three cases of penetration are considered. The three cases consist of a modestly sized enclosure with three aperture configurations: one large aperture, two large apertures, and one small aperture.

Contrary to initial intuitive estimations, these are not entirely trivial problems for the Finite-Difference, Time-Domain (FDTD) method. Particularly when the aperture is small relative to the size of the enclosure, the decay time of a pulsed excitation is enormous. However, there may be some advantages to introducing an artificial loss mechanism into the problem space to accelerate the decay of the late-time fields.

Thank you to Dr. M. D. Deshpande of FDC/NYMA Langley Research Center, and Fred Beck and C. Cockrell of NASA Langley Research Center for providing the MoM

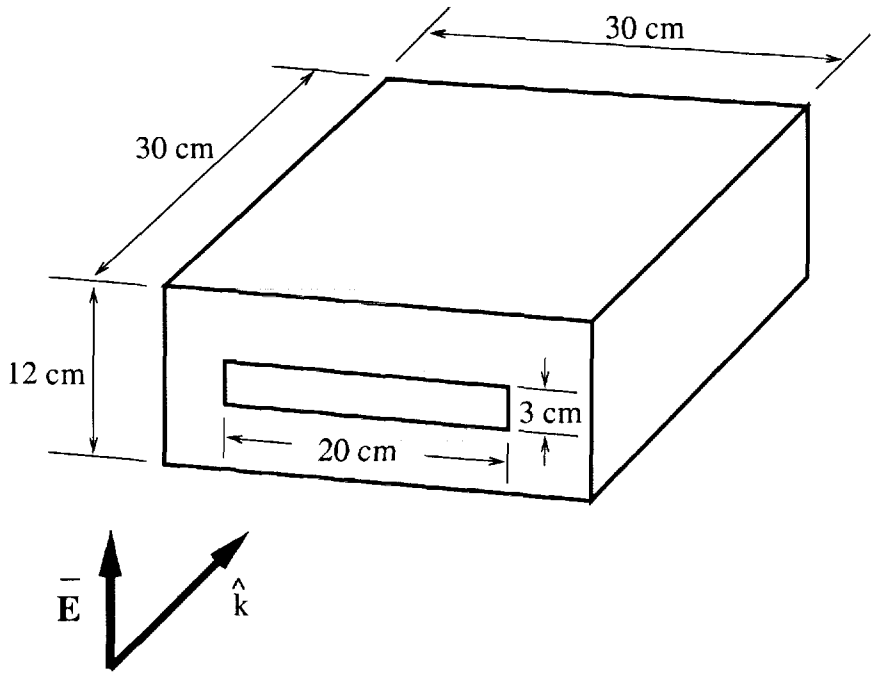

Figure 2.1: A 30 cm X 30 cm X 12 cm conducting box with a 20 cm X 3 cm aperture. A vertically polarized plane wave is normally incident on the aperture.

predictions and measurements used for comparisons with the FDTD predictions.

I. Case #1

The enclosure is a rectangular box having the dimensions of 30 cm wide by 30 cm deep by 12 cm high. The first aperture case (Case #1) consists of a 20 cm wide by 3 cm high aperture in the side of the box. The drawing in Figure 2.1 illustrates this small box with an aperture.

As shown in the figure, the fields (a Gaussian pulse) are normally incident on the aperture. The Rayleigh number (β) for the pulse was chosen to yield a spectrum of up to 1 GHz.

This geometry was discretized at a cell size of 2.5mm. This cell size is very small ($\lambda/120$ at 1 GHz), but is necessary to resolve the aperture of Case #3. This discretization results in a solution space that measures 130 x 130 x 58 cells, for a total

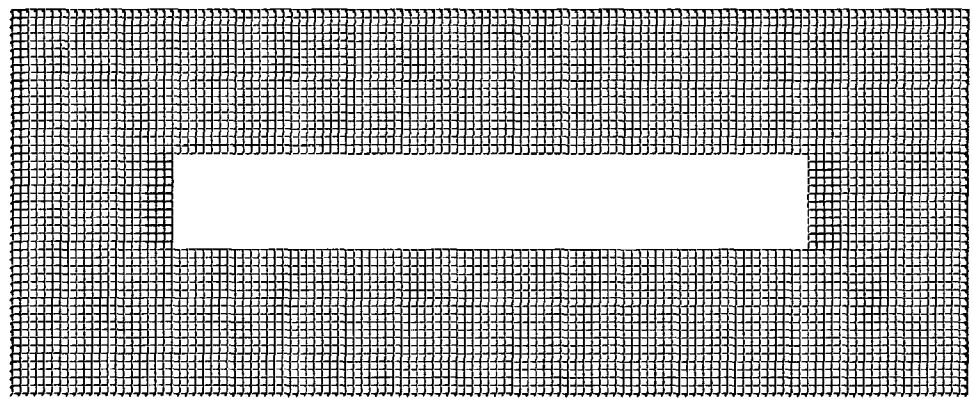

Figure 2.2: The 30 X 30 X 12 cm box with the 20 X 3 cm aperture (Case #1) was discretized at 2.5 mm per cell ($\lambda/120$ at 1 GHz).

of 980,200 cells. A view of the mesh from the side of the box containing the aperture is pictured in Figure 2.2. Five pad cells separate the sides of the box from the six layers of PML.

The pivotal issue in using a pulse excitation with the FDTD method is that the fields (or currents), particularly at the locations of interests, decay to zero. When the time-domain response has decayed to zero, it can be Fourier transformed into the frequency domain without error. In some cases, it may not be practical or possible to execute sufficient simulation time to achieve complete decay of the pulse response. In those cases, a reasonably good answer can be obtained by transforming the pulse response after it has decayed to a sufficiently small amount. However, the criterion for what is "sufficiently small" has not been formalized.

After some "false starts," Case #1 was executed for 131,000 time steps. This corresponds to a simulation time of 0.6 microseconds. In this $0.6\mu sec$, the pulse could travel back and forth (across the long dimension) through the enclosure almost 600 times. This simulation ran for approximately 46 (wall clock) hours on our SGI Octane.

In Figure 2.3, the component of the time-domain electric field, at the center of the enclosure, that is copolarized with the excitation field is plotted with respect to the number of time steps. As shown in the inset, the field has decayed to an amplitude of 0.0002 V/m. As will be seen in Figure 2.4, this is sufficiently close to zero to result in an accurate prediction for this case.

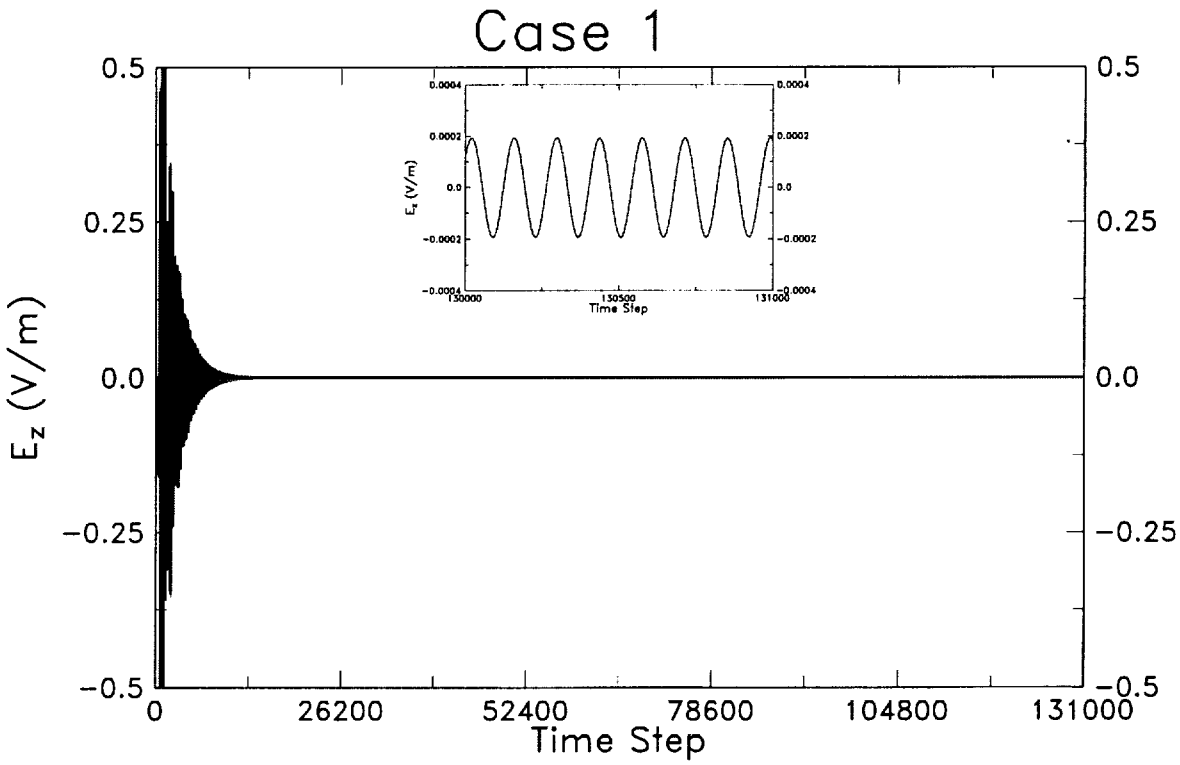

Figure 2.3: The time-domain electric field at the center of the enclosure for Case #1. The fields have decayed to .0002 V/m at the end of 131,000 time steps.

The results are presented here as elecric field shielding. The electric field shielding is a relation between the fields at the center of the box relative to the fields outside of the box. To realize the electric field shielding using the FDTD, the following procedure was performed. First, an empty FDTD solution space was created. This empty solution space does not need to be large. A space of 26 x 26 x 26 cells was chosen. The cell size of the empty solution space must match that of the problem solution space. Then the same pulse used in the problem simulation was launched in the empty solution space. The frequency response of the pulse at the center of the empty solution space was stored. Note that the number of time steps can be greatly reduced compared to that of the problem simulation. In this case, 32,000 time steps were used. This was more than necessary. Finally, the "electric field shielding" was computed according to

$$\text{electric field shielding} = 20\log\left(\frac{\text{empty space frequency response}}{\text{problem space frequency response}}\right) \qquad (2.1)$$

where "empty space frequency response" and "problem space frequency response" are the linear magnitude values of the z components of the frequency-domain electric fields computed at the centers of the empty and problem solution spaces, respectively. Note that with this definition, the fields at the center of the enclosure are highest when the electric field shielding is lowest (near 650 MHz for Case #1).

The FDTD-predicted electric field shielding is plotted in Figure 2.4 with measured values and Method of Moments (MoM) predicted values. The MoM prediction model consists of the cavity mounted behind an infinite ground plane which includes the aperture. Thus the MoM prediction does not include any diffraction effects from the exterior edges of the enclosure. The correlation of the FDTD prediction is excellent compared to the MoM prediction and the somewhat noisy measurement. This noise is attributed to resonances in the screen room in which the measurements were performed [2].

II. Case #2

Case #2 consists of the same box as in Case #1, but with two 20 x 3 cm apertures. One aperture is at the same location as the one for Case #1, the second aperture is located in the center of the side of the box opposite the illumination. A drawing of the conducting enclosure with the two apertures of Case #2 is shown in Figure 2.5.

All of the FDTD parameters (cell size, β, number of pad cells, etc.) for Case #2 are the same as those in Case #1. The predictions were again computed for 131,000 time steps, and the same procedure was used to normalize the resulting frequency-domain field at the center of the enclosure relative to the input pulse response.

The time-domain response of the pulse at the center of the cavity is shown in Figure 2.6. The field configuration and pulse response is different from that of Case #1 due to the different aperture configuration. The time-domain fields are somewhat lower for this reason. The peak response for Case #1 is 0.7262 V/m; for Case #2 it is 0.4421 V/m. However, the amplitude of the late-time fields for Case #1 is approximately 1.93×10^{-4}, or about 0.027% that of the peak. In Case #2, the amplitude of the late-time fields is about 4.8×10^{-5} V/m, or about 0.011% of the peak. It is a reasonable conclusion that the fields inside the cavity of Case #2 have decayed more rapidly than those in Case #1 due to the additional loss mechanism of the second aperture.

The only values available for comparison for this case are MoM predictions. One of the predictions is labeled "with internal coupling", the other is labeled "without internal coupling" (with respect to the apertures). It is assumed by the author that these two predictions were intended to explore the effects of the coupling between the two apertures, and are not the most accurate MoM predictions possible. This is in consideration of the fact that this structure is slightly less demanding on the FDTD than that of Case #1, for which the agreement with MoM was excellent. The FDTD-predicted electric field shielding in Figure 2.7 is greater than that of the MoM predictions. However, the general shape is very similar, and the null occurs at approximately the same frequency as in the MoM predictions.

III. Case #3

Again, the enclosure for Case #3 has the same dimensions as those in Case #1 and #2. This time, the single aperture is 0.5 cm in height and 10 cm wide. The vertically polarized pulse is again normally incident on the face of the box which contains the aperture, as shown in Figure 2.8. The geometry was again meshed at 2.5 mm per cell. The mesh of the aperture side of the box is shown in Figure 2.9.

After executing Case #3 for 131,000 time steps, the time-domain electric field amplitude at the center of the box has only decayed to a value of 0.03 V/m, as seen in the inset of Figure 2.10. This high-Q cavity essentially represents a condition that is the opposite of Case #2 relative to Case #1: the smaller aperture of Case #3 provides a smaller loss mechanism, and the fields decay very slowly.

Is the late-time electric field amplitude of 0.03 V/m close enough to zero for the accurate transformation of the time-domain fields into the frequency domain? The electric field shielding was computed as before, and the results are plotted with MoM prediction and with measured values in Figure 2.11. The agreement between the measurement and the MoM prediction indicates that they are accurate, and that the FDTD prediction is significantly in error. The only agreement between the FDTD prediction, and the MoM prediction and measurement is the location of the null at 700 MHz. Evidently, the time-domain fields have not decayed to a small enough value for the FFT to be accurate.

One possible solution is to execute the simulation for a greater number of time steps. With the current configuration of the code, a radix-2 FFT is used to transform the time-domain fields into the frequency domain. That means that the computer memory reserved for the time-history of the fields to be transformed must be increased by powers of two: the smallest increase is double the current number of time steps. In this particular case, the array size could be increased from 131,072 to 232,177. Unless there is reason to believe that the late-time fields will decay to an acceptably small value within some intermediate number of time steps, the logical number of time steps to run is then 232,000. That would take at least twice as long to run as does the present number of time steps: approximately four days. Judging from the rate of decay evident in Figure 2.10, a doubling of the number of time steps is unlikely to be sufficient. This option is not particularly appealing.

Another possibility is to introduce some additional loss mechanism into the solution space. To enlarge the existing aperture or add an additional aperture would surely change the field distribution inside, thus invalidate the prediction. The walls of the enclosure could be made lossy; however, a third possibility is to artificially assign some small loss to the free-space cells of the solution space. This third approach is attempted.

A. Case #3, artificial loss

The FDTD prediction for Case #3 was computed again for 131,000 time steps, but with the free-space cells artificially assigned a conductivity of 0.000001 S/m. This change was implemented in the input (control) file. The second parameter of the first media property line defines the conductivity of the free-space cells.

The time-domain electric field amplitude versus time step is shown in Figure 2.12. The late-time fields have decayed only slightly more than those for the lossless case. However, the electric field shielding has improved substantially as seen in Figure 2.13. The null at 700 MHz has increased to the MoM predicted value, and the erroneous peaks at approximately 410 MHz and 890 MHz have been reduced. However, the discrepancies between the FDTD prediction and the measurement and MoM prediction is still considerable, particularly below 300 MHz.

Some improvement in the FDTD-predicted electric field shielding was observed in the previous case in which the free-space cells were assigned a very small value of conductivity. The obvious next step would be to increase this conductivity to obtain a more pronounced effect on the late-time fields. This case was repeated with the artificial conductivity of the free-space cells set to 0.0032 S/m. Furthermore, the number of time steps have been reduced to 16,000.

In Figure 2.14, the time-domain fields at the center of the cavity are shown versus time steps, and the last 3,000 time steps are shown in the inset. The late-time fields have now been driven almost to zero within 16,00 time steps.

A dramatic improvement in the comparison between the FDTD prediction and the measurement and MoM prediction is evident in Figure 2.15. However, the FDTD-predicted null at 700 MHz is slightly higher than both the measured and MoM-predicted null.

B. Case #3, variable artificial loss

Finally, Case #3 is repeated after making a slight modification to the NEWS code to linearly increase the artificial conductivity assigned to the free-space cells. This variable conductivity is set to zero at time step zero, and increases to a value of 0.0064 S/m at 16,000 time steps. The value of 0.0064 S/m was chosen to yield the same *total* loss experienced by the pulse: the integration of the instantaneous conductivity with respect to the simulation time.

The time-domain field at the center of the cavity is plotted versus time steps in Figure 2.16. As seen in the inset, again the fields have been driven virtually to zero within 16,000 time steps. However, the difference in the rate of decay from that of the previous case is clearly evident.

The electric field shielding for this case is compared with measurement and MoM prediction in Figure 2.17. The agreement is excellent. Note that the FDTD-predicted null at 700 MHz is now between that of the measurement and the MoM prediction.

Why is the electric field shielding predicted by the FDTD slightly better when the artificial conductivity of the free-space cells is linearly increased than when it is set to a constant? It is speculated that there is an initial response to the pulse excitation that is critical to the accuracy of the final predicted spectrum. This initial pulse response is clearly seen in the time-domain field plots for Cases #1 and #2 (within the first few thousand time steps), but is not obvious in Case #3. In Figures 2.18 and 2.19 the time-domain field for the lossless Case #3 is compared with that using a constant artificial loss and a variable artificial loss, respectively. Notice that the time-domain response for the constant artificial loss case is different from that of the lossless case. However, the time-domain response of the linearly increasing artificial loss case is almost exactly the same as that of the lossless case for the first few thousand time steps. For the linearly increasing artificial loss case, the early-time loss is negligible and the initial pulse response is not significantly altered. The loss then increases to levels that are effective in causing a rapid decay of the late-time fields, enabling an accurate Fourier transformation into the frequency domain.

IV. Conclusions

The FDTD-based NEWS code was used to compute the electric field shielding of a conducting box having three different aperture configurations. The FDTD predictions were compared with measurements and MoM predictions, where available.

Due to the high Q of the cavities considered, the conventional second-order FDTD method required a very large number of time steps for a Gaussian pulse excitation to decay to a value that was sufficiently close to zero for accurate Fourier transformation of the time-domain fields into the frequency domain. With 131,000 time steps (in this case), however, the agreement of the FDTD predictions with measurements and MoM predictions were excellent.

The loss mechanism which allows the time-domain fields to decay consists of the fields exiting the cavity through the aperture and terminating into the Absorbing Boundary Condition (ABC). When the aperture area is small relative to the size of the cavity, the late-time fields decay more slowly than when the aperture area is large. For small apertures, the number of time steps necessary to allow the late-time fields to decay can be enormous. An extremely large number of time steps has significant drawbacks: long computation time, accumulation of dispersion, accumulation of numerical error, etc.

This study suggests that the introduction of an artificial loss mechanism into the solution space may be a viable alternative to extremely large numbers of time steps. In this report, the free-space cells were assigned a low value of conductivity. This additional loss mechanism did force the transient fields to decay more rapidly.

The speculations, based on the observations from this study, concerning the introduction of this artificial loss are as follows. When the free-space cells are assigned a very low value of conductivity, the loss experienced by the pulse is cumulative over a large number of time steps, and the greatest effect is on the late-time fields. When the free-space cells are assigned a higher value of conductivity, the initial pulse response of the cavity is altered, and the accuracy of the prediction is degraded. However, if the conductivity of the free-space cells is increased as a function of time steps from an initial value of zero, the initial pulse response of the cavity is virtually unaltered from its true free-space response. The artificial loss then increases to values that are effective in forcing the late-time fields to zero.

For Case #3 (a 30 x 30 x 12 cm box with a 10 x 0.5 cm aperture), 131,000 time steps were found to be insufficient for the late-time fields to decay to suitable levels. By slightly altering the NEWS code to linearly increase the conductivity of the free-space cells from zero to 0.0064 S/m, the transient fields were driven to zero in 16,000 time steps. This resulted in a predicted electric field shielding that was in excellent agreement with measurement and MoM prediction, and was a reduction in computation time of approximately 87% over that of the unaltered NEWS code (which did not yet yield an accurate FDTD prediction).

It should be noted that, strictly speaking, the use of time-varying material properties violates an assumption made in the formulation of the conventional FDTD update equations. The update equations are derived using the time derivative of the electric field intensity, not the electric flux density. Therefore, there is an implicit assumption made that the permittivity (ϵ) is constant with time.

The introduction of a linearly increasing artificial loss to the free-space cells of an FDTD problem consisting of a cavity with an aperture was found to greatly reduce the computation time of the calculations, reduce the computer memory requirements, enable the solution of an otherwise possibly intractable problem, and to yield results that are in excellent agreement with other methods. However, additional cases should be examined to verify that this technique is generally applicable to this class of problems. In addition, there may be advantages to other profiles (exponentially increasing, delayed, etc.) of the artificial loss that can be explored.

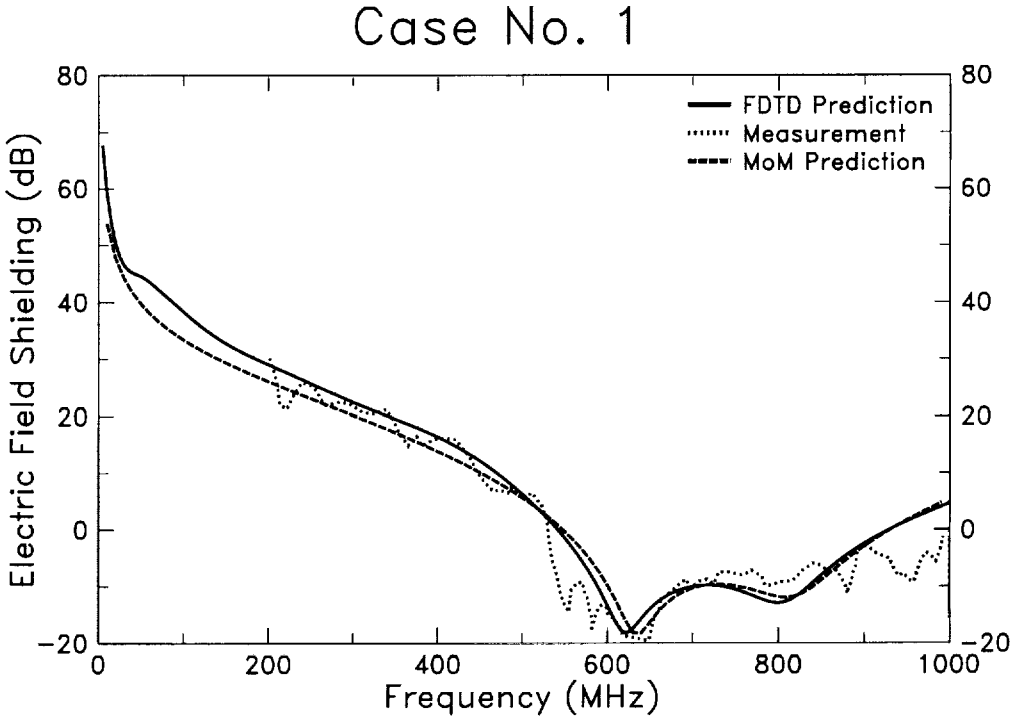

Figure 2.4: A comparison of the electric field shielding at the center of the enclosure for Case #1 between FDTD prediction, MoM prediction, and measurement.

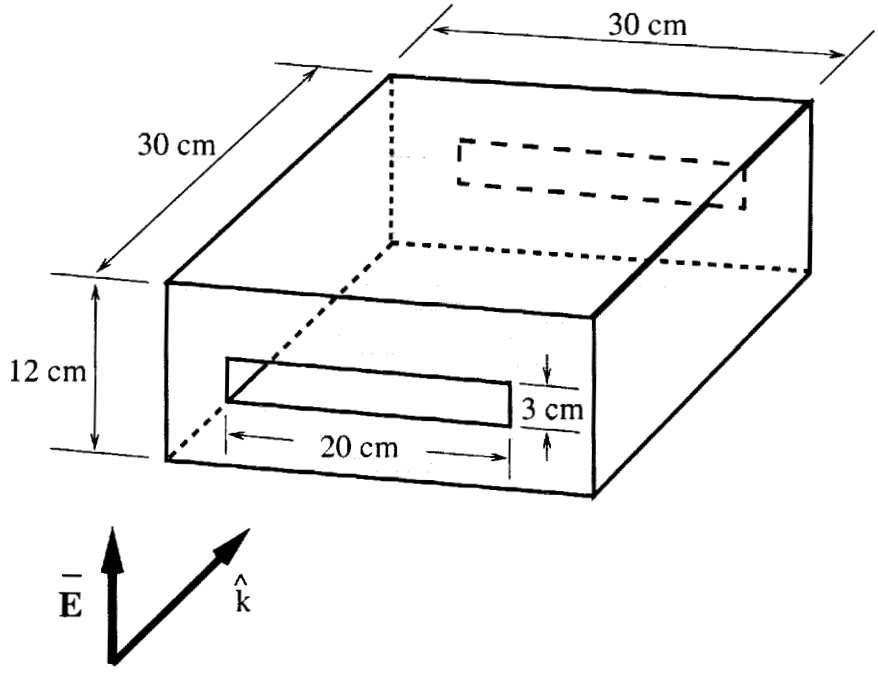

Figure 2.5: A 30 cm X 30 cm X 12 cm conducting box with two 20 cm X 3 cm apertures.

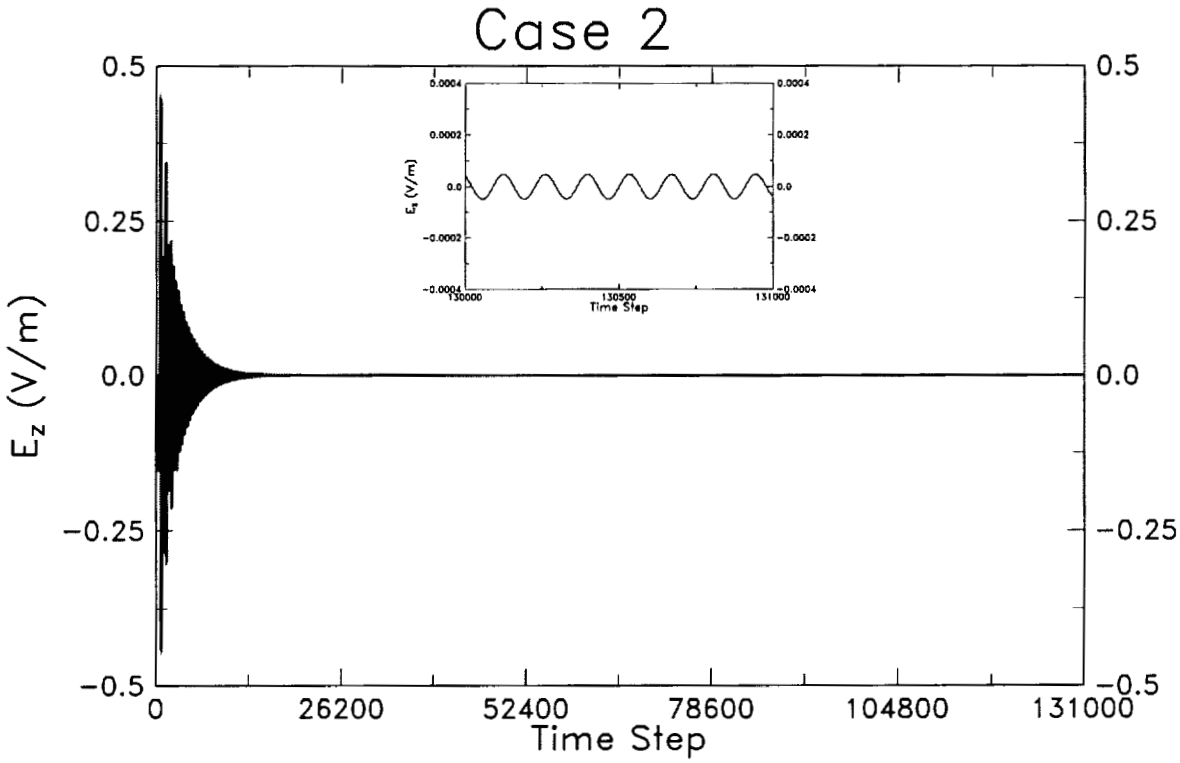

Figure 2.6: The time-domain electric field at the center of the enclosure for Case #2. The fields have decayed to approximately .00005 V/m at the end of 131,000 time steps.

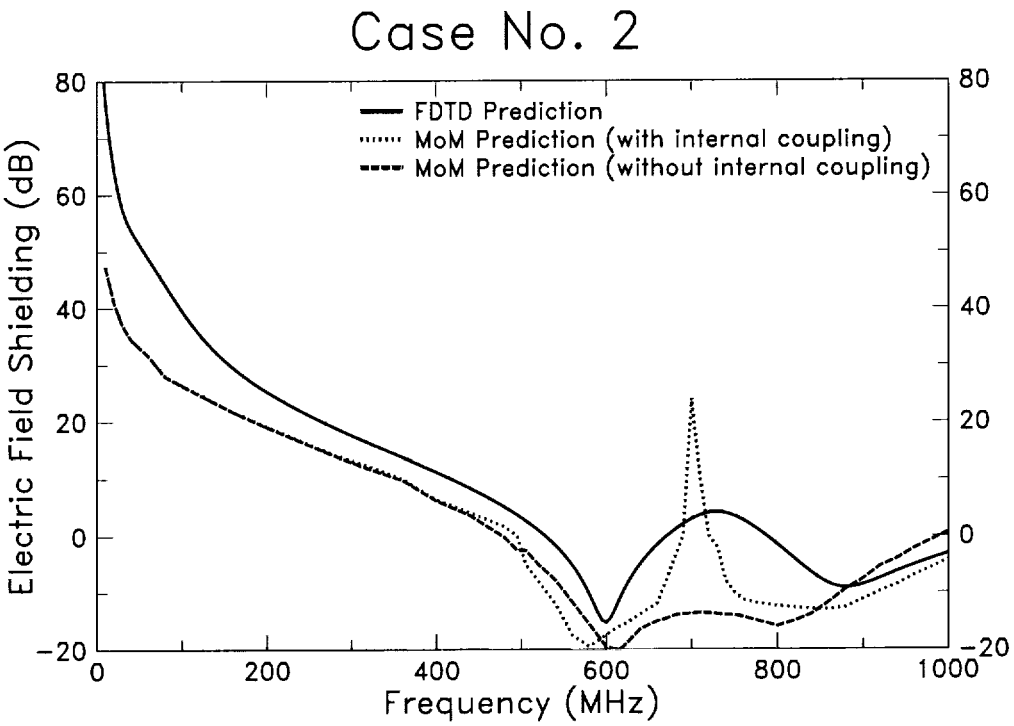

Figure 2.7: A comparison of the electric field shielding at the center of the enclosure for Case #2 between FDTD prediction, MoM prediction (with internal coupling between the apertures), and MoM prediction (without internal coupling between the apertures).

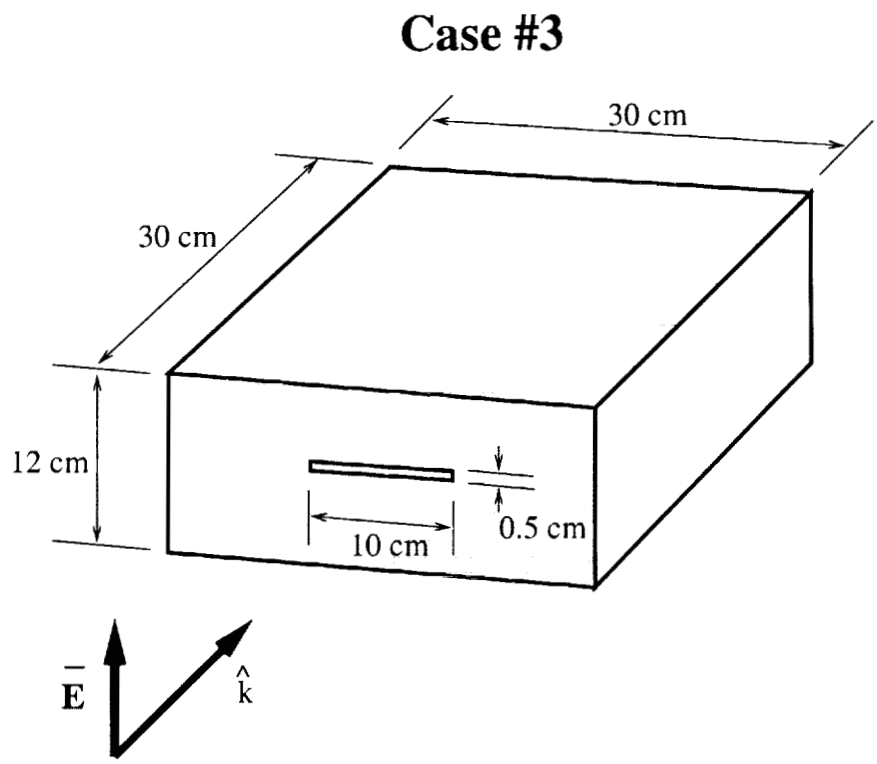

Figure 2.8: A 30 cm X 30 cm X 12 cm conducting box with one 10 cm X 0.5 cm aperture.

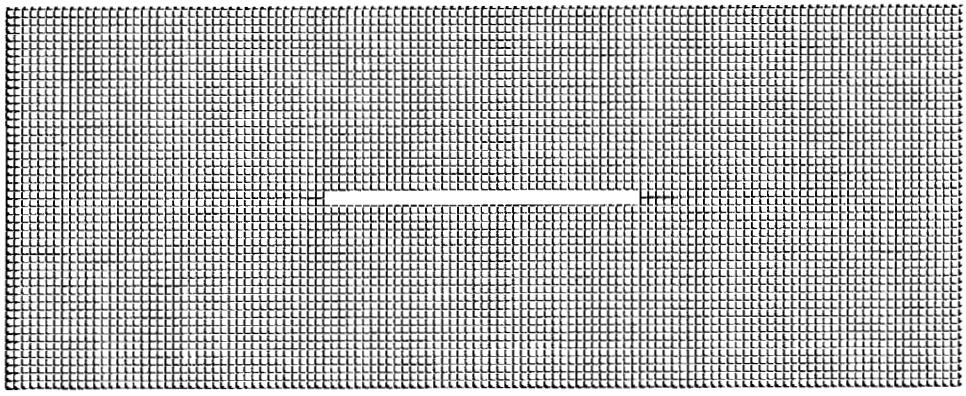

Figure 2.9: The 30 X 30 X 12 cm box with the 10 X 0.5 cm aperture (Case #3) was discretized at 2.5 mm per cell ($\lambda/120$ at 1 GHz).

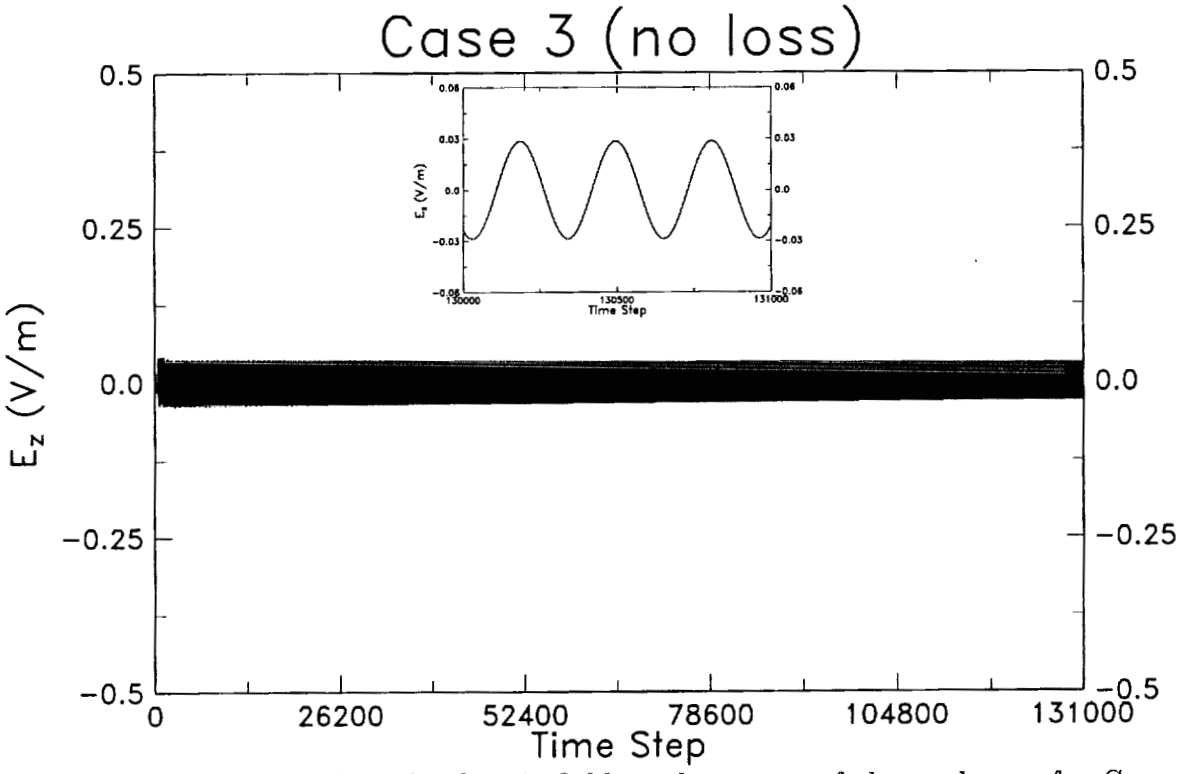

Figure 2.10: The time-domain electric field at the center of the enclosure for Case #3. The fields have only decayed to 0.03 V/m at the end of 131,000 time steps.

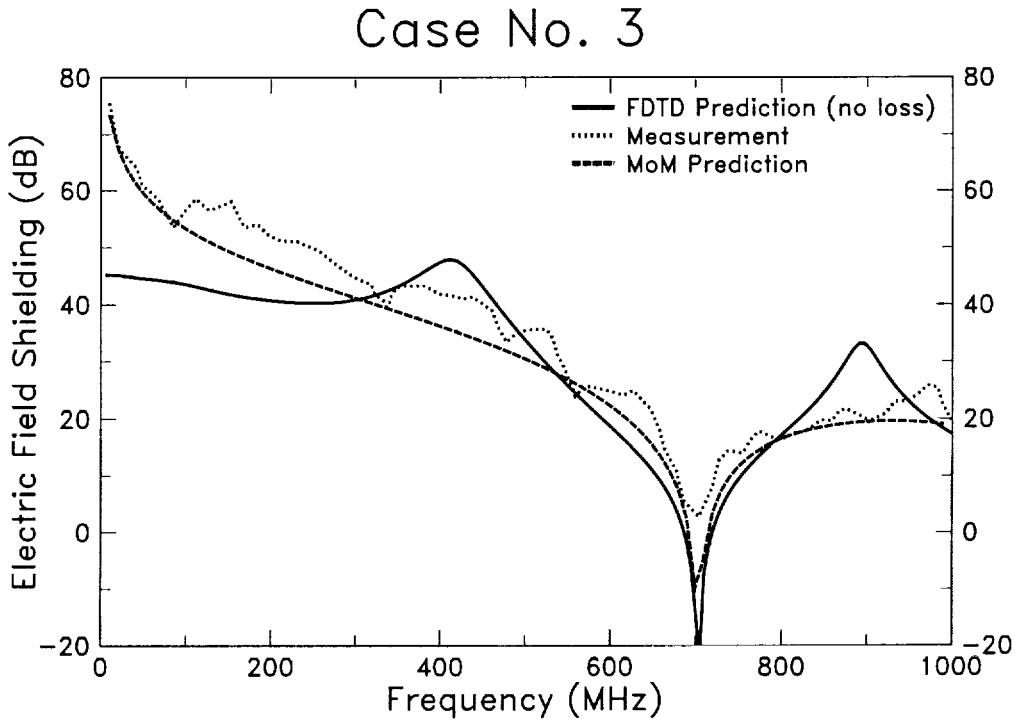

Figure 2.11: A comparison of the electric field shielding at the center of the enclosure for Case #3 between FDTD prediction (with no artificial loss mechanism), MoM prediction, and measurement.

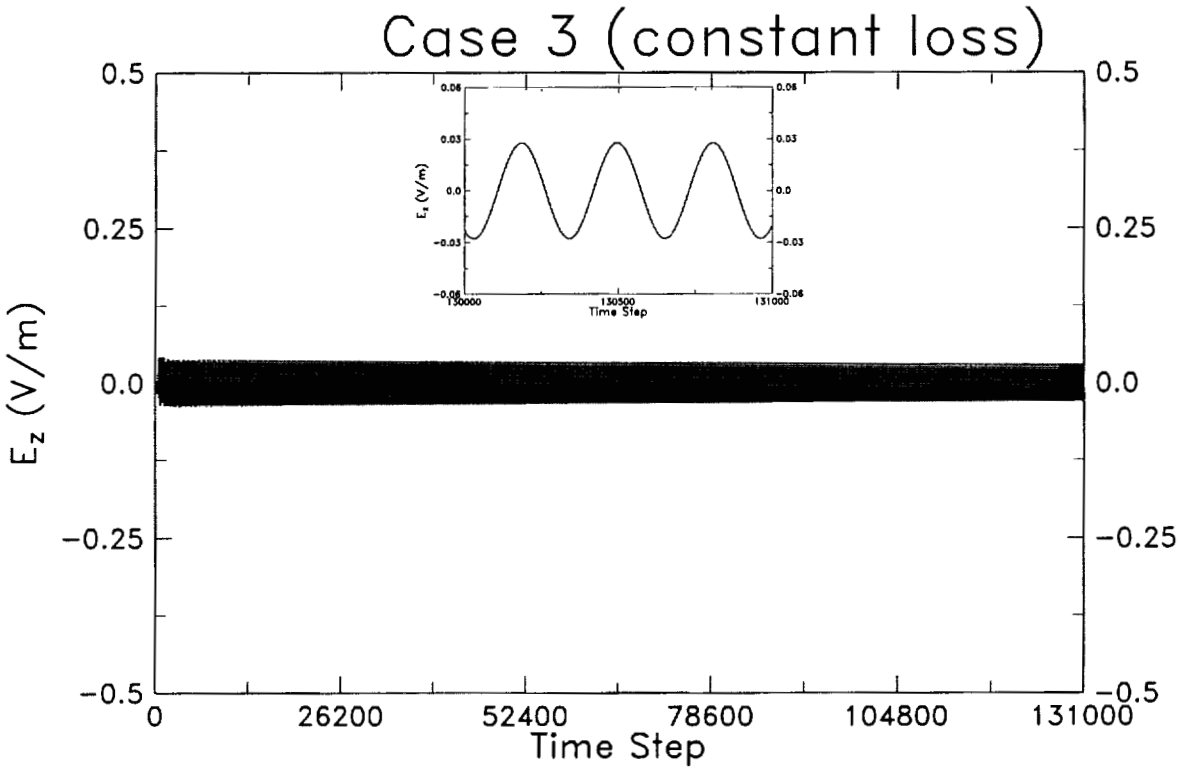

Figure 2.12: The time-domain electric field at the center of the enclosure for Case #3 and with the free-space cells of the FDTD solution space artificially assigned a conductivity of 0.000001 S/m. The fields have decayed only slightly more than those of the lossless case after 131,000 time steps.

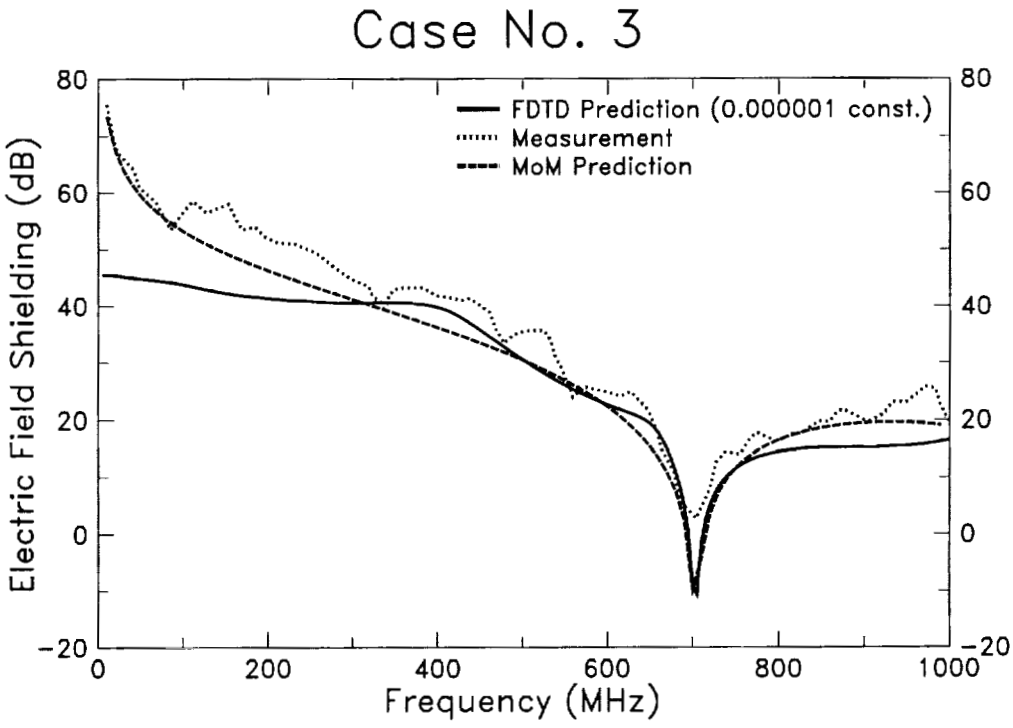

Figure 2.13: A comparison of the electric field shielding at the center of the enclosure for Case #3 between FDTD prediction (with a constant 0.000001 S/m artificial conductivity assigned to the free-space cells), MoM prediction, and measurement.

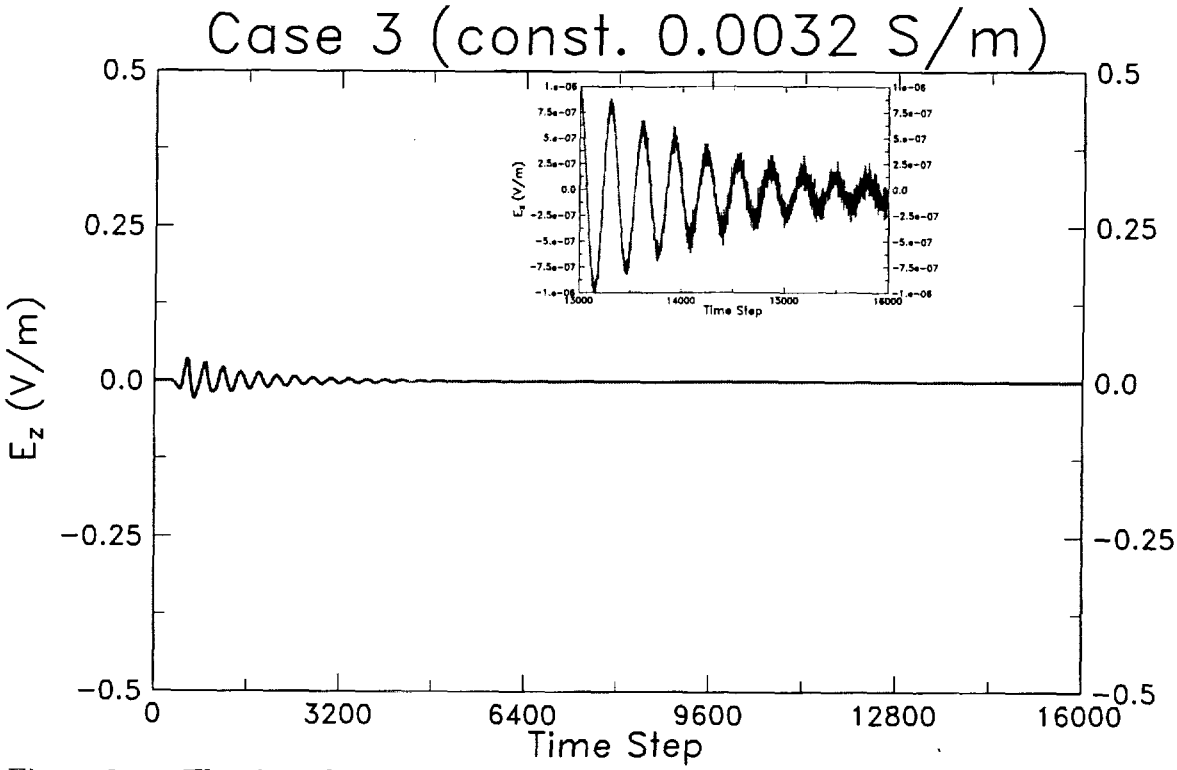

Figure 2.14: The time-domain electric field at the center of the enclosure for Case #3 with the free-space cells of the FDTD solution space artificially assigned a conductivity of 0.0032 S/m. The fields have decayed almost to zero after only 16,000 time steps.

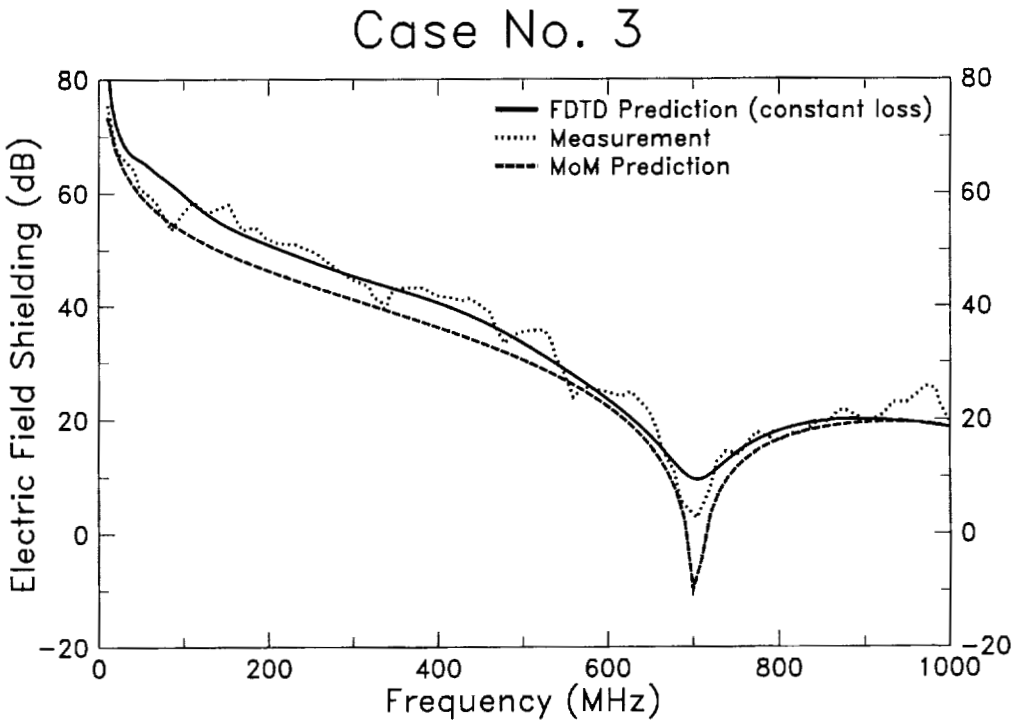

Figure 2.15: A comparison of the electric field shielding at the center of the enclosure for Case #3 between FDTD prediction (with a constant 0.0032 S/m artificial conductivity assigned to the free-space cells), MoM prediction, and measurement.

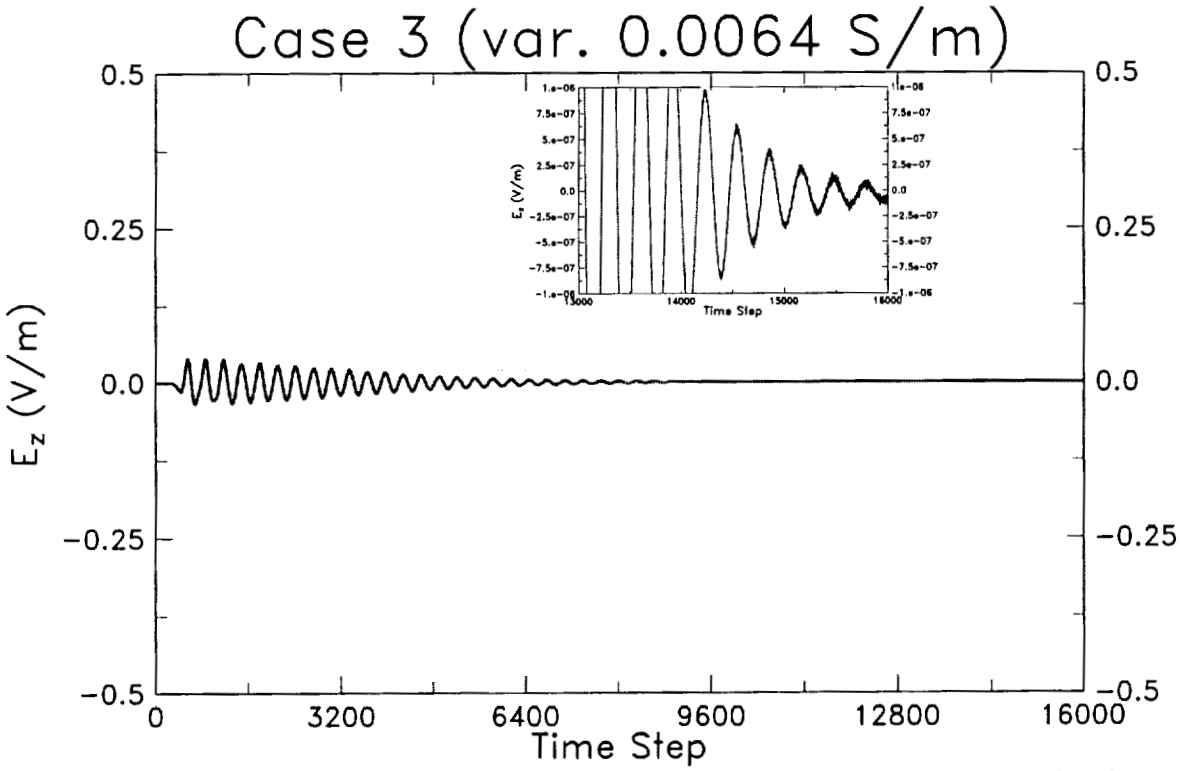

Figure 2.16: The time-domain electric field at the center of the enclosure for Case #3 and with the free-space cells of the FDTD solution space artificially assigned a linearly increasing conductivity as a function of time steps. The fields have decayed to nearly zero after only 16,000 time steps.

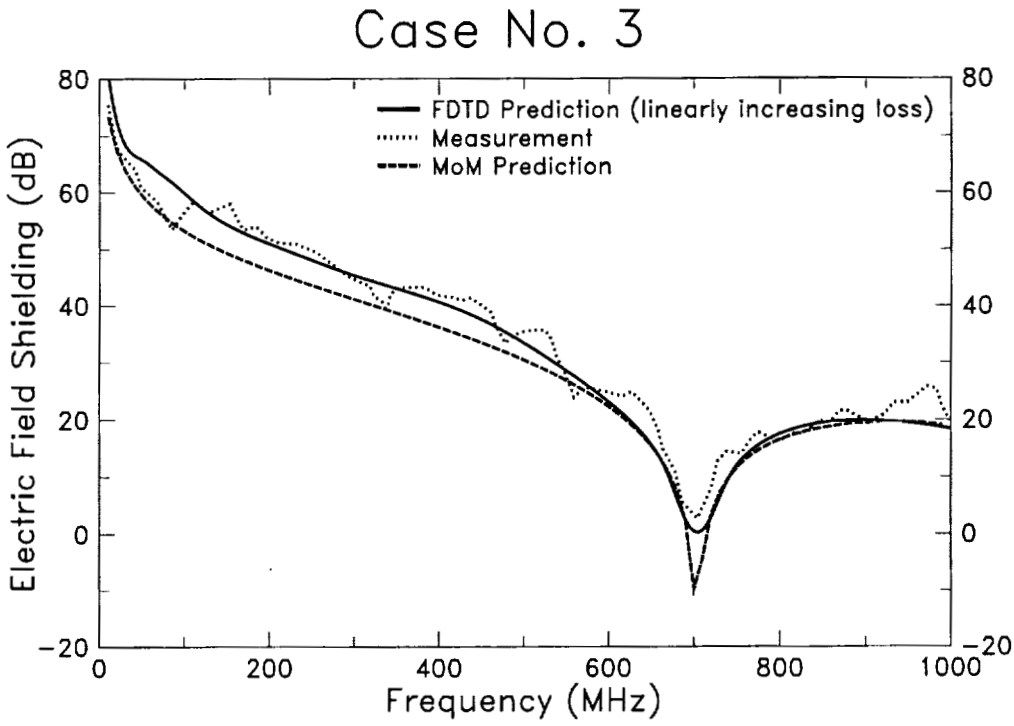

Figure 2.17: A comparison of the electric field shielding at the center of the enclosure for Case #3 between FDTD prediction (with a linearly increasing artificial conductivity assigned to the free-space cells), MoM prediction, and measurement. The agreement is excellent.

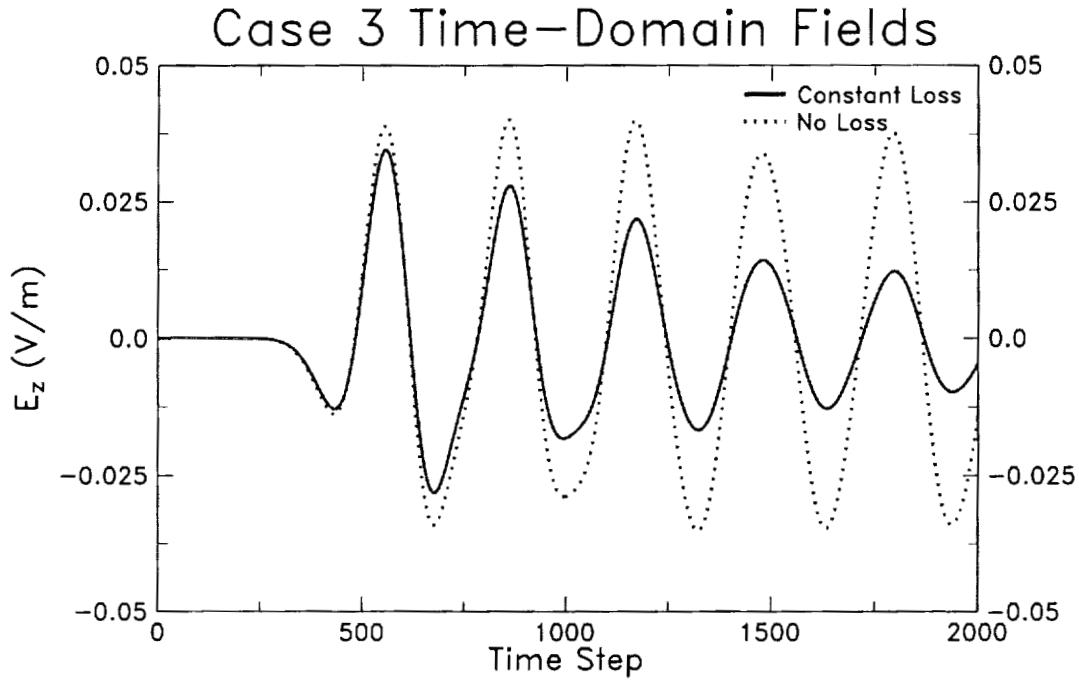

Figure 2.18: A comparison of the initial time-domain electric fields at the center of the enclosure for Case #3. The solid line corresponds to the case of the free-space cells being assigned a constant artificial conductivity of 0.0032 S/m. The patterned line is for the lossless case. Note that differences between the two curves occur very early in the simulation.

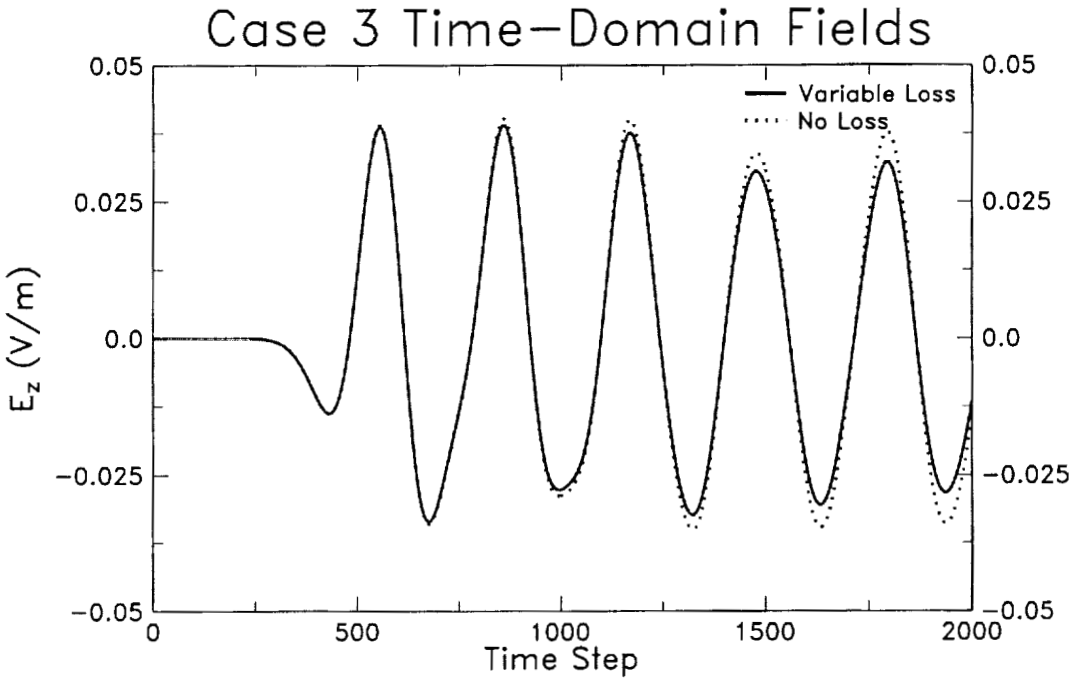

Figure 2.19: A comparison of the initial time-domain electric fields at the center of the enclosure for Case #3. The solid line corresponds to the case of the free-space cells being assigned a linearly increasing artificial conductivity. The patterned line is for the lossless case. Note that there is little difference between the two curves for the first few thousand time steps.

Chapter 3

Analysis of Cavity-Backed Slot Antennas: FDTD, FEM & Measurements

I. Introduction

Mutual coupling between cavity-backed slot (CBS) antennas mounted on a ground plane has been examined in the past using the Finite-Difference Time-Domain (FDTD) method and a hybrid Finite Element Method/Method of Moments (FEM/MoM) approach. Predictions were compared with measurements performed in the Electro-Magnetic Anechoic Chamber (EMAC) facility at Arizona State University. In this report, simulation issues related to the modeling of CBS antennas with either FDTD or FEM/MoM are described. Furthermore, additional numerical results are presented and compared with measurements.

Initially, FDTD modeling of CBS antennas is discussed, including an efficient source implementation for single elements and its extension to multiple elements. Then, the hybrid FEM/MoM approach is briefly described and its advantages are outlined. In the last section, FDTD and FEM/MoM are used to compute the input impedance of a CBS antenna and coupling between two identical CBS antennas. Finally, some parametric studies of coupling are performed using the hybrid FEM/MoM code.

II. FDTD Modeling

A. Source Implementation

The computation of the input impedance of an antenna or the network parameters of a system of antennas involves the Fourier transform of the input voltages and currents. Therefore, using a transient excitation (pulse) the impedance or the network parameters can be determined over a frequency band by fast Fourier transforming (FFT) the time-domain data. The basic requirement for the FFT to work is to allow enough simulation time for the transient phenomena to decay. However, one of the main difficulties involved in FDTD simulations is that in some applications, e.g., resonant lossless structures, tens or even hundreds of time-steps may be required for the transient fields to decay.

The voltage source that is used in FDTD simulations is commonly connected directly to the antenna; *hard* voltage source. This source is usually a pulse with a significantly greater than zero amplitude, only for a very short fraction of the total computation time. When the pulse amplitude drops essentially to zero, the source becomes effectively a short circuit. Consequently, any reflections from the antenna towards the source are totally reflected back. Additionally, the energy that is introduced in the computational space can be dissipated by either radiation, or absorption due to the presence of lossy media or lumped elements. For resonant structures, this radiation or absorption process may require a long time to dissipate the excitation energy.

Many attempts have been recently made in order to reduce the required simulation time. A transient source for a microstrip line was introduced in [3]. This source is located near the FDTD outer boundary and when its amplitude falls to zero, the source is removed and replaced with a FDTD absorbing boundary. The main disadvantages of this method are that it can not be explicitly applied to arbitrary geometries, and the feed location should be far enough from any geometrical features so that no reflections return to the feed location before the source is replaced with the absorbing boundary. A similar approach has been applied to antennas that are fed by a coaxial cable. Instead of introducing an absorbing boundary during the calculation, a portion of the coaxial cable terminated in an absorbing boundary is

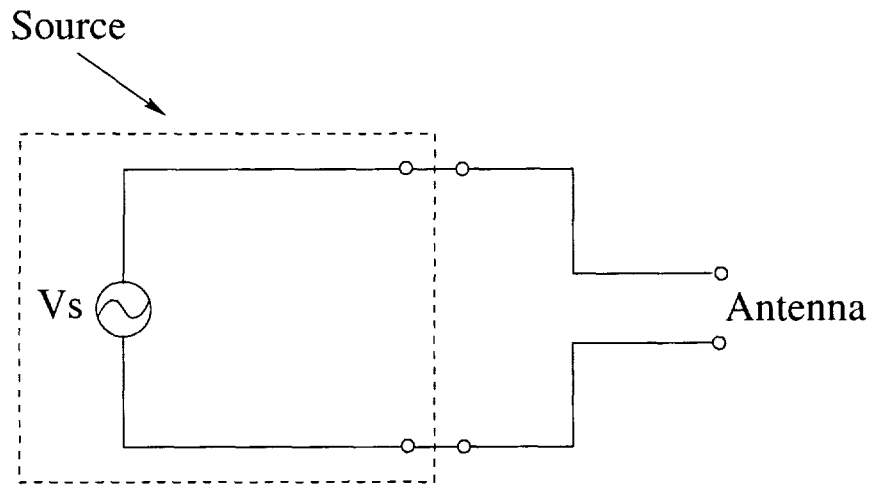

Figure 3.1: Voltage source.

included in the FDTD calculation [4], [5]. It is reported in [5] that this approach is preferable to the gap source described in [6], since the fields decay more rapidly when the explicit coaxial cable is used. Furthermore, a more involved technique that reduces the simulation time is based on the use of signal processing methods to predict the voltages and currents at later times based on manipulation of computed results at earlier times. This technique [7],[8] proposes the truncation of the FDTD computations at a given time and use of the already calculated results to predict the ones at future times. However, the utilization of prediction methods increases the complexity of the FDTD calculation process (post-processing). Additionally, the prediction methods are complicated and their accuracy depends significantly on the choice of order of the prediction technique, which has to be made by the user and is not a trivial matter.

A novel, effective and very simple technique to implement for reducing the simulation time is based on a source with an internal resistance that provides the excitation. Initially, this method was used in [9] to excite microstrip patch antennas. In addition, the expression for a voltage source with an internal resistance in parallel with the free-space capacitance of the FDTD cell is given in [10]. However, the advantages of this method were illustrated and outlined explicitly only in [11].

Consider the excitation of an FDTD computational region with a voltage source at a certain mesh position (i_s, j_s, k_s). Figure 3.2 shows the equivalent circuit of a voltage source with an internal source resistance R_s. The voltage at the output port

of the source, which is fed to the antenna, can be easily computed by applying Ohm's Law to the circuit of Figure 3.2

$$V_{out} = V_s - I_s R_s \tag{3.1}$$

where I_s is the current flowing through the source which is equal with the current at the input port of the antenna. This current can be computed using the integral form of Ampère's law. Obviously, the input impedance of the antenna is calculated from the following equation:

$$Z_{in}(\omega) = \frac{V_{out}(\omega)}{I_s(\omega)} \tag{3.2}$$

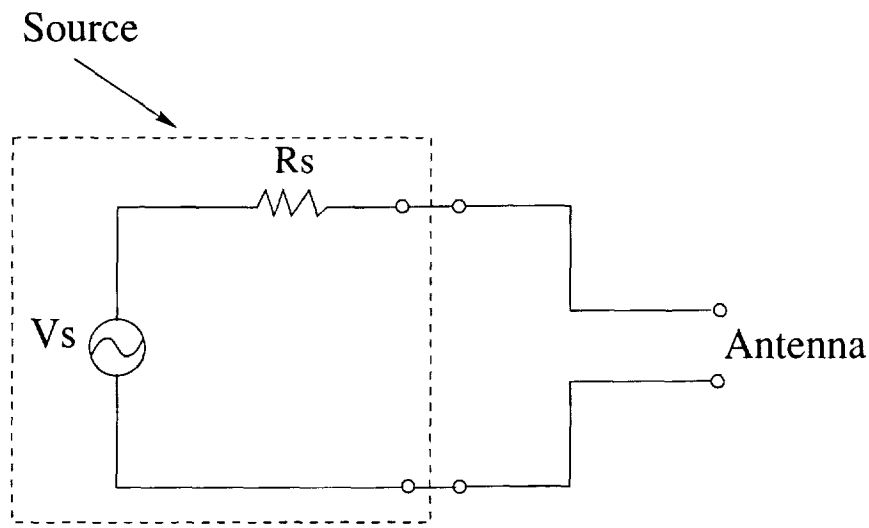

Figure 3.2: Voltage source with intrinsic resistance.

The source resistance cannot be chosen very large, otherwise instabilities may occur due to neglecting the displacement current through the FDTD cell containing the source. This problem can be encountered by judicious choices of the values of the resistance or by taking into account the capacitance of the FDTD cell as discussed in [10]. A reasonable choice for R_s is the value of the characteristic impedance of the transmission line; e.g., 50 ohms for a standard coaxial cable.

B. Illustration of the effectiveness of the resistive voltage source

In order to illustrate the effectiveness of the use of a voltage source with an internal resistance, it was decided to compute the input impedance of an air-filled cavity-

backed slot antenna analyzed in [12]. A three-dimensional (3-D) view of the cavity under consideration is demonstrated in Figure 3.3 and a detailed description of the geometry is shown in Figure 3.4. The input impedance of the cavity-backed slot antenna was measured in the Electromagnetic Anechoic Chamber facility at Arizona State University. In the experiment, the aperture antenna was mounted on a finite ground plane of dimensions 24×24 in and the sharp edges were covered with absorbing material to reduce diffractions. Additionally, the antenna was rotated at an angle with respect to the principal axes and offset relative to the center of the ground, to direct the diffractions away from the aperture. Moreover, the input impedance of the same aperture mounted on an infinite ground plane was calculated in [12] using a hybridization of the Finite Element Method (FEM) with the Moment Method (MoM) and compared very well with measurements; showing that the dimensions of the ground plane do not have a profound effect on the value of the input impedance.

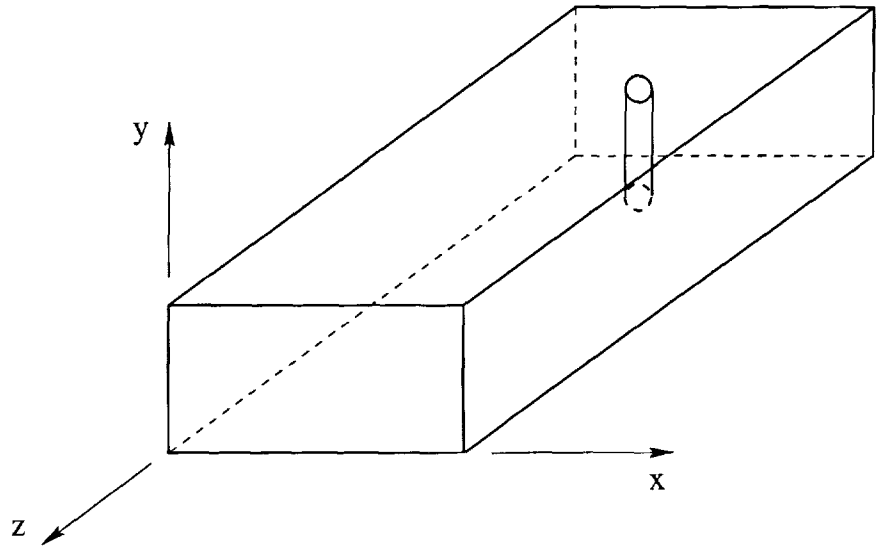

Figure 3.3: A three-dimensional view of an air-filled rectangular cavity-backed slot antenna fed with a probe oriented in the y-direction.

In the FDTD simulations, this aperture antenna was mounted on a 9×9 cm finite ground plane, which is smaller than the one used in the measurements to reduce the size of the computational space. In order to determine the input impedance of the antenna, the voltage and current at the feeding probe of the cavity-backed slot antenna have to be computed. The simulation time should allow the transient effects

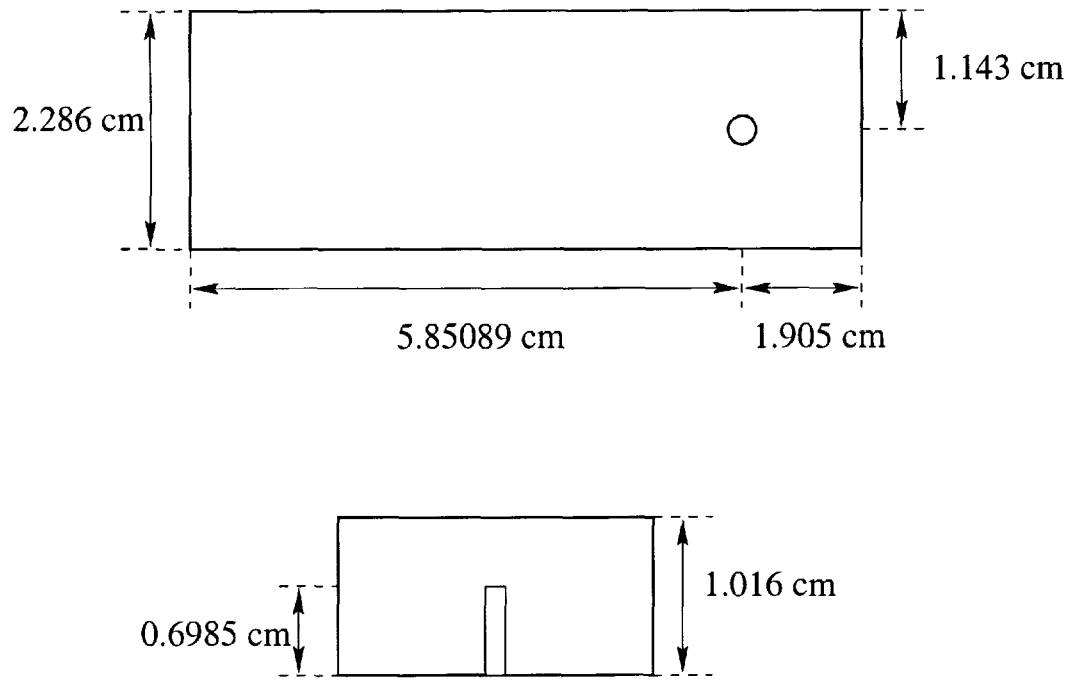

Figure 3.4: A two-dimensional view of an air-filled rectangular cavity-backed slot fed with a probe oriented in the y-direction.

in both the voltage and current to decay so that they can be accurately Fourier transformed. As discussed previously, the voltage is a user defined function of time that decays quickly to zero, whereas the current may need a long time to decay. Two FDTD simulations were performed, and for both the cell size was 1.5 mm whereas the probe was excited with a voltage Rayleigh pulse. In the first case, the voltage source had zero internal resistance ($R_s = 0$), and in the second case, R_s was set equal to 50 ohms. Figs. 3.5 and 3.6 show the computed current at the probe exciting the cavity for the two cases, respectively. Obviously, the current in the case with no internal resistance ($R_s = 0$) did not decay to zero even after 64,000 time steps, indicating the resonant behavior and the high quality factor, Q, of the antenna. On the contrary, in the second simulation, the source current converged to zero very fast and the FDTD calculation time reduced significantly.

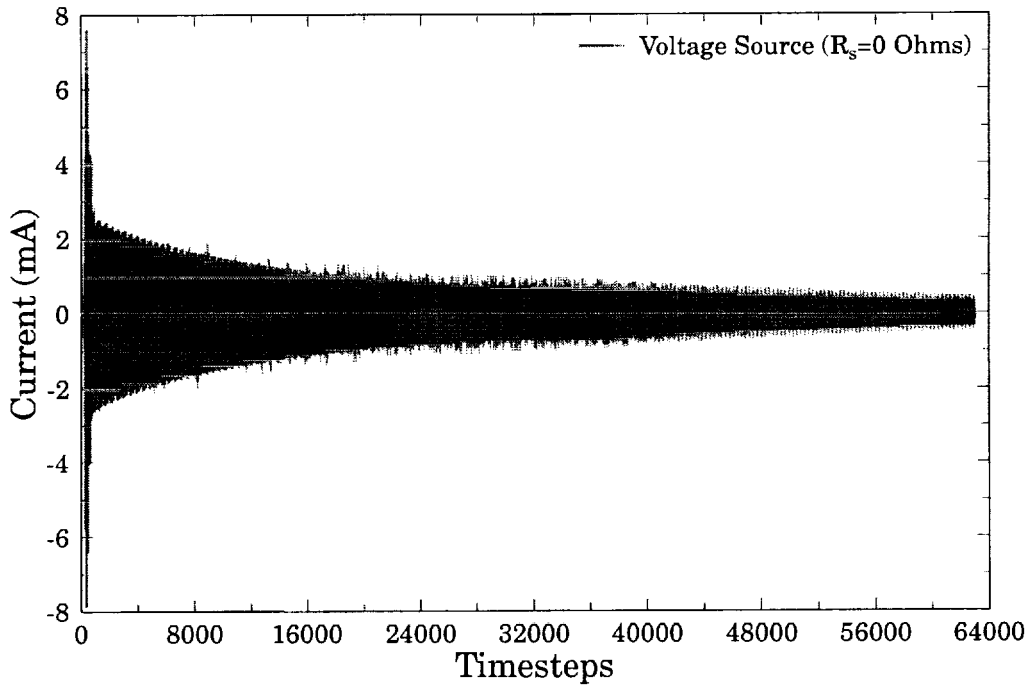

Figure 3.5: Current of the probe exciting the cavity-backed slot antenna for $R_s = 0$

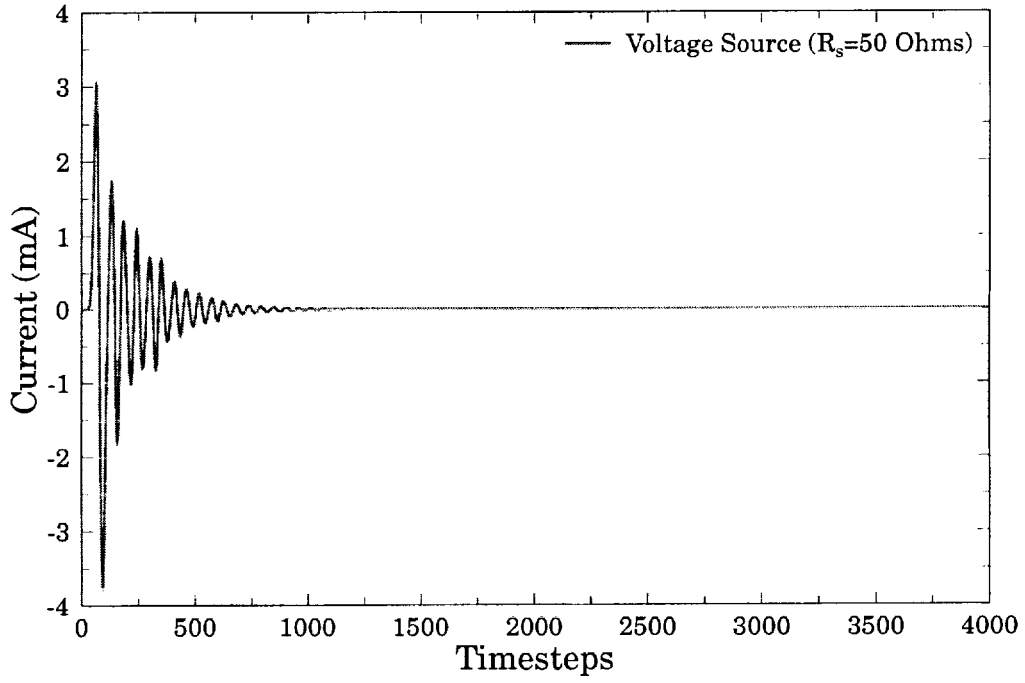

Figure 3.6: Current of the probe exciting the cavity-backed slot antenna for $R_s =$ 50 ohms

C. Calculation of the ABCD-parameters using a voltage source with internal resistance

In the previous section a voltage source with an internal resistance was used to efficiently compute the input impedance of an antenna. However, when a problem involves the calculation of the network parameters of a system of antennas, then a modified approach should be used. Here, because our analysis is related to mutual coupling between two antennas, only the evaluation of two-port network parameters will be considered. The computation time required for the calculation of the two-port network parameters that model a system of two antennas can be substantially reduced by using a voltage source with an internal resistance. The augmented system of two generic antennas along with the voltage sources is shown in Figure 3.7. This system can be thought of as the cascade connection of three two-port networks, as illustrated in Figure 3.7.

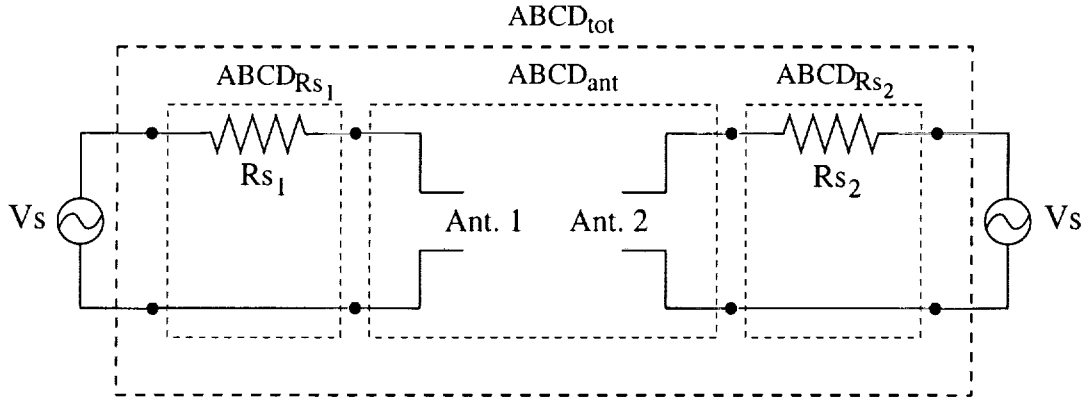

Figure 3.7: Augmented system of two generic antennas with voltage sources.

The proposed approach requires to initially compute the Y-parameters of the entire system including the antennas and the load resistors. Then, the Y-parameters of the system are converted to ABCD-parameters. It is known that the ABCD matrix of the cascade connection of two-port networks is equal to the product of the ABCD matrices representing the individual two ports. Note also, that the order of matrix multiplication must correspond to the order in which the networks are arranged, since matrix multiplication is not, in general, commutative. Therefore, the ABCD matrix of the entire system is equal to the product of the ABCD matrices of each sub-network

and can be written as

$$\begin{bmatrix} A_{tot} & B_{tot} \\ C_{tot} & D_{tot} \end{bmatrix} = \begin{bmatrix} A_{R_{s1}} & B_{R_{s1}} \\ C_{R_{s1}} & D_{R_{s1}} \end{bmatrix} \begin{bmatrix} A_{ant} & B_{ant} \\ C_{ant} & D_{ant} \end{bmatrix} \begin{bmatrix} A_{R_{s2}} & B_{R_{s2}} \\ C_{R_{s2}} & D_{R_{s2}} \end{bmatrix} \tag{3.3}$$

where $ABCD_{R_{s1}}$ and $ABCD_{R_{s2}}$ are the ABCD matrices of the series resistances R_{s1} and R_{s2}, respectively, and $ABCD_{ant}$ is the ABCD matrix of the overall antenna system. The ABCD parameters of a two-port network consisting of a series impedance Z between ports 1 and 2 (see Figure 3.8) are given by

$$\begin{bmatrix} A_Z & B_Z \\ C_Z & D_Z \end{bmatrix} = \begin{bmatrix} 1 & Z \\ 0 & 1 \end{bmatrix} \tag{3.4}$$

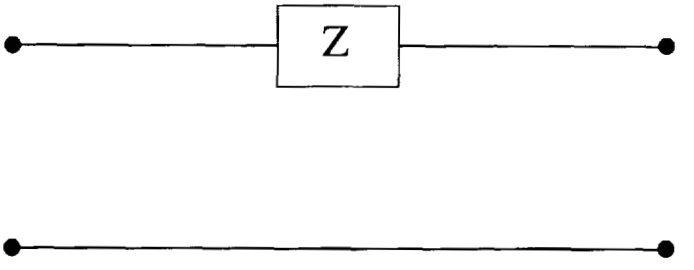

Figure 3.8: Two-port network consisting of a series impedance Z.

Consequently, the ABCD matrices denoted as $ABCD_{R_{s1}}$ and $ABCD_{R_{s2}}$ are given by

$$\begin{bmatrix} A_{R_{s1}} & B_{R_{s1}} \\ C_{R_{s1}} & D_{R_{s1}} \end{bmatrix} = \begin{bmatrix} 1 & R_{s1} \\ 0 & 1 \end{bmatrix} \tag{3.5}$$

$$\begin{bmatrix} A_{R_{s2}} & B_{R_{s2}} \\ C_{R_{s2}} & D_{R_{s2}} \end{bmatrix} = \begin{bmatrix} 1 & R_{s2} \\ 0 & 1 \end{bmatrix} \tag{3.6}$$

whereas the ABCD matrix of the overall antenna system, $ABCD_{ant}$, can be computed by the following expression:

$$\begin{bmatrix} A_{ant} & B_{ant} \\ C_{ant} & D_{ant} \end{bmatrix} = \begin{bmatrix} A_{R_{s1}} & B_{R_{s1}} \\ C_{R_{s1}} & D_{R_{s1}} \end{bmatrix}^{-1} \begin{bmatrix} A_{tot} & B_{tot} \\ C_{tot} & D_{tot} \end{bmatrix} \begin{bmatrix} A_{R_{s2}} & B_{R_{s2}} \\ C_{R_{s2}} & D_{R_{s2}} \end{bmatrix}^{-1} \tag{3.7}$$

The computed $ABCD_{ant}$ matrix of the two antennas can be converted, if needed, to any of the other type of two-port network parameters using the appropriate conversion formulas. Following the method described, computation of the ABCD parameters of the two antennas can lead to great savings in the computational time.

III. FEM/MoM Hybrid Approach

A vector finite element method (FEM) hybridized with the method of moments (MoM) is used in the analysis of cavity-backed slot (CBS) antennas. The FEM, which is based on linear tetrahedral elements, solves for the electric field distribution inside the cavity or cavities, since we are interested in coupling. A spectral domain MoM is implemented through the continuity of the tangential magnetic field in the aperture(s) to solve for the field distribution in the exterior region; note that the cavity(ies) is(are) mounted on an infinite ground plane with a possible dielectric/magnetic overlay. The main drawback of the spectral domain MoM is that it becomes extremely slow with increasing the number of edges in the aperture(s). This problem is overcome by using an asymptotic extraction of the exponential behavior of the Green's function; the asymptotic part is evaluated using a computationally efficient spatial domain integration. The excitation is based on either a plane wave incidence (scattering problem) or a coaxial feed model (radiation problem) implemented using the FEM. The radar cross section (RCS), input impedance, return loss, and gain versus frequency can be conveniently and efficiently calculated using the hybrid formulation.

A. FEM/MoM formulation

A two-dimensional (2-D) view of a CBS antenna mounted on an infinite ground plane coated with a dielectric layer is depicted in Figure 3.9. A vector FEM is implemented for the solution of the source-free Helmholtz's equation

$$\nabla \times \left([\mu_r]^{-1} \cdot \nabla \times \mathbf{E} \right) - k_\circ^2 \, [\epsilon_r] \, \mathbf{E} = 0 \tag{3.8}$$

inside the cavity volume (Ω), where $[\epsilon_r]$ and $[\mu_r]$ are, respectively, the permittivity and permeability tensors of the domain, and $\mathbf{E}$ is the unknown electric field. Full-tensor representation of ϵ_r and μ_r allows electromagnetic modeling of frequency dependent anisotropic materials. Dirichlet boundary conditions are imposed on all perfectly conducting surfaces, which implies that $\hat{n} \times \mathbf{E} = 0$ on cavity walls. Using this boundary condition and the well-known Galerkin's approach, the Helmholtz's equation can be

written in a weak integral form given by

$$\iiint_{\Omega}([\mu_r]^{-1}\nabla\times\mathbf{E})\cdot(\nabla\times\mathbf{W})\,dV \;-\; k_\circ^2\iiint_{\Omega}[\epsilon_r]\cdot\mathbf{E}\cdot\mathbf{W}\,dV$$

$$+\; jk_\circ\eta_\circ\iint_S\mathbf{H}\cdot(\mathbf{W}\times\hat{a}_z)\,dA=0 \quad (3.9)$$

where $\mathbf{W}$ is the chosen testing function, $k_\circ$ is the free-space propagation constant, $\eta_\circ$ is the free-space intrinsic impedance, and S denotes the area of the cavity aperture.

For scattering, a linearly polarized plane wave, denoted by $\mathbf{H}^{inc}$, is incident on the aperture plane at an angle θ_i with respect to the normal vector and ϕ_i with respect to the x-axis. By imposing the boundary condition that the tangential magnetic field must be continuous across the aperture plane, one may write

$$\mathbf{H}=\mathbf{H}^{inc}+\mathbf{H}^{ref}+\frac{1}{4\pi^2}\iint_{-\infty}^{\infty}\widetilde{\mathbf{M}}(k_x,k_y)\cdot\overline{\overline{\widetilde{\mathbf{G}}}}\,(k_x,k_y,z|0)\,e^{j(k_xx+k_yy)}\,dk_xdk_y \quad (3.10)$$

where $\mathbf{H}^{ref}$ is the magnetic field reflected by the coated ground plane in the absence of the aperture, $\overline{\overline{\widetilde{\mathbf{G}}}}$ is the spectral dyadic Green's function for a coated conducting ground plane in the presence of a magnetic current source at the origin, and $\widetilde{\mathbf{M}}$ is the Fourier transform of the magnetic current $(\mathbf{E}\times\hat{a}_z)$ just above the aperture. Substituting (3.10) into (3.9) and utilizing the inverse Fourier transform in conjunction with the definition that $\mathbf{T}=\mathbf{W}\times\hat{a}_z$, the weak form of Helmholtz's equation can be expresses as

$$\iiint_{\Omega}([\mu_r]^{-1}\nabla\times\mathbf{E})\cdot(\nabla\times\mathbf{W})\,d\Omega-k_\circ^2\iiint_{\Omega}[\epsilon_r]\mathbf{E}\cdot\mathbf{W}\,d\Omega$$

$$-\;\frac{jk_\circ\eta_\circ}{4\pi^2}\iint_{-\infty}^{\infty}\widetilde{\mathbf{M}}(k_x,k_y)\cdot\overline{\overline{\widetilde{\mathbf{G}}}}\,(k_x,k_y,z|0)\cdot\tilde{\mathbf{T}}(-k_x,-k_y)\,dk_xdk_y$$

$$=\;jk_\circ\eta_\circ\iint_S(\mathbf{H}_{tan}^{inc}+\mathbf{H}_{tan}^{ref})\cdot\mathbf{T}\,dA \quad (3.11)$$

The finite element volume is discretized with tetrahedrons and the aperture with triangles. Thus, the electric field $(\mathbf{E})$ inside the cavity is expanded in terms of a set of basis functions $\mathbf{W}_i$'s and the magnetic current $(\mathbf{M})$ in the aperture is expanded in terms of another set of basis functions $\mathbf{T}_i$'s, where i corresponds to a global edge number. The second type of basis functions ($\mathbf{T}_i$'s) were originally proposed by Rao *et*

al. [13]. These are very similar to $\mathbf{W}_i$'s with the only difference being the enforcement of normal continuity, rather than tangential continuity, across edges. The Fourier transform of these triangular basis functions is known in closed form [14].

The integral on the right-hand side of (3.11) represents the excitation vector which is evaluated using a pure spectral domain approach. The spectral integral on the left-hand side of (3.11) represents the admittance matrix for the exterior region of the cavity. The latter is evaluated using a mixed spectral/spatial domain MoM approach. The exponential behavior of the governing Green's function is numerically extracted to improve the computational speed of the spectral integration. The asymptotic part is evaluated using a spatial integration which is known to be computationally more efficient. Thus, using the asymptotic extraction, the admittance matrix can be expressed in spectral domain as

$$\begin{aligned} Y_{ij} &= -\frac{jk_o\eta_o}{4\pi^2}\iint_{-\infty}^{\infty}\tilde{\mathbf{T}}_i(k_x,k_y)\cdot\left\{\overline{\overline{\tilde{\mathbf{G}}}}\,(k_x,k_y,z|0)-\overline{\overline{\tilde{\mathbf{G}}}}_h\,(k_x,k_y,z|0)\right\} \\ &\qquad\cdot\tilde{\mathbf{T}}_j(-k_x,-k_y)\,dk_xdk_y \\ &\quad -\frac{jk_o\eta_o}{4\pi^2}\iint_{-\infty}^{\infty}\tilde{\mathbf{T}}_i(k_x,k_y)\cdot\overline{\overline{\tilde{\mathbf{G}}}}_h\,(k_x,k_y,z|0)\cdot\tilde{\mathbf{T}}_j(-k_x,-k_y)\,dk_xdk_y \end{aligned} \tag{3.12}$$

where $\overline{\overline{\tilde{\mathbf{G}}}}_h$ is the dyadic Green's function of a homogeneous space with $\epsilon_r = \epsilon_r^d$ and $\mu_r = \mu_r^d$ (ϵ_r^d and μ_r^d referred to the dielectric coating), and $\tilde{\mathbf{T}}_i$ is the Fourier transform of the i^{th} basis function. The first integral in (3.12), denoted as $\tilde{Y}_{ij}$, is evaluated using a pure spectral domain approach after converting to polar coordinates. The second integral in (3.12), denoted as Y_{ij}^H, is evaluated using a spatial, instead of spectral, domain MoM

$$\begin{aligned} Y_{ij}^H &= -2k^2\int_{A_i}\mathbf{T}_i(\mathbf{r})\cdot\left[\int_{A_j}\mathbf{T}_j(\mathbf{r}')\,G_h(\mathbf{r},\mathbf{r}')\,dA'\right]dA \\ &\quad + 2\int_{A_i}\nabla\cdot\mathbf{T}_i(\mathbf{r})\left[\int_{A_j}G_h(\mathbf{r},\mathbf{r}')\nabla'\cdot\mathbf{T}_j(\mathbf{r}')\,dA'\right]dA \end{aligned} \tag{3.13}$$

where A_i (A_j) is the triangle supporting the i^{th} (j^{th}) basis function, $\mathbf{r}$ ($\mathbf{r}'$) is the position vector, and G_h is the Green's function for a homogeneous medium with $\epsilon_r = \epsilon_r^d$ and $\mu_r = \mu_r^d$.

Once the unknowns (non-PEC edges) inside the cavity and aperture are assembled, a linear system of equations is formed

$$\begin{bmatrix} M^{c/c} & M^{c/a} \\ M^{a/c} & M^{a/a} + Y^{a/a} \end{bmatrix} \begin{bmatrix} E^c \\ E^a \end{bmatrix} = \begin{bmatrix} 0 \\ b^a \end{bmatrix}$$

where $[M]$ represents the finite element matrix given by

$$M_{ij} = \iiint_\Omega (\nabla \times \mathbf{W}_i) \cdot [\mu_r]^{-1} \cdot (\nabla \times \mathbf{W}_j)\, d\Omega - k_o^2 \iiint_\Omega \mathbf{W}_i \cdot [\epsilon_r] \cdot \mathbf{W}_j\, d\Omega \quad (3.14)$$

and $[Y] = [\tilde{Y}] + [Y^H]$; the superscripts c and a, which denote cavity and aperture, respectively, are used to distinguish field interactions between the two regions. The rank of matrix $[M]$ is $N_c + N_a$ where N_c is the number of non-PEC edges inside the cavity, and N_a is the number of non-PEC edges in the aperture. The rank of matrix $[Y]$ is N_a.

The right-hand side vector, which is non-zero only in the aperture plane and expressed by the surface integral in (3.11), can be evaluated very conveniently using the spectral domain approach

$$b_i^a(hard) = \frac{2}{\eta_o} \tilde{G}_\theta^M(k_{xs}, k_{ys}) \cos\theta_i\, e^{jk_o d \cos\theta_i} \left\{ \tilde{T}_{xi}^*(k_{xs}, k_{ys}) \sin\phi_i - \tilde{T}_{yi}^*(k_{xs}, k_{ys}) \cos\phi_i \right\} \quad (3.15)$$

$$b_i^a(soft) = \frac{2}{\eta_o} \tilde{G}_\phi^M(k_{xs}, k_{ys}) \cos\theta_i\, e^{jk_o d \cos\theta_i} \left\{ \tilde{T}_{xi}^*(k_{xs}, k_{ys}) \cos\phi_i + \tilde{T}_{yi}^*(k_{xs}, k_{ys}) \sin\phi_i \right\} \quad (3.16)$$

for hard and soft polarization, respectively; i denotes the global number of an edge in the aperture, * indicates complex conjugate, and

$$k_{xs} = k_o \sin\theta_i \cos\phi_i$$

$$k_{ys} = k_o \sin\theta_i \sin\phi_i. \quad (3.17)$$

The Green's function definitions for $\tilde{G}_\theta^M$ and $\tilde{G}_\phi^M$ as well as additional details in the derivation of (3.15) and (3.16) are provided in [12],[15].

For radiation, the formulation remains the same except for the excitation vector which is formulated in a different way. Instead of plane wave incidence, the antenna is now excited using a coaxial feed model which becomes part of the finite element

domain. The associated formulation for the coaxial feed model and the evaluation of the reflection coefficient at the coax/cavity interface are explicitly given in [12].

The far-zone radiated and/or scattered fields are calculated using the magnetic current distribution in the aperture. Specifically, these are given by

$$E_\theta = \frac{jk_\circ \cos\theta}{2\pi}\frac{e^{-jk_\circ r}}{r}\tilde{G}_\theta^M(k_{xs},k_{ys})\cdot \sum_{j\in A} E_j\left\{-\tilde{T}_{xj}^*(k_{xs},k_{ys})\sin\phi + \tilde{T}_{yj}^*(k_{xs},k_{ys})\cos\phi\right\} \tag{3.18}$$

$$E_\phi = \frac{jk_\circ \cos\theta}{2\pi}\frac{e^{-jk_\circ r}}{r}\tilde{G}_\phi^M(k_{xs},k_{ys})\cdot \sum_{j\in A} E_j\left\{\tilde{T}_{xj}^*(k_{xs},k_{ys})\cos\phi + \tilde{T}_{yj}^*(k_{xs},k_{ys})\sin\phi\right\} \tag{3.19}$$

where A is a triangle in the aperture. Knowing the far-zone fields, antenna characteristics such as RCS, directivity, gain and efficiency can be calculated.

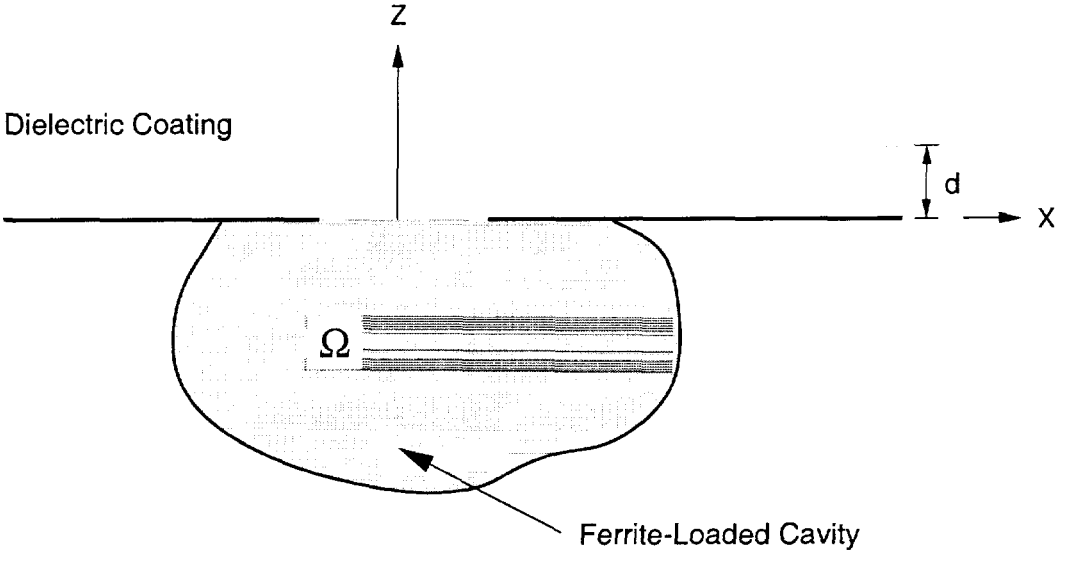

Figure 3.9: Two-dimensional view of a ferrite-loaded cavity-backed slot.

IV. Numerical Calculations

Initially, in order to examine the accuracy of FDTD results computed using a source with an internal resistance, the input impedance of the cavity-backed slot antenna examined in Section II. was computed for three different cases. In all the cases, the feeding probe was excited by a voltage source with R_s equal to 50 ohms. In the first case, the radius of the probe was not modeled (infinitely thin probe) and the cell size was 1.5 mm. In the second case, the radius was taken into account by using the thin-wire model and the cell size was 1.5 mm. In the third case, the cell size was 0.6 mm and the probe itself was discretized along with the rest of the geometry. Fig. 3.10 illustrates the computed input resistance and reactance of the aperture antenna for the three different cases. Also, the FDTD calculations are compared with measurements and with the results based on the hybrid FEM/MoM formulation which were reported in [12]. Obviously, the accuracy of the FDTD results depends greatly on the wire modeling of the probe that excites the antenna. Excellent agreement between the FDTD computations and the measurements is observed in the case where the probe was discretized. The improvement in accuracy for the last case can be attributed to the finer discretization and the enhanced modeling of the probe.

Moreover, the coupling between two identical cavity-backed slot antennas (whose specifications are defined in Fig. 3.4) mounted on a square 9×9 cm ground plane, 25 mm apart from each other, was computed by FDTD and FEM/MoM and the results of the two methods compare very well (see Fig. 3.11 for the geometry specifications and Fig. 3.12 for the coupling calculations). The discrepancies at the higher end of the band can be attributed to discretization errors. In these simulations the FEM mesh consisted of 75,874 elements with average edge size 0.16 cm whereas the FDTD used a cell size of 0.6 mm and a computational domain of $160 \times 160 \times 142$ cells. Notice that two different FDTD methods were used. The first one, denoted as FDTD(2,2), represents a second-order accurate FDTD both in time and space. The second one, denoted as FDTD(2,4), represents a second-order accurate in time and and fourth-order accurate in space FDTD. It can be observed that the FDTD(2,4) scheme does not provide a significant improvement in accuracy compared to the FDTD(2,2) scheme. However, it is expected that as the distance between the two apertures becomes large in terms of the wavelength, FDTD(2,4) will outperform FDTD(2,2).

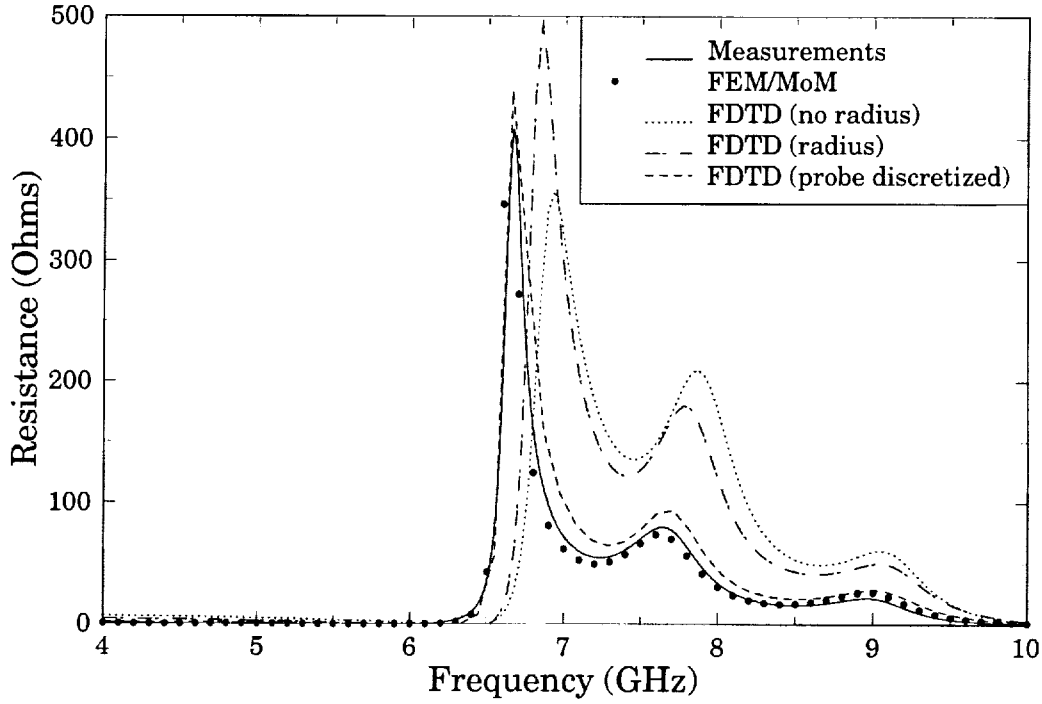

(a)

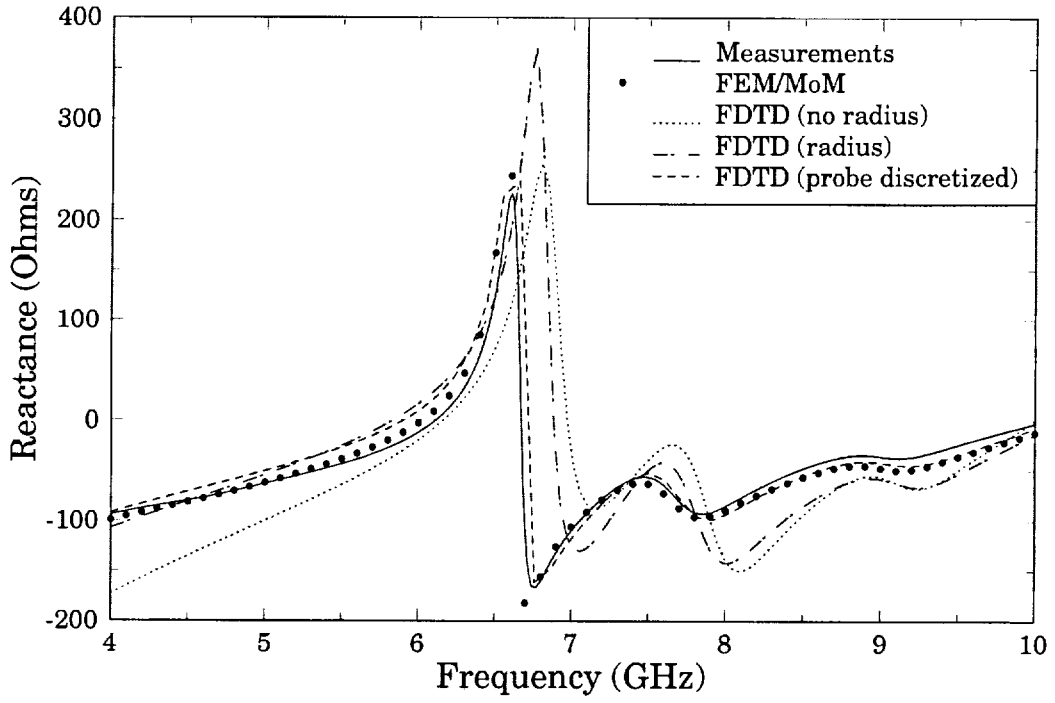

(b)

Figure 3.10: Input impedance of a cavity-backed slot antenna.

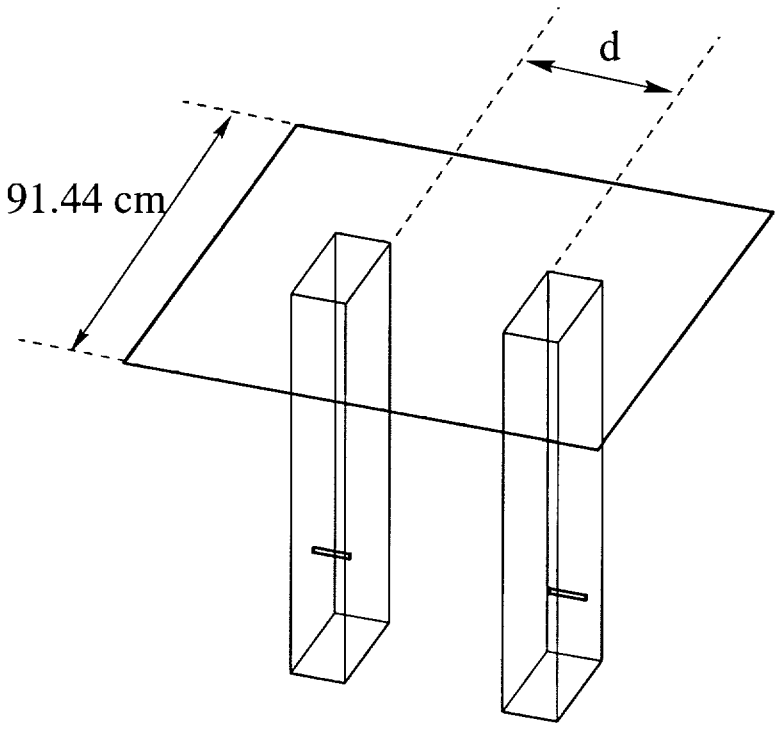

Figure 3.11: Geometry of two identical cavity-backed slot antennas mounted on a square ground plane (for antenna specifications see Figure 1.4).

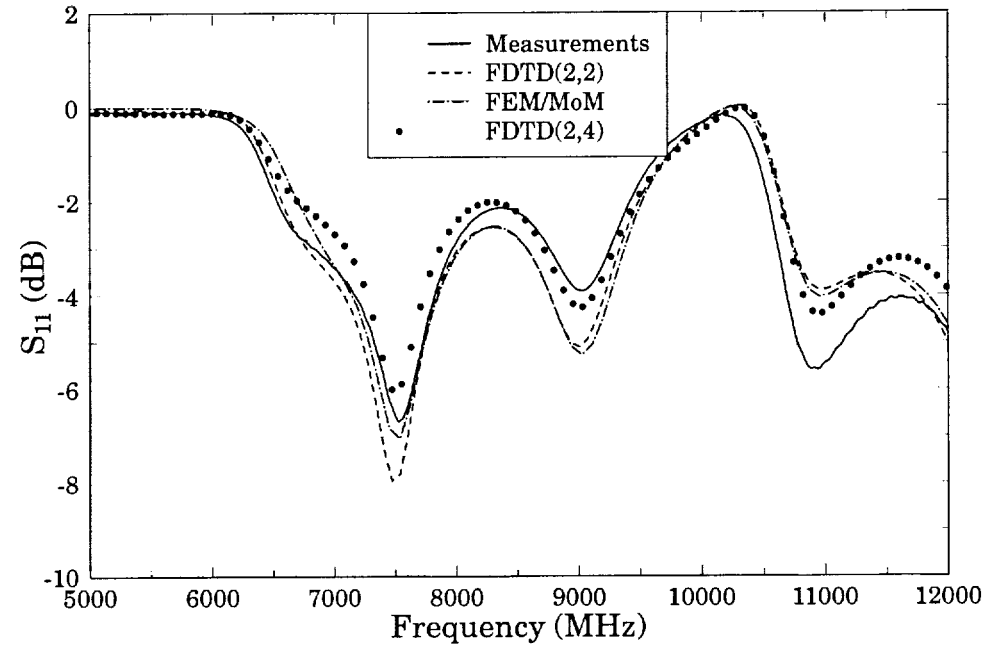

(a)

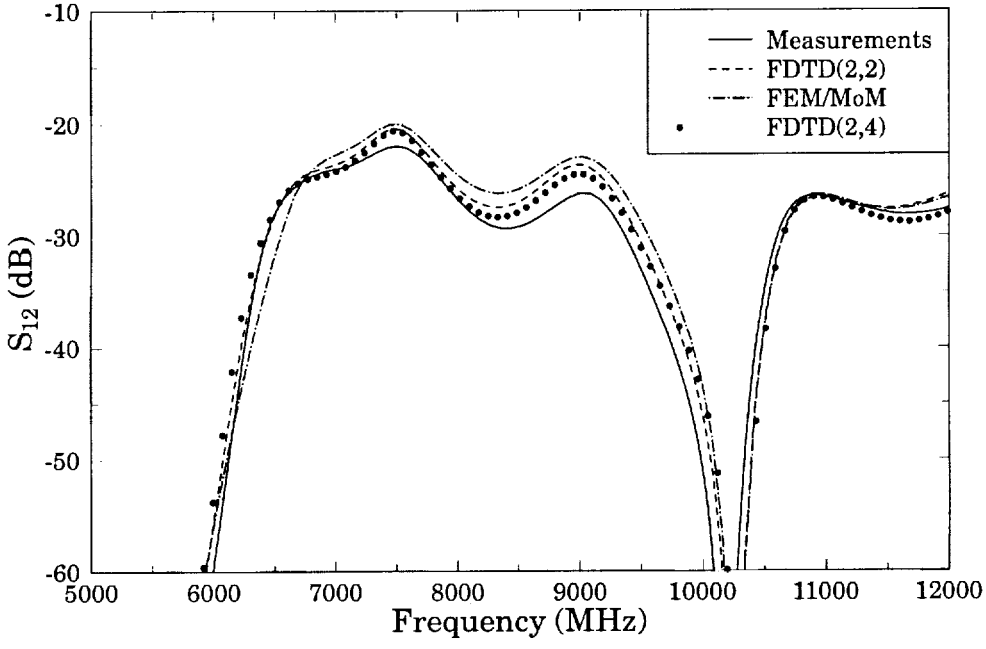

(b)

Figure 3.12: S-parameters of two identical cavity-backed slot antennas mounted on a square ground plane (for antenna specifications see Figure 1.4).

Parametric studies of coupling between two E-plane oriented cavity-backed slot antennas, shown in Fig. 3.13, were performed both numerically and experimentally; d denotes the separation between the two antenna apertures. Only the hybrid FEM/MoM approach was used in these calculations because it was shown to be more efficient and accurate than FDTD. The advantages of FEM/MoM are attributed to the fact that this method does not discretize the space between the two cavities but rather the open-space interaction between the slots is accounted for in the MoM formulation. A sample of the results is illustrated in Figs. 3.14 and 3.15, where the computed coupling of the two antennas is plotted versus separation distance at different frequencies and compared with measurements. It is observed that the coupling between the two antennas diminishes at approximately the same rate as a function of aperture separation at all frequencies. Also, the agreement between the measurements and the FEM/MoM hybrid is excellent considering that the levels of coupling are below -20 dB.

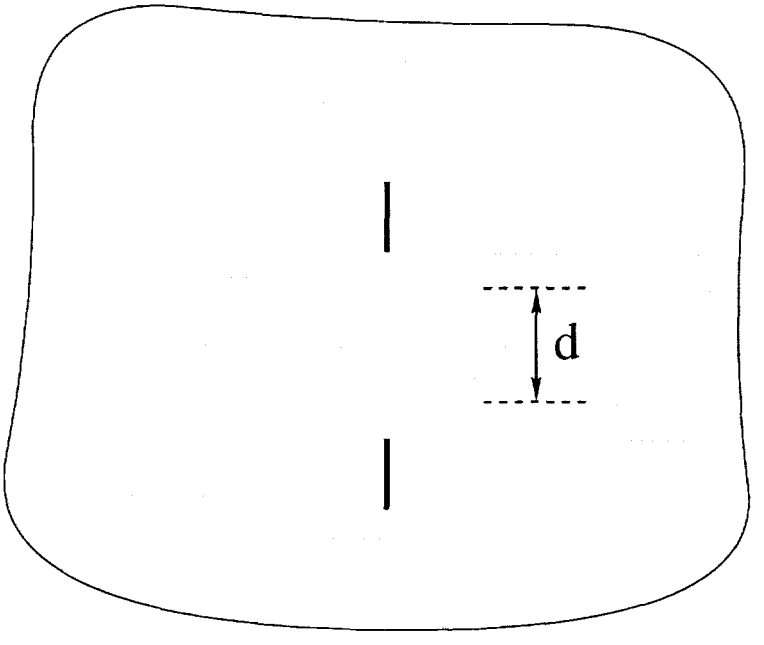

Figure 3.13: Top view of two identical cavity-backed slot antennas mounted on a ground plane (E-plane configuration).

Finally, the FEM/MoM method was used to compute coupling versus separation distance for an echelon configuration of the two identical CBS antennas examined

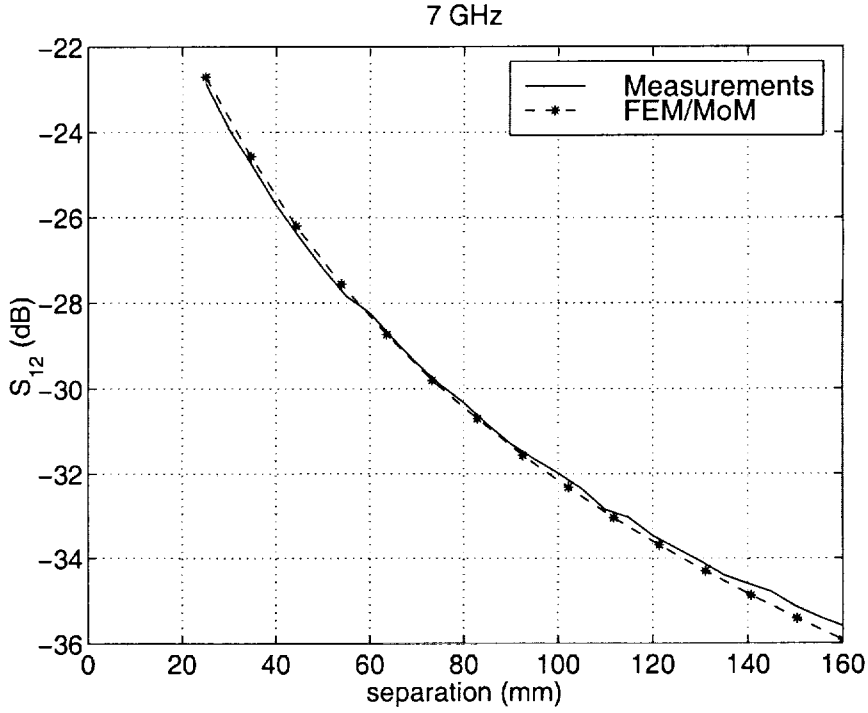

(a)

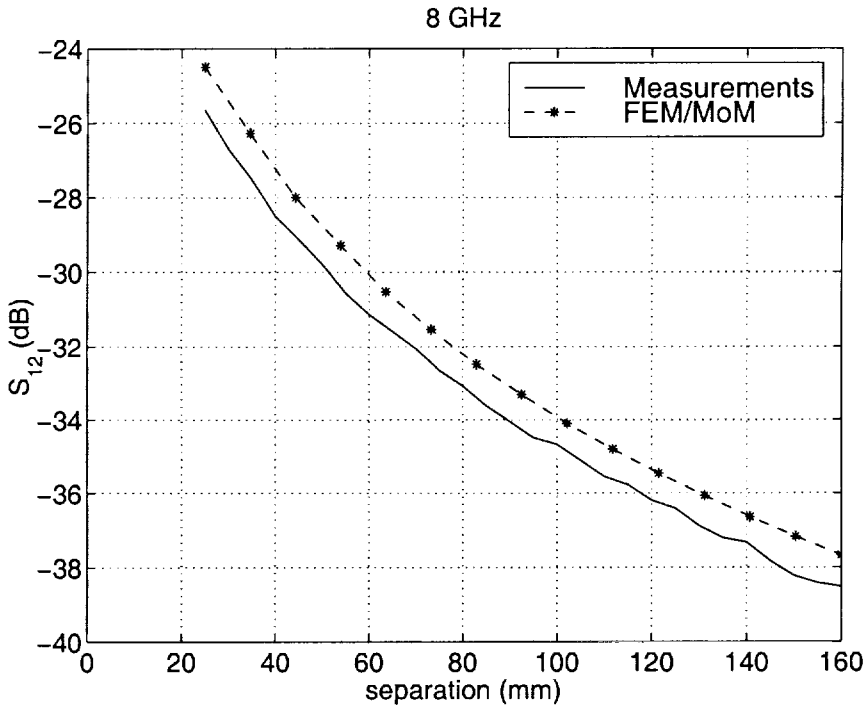

(b)

Figure 3.14: Coupling versus distance for the E-plane configuration at: (a) 7 GHz and (b) 8 GHz.

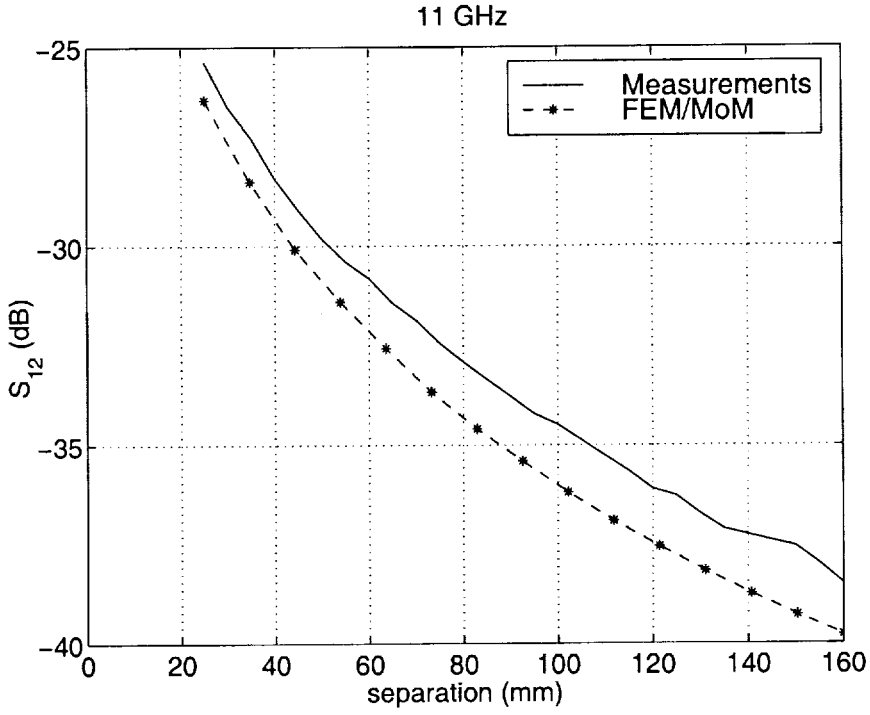

(a)

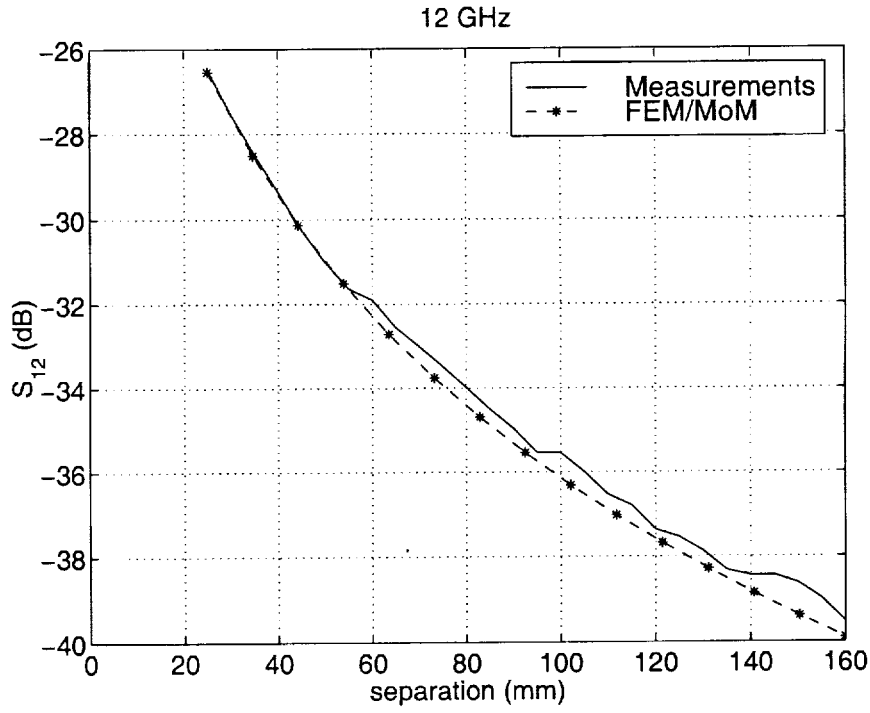

(b)

Figure 3.15: Coupling versus distance for the E-plane configuration at: (a) 11 GHz and (b) 12 GHz.

above (see Figure 3.16). The distance d was fixed to 25 mm and the separation s was varied. The calculations are illustrated in Figure 3.17 for different frequencies. For this type of configuration there exist no available measurements. Again, it is observed that the coupling drops as a function of distance in a similar way for different frequencies. Moreover, it can be seen that coupling drops with a considerably faster rate in the case of the echelon configuration than in the E-plane orientation. This coupling behavior agrees with what it has already been observed in patch antennas, and is due to the fact that along the ground plane the E-plane radiation pattern of an aperture antenna exhibits a maximum, whereas the H-plane radiation pattern exhibits a null.

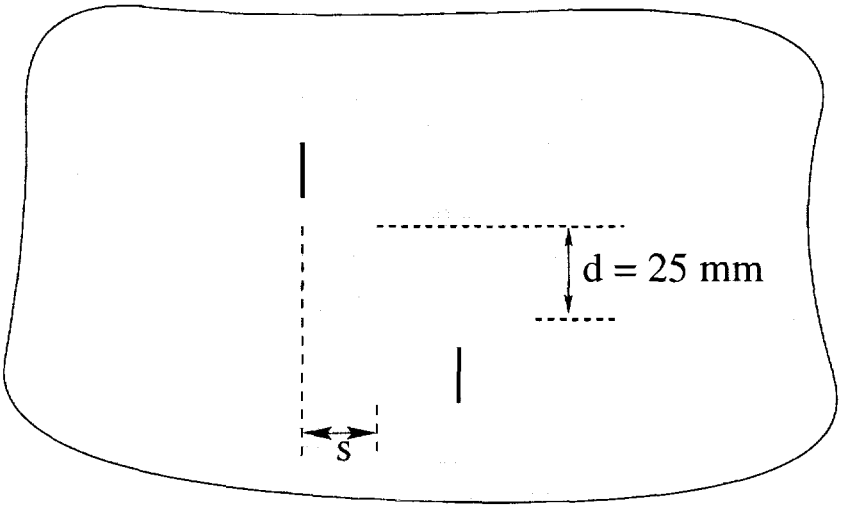

Figure 3.16: Top view of two identical cavity-backed slot antennas mounted on a ground plane (echelon configuration).

V. Conclusions

In this report an overview of the analysis of cavity-backed slot antennas in the context of FDTD and FEM/MoM was presented. Different numerical issues related to the modeling of such antennas were described. It was found that the use of a voltage source with an internal resistance in FDTD is indispensable for efficient computations. Both FDTD and FEM/MoM were used to compute the input impedance of a single CBS antenna, and coupling between two elements, and compared very well with

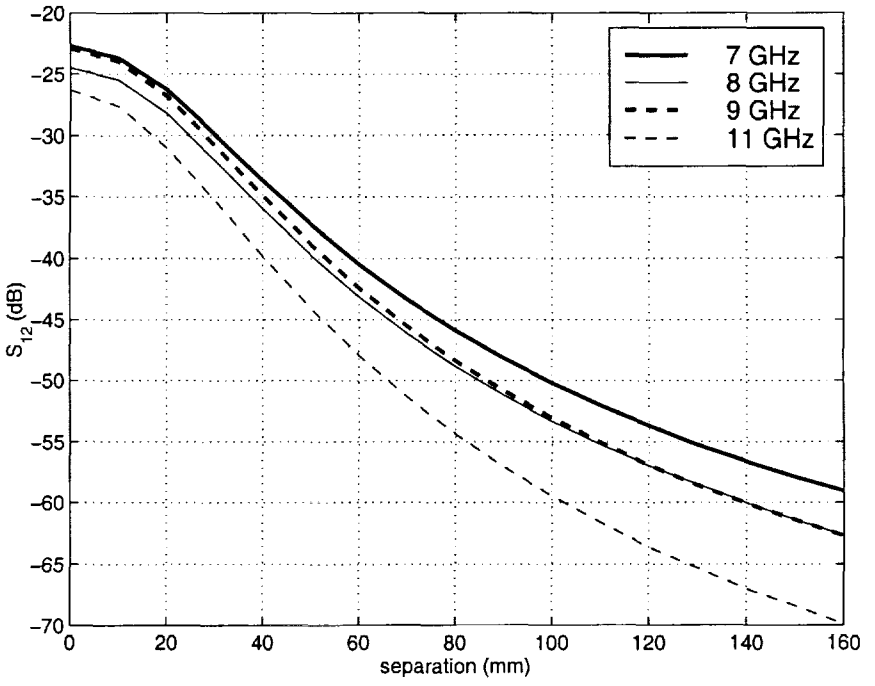

Figure 3.17: Coupling versus distance for the echelon configuration.

measurements. However, it was found that for coupling versus distance calculations, FEM/MoM is faster and more accurate than FDTD. This is attributed to the fact that FEM/MoM does not discretize the space between the two cavities but rather treats the open-space interaction within the MoM formulation. Therefore, it does not suffer from dispersion errors like FDTD which simulates the open space in addition to the cavity space. Also, the FEM/MoM computational space remains constant because only the CBS antennas need to be discretized in the hybrid methodology. On the contrary, FDTD has to also account for the space between the two antennas thereby yielding very large domains especially for large distances. Another advantage of the FEM/MoM approach is that it is more flexible in simulating arbitrary geometries without having the staircasing problem of FDTD. For example, coupling between arbitrarily oriented CBS antennas on a ground plane can be accurately computed using the existing FEM/MoM code, whereas the FDTD code would have to be modified to include contour-path methods in order to eliminate the staircasing errors.

Chapter 4

Radiation Pattern Analysis: FDTD(2,2) versus FDTD(2,4)

I. Introduction

In our research lab, higher-order FDTD schemes were developed in the past and thoroughly investigated. Specifically, a second-order accurate in time and fourth-order in space FDTD scheme [FDTD(2,4)] was first examined. The characteristics of FDTD(2,4) were compared with the ones of the standard second-order in time and space FDTD [FDTD(2,2)]. It was shown that FDTD(2,4) exhibits significantly smaller dispersion than FDTD(2,2). Therefore, it is expected that FDTD(2,4) can handle electrically large domains more efficiently and accurately. However, there are some problems related to the behavior of FDTD(2,4) around discontinuities especially PEC ones. Some of these issues were examined in the previous report by analyzing 1-D domains and some ways to resolve them were presented. As far as truncation methods, the anisotropic PML technique was used to terminate FDTD(2,2) and FDTD(2,4) lattices. It was found that PML is a very effective truncation technique, and it performs equivalently on either FDTD(2,2) or FDTD(2,4) computational grids.

After validating the FDTD(2,4) 3-D code along with PML, a more general FDTD(2,4) code was implemented. This code works in a similar way as the NEWS FDTD(2,2) code. Before the simulation starts, it reads a discretized geometry created by the Anastasia mesher and also an input file where all the problem parameters are specified. This FDTD(2,4) code can handle any type of radiation problems like the NEWS FDTD(2,2) code. However, scattering simulation capability has not been imple-

mented yet. It should be emphasized that this is the first version of a 3-D FDTD(2,4) code, and therefore, this program is still under validation. This validation procedure consisted of different radiation problems, e.g., analysis of dipoles, monopoles, cavity-backed slot antennas, etc., where patterns, coupling and input impedances have been calculated.

In this report, a few radiation problems are examined in order to investigate and illustrate possible advantages of FDTD(2,4) versus FDTD(2,2). Initially, the radiation patterns of a monopole antenna mounted on the tail of the NASA scale model helicopter are computed at 9.18 GHz. Moreover, the radiation patterns of a monopole antenna mounted on top of a rectangular box are calculated at 2 GHz. Both problems are analyzed using either FDTD(2,4) or FDTD(2,2) and the numerical results are compared with measurements.

II. Numerical Analysis

The first problem consists of a quarter-wavelength monopole at 9.18 GHz, mounted on the tail of the NASA scale-model helicopter. The geometry is shown in Figure 4.1. The principal radiation patterns of this monopole on the NASA helicopter were measured in the Electromagnetic Anechoic Chamber facility at Arizona State University in the past. The physical length of the monopole was 8.17 mm ($\lambda/4$ at 9.18 GHz), the cell size was 4 mm ($\lambda/8$) and the computational domain was $184 \times 440 \times 98$ cells or $21\lambda \times 51\lambda \times 11\lambda$ long. Both FDTD(2,2) and FDTD(2,4) were used to compute the principal plane patterns of the monopole. The numerical calculations are illustrated in Figs. 4.2-4.4, where the predicted yaw, roll, and pitch plane patterns are compared with measurements. Considering these computations, it seems that FDTD(2,4) does not provide a significantly better accuracy than FDTD(2,2). The main reason for this is that the discretization errors of each method are mixed with staircasing errors. The artificial corners that have been created on the simulation geometry through staircasing become diffraction points that affect substantially the shape of the radiation patterns. This effect becomes more dominant at high frequencies, as the one used in this simulation. Through a closer examination of the results, it seems though that FDTD(2,4) exhibits a slightly better accuracy than FDTD(2,2). This improved accuracy of FDTD(2,4) can be observed, for example, on the yaw pattern calculations,

and on the top, bottom and port side of the roll plane.

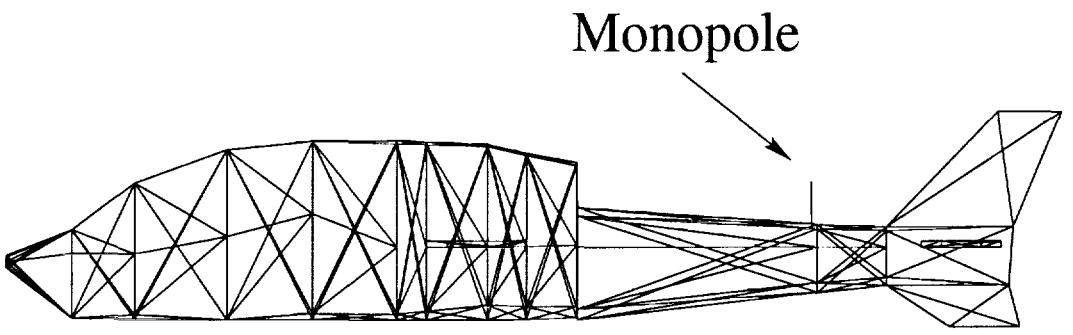

Figure 4.1: Geometry of a monopole mounted on the tail of the NASA scale-model helicopter.

Because of the coexistence of discretization and staircasing errors in the previous example, it was not clear which method is more accurate. Therefore, another problem, which is free of staircasing errors, was chosen to be analyzed. This problem consists of a monopole mounted on a rectangular box of dimensions $11\lambda \times 5\lambda \times 2\lambda$ at 2 GHz (see Figure 4.5). The physical length of the monopole was 60 mm ($\lambda/2.5$), the cell size was chosen either 20 mm ($\lambda/7.5$) or 5 mm ($\lambda/30$), and the computational domain was $92 \times 54 \times 34$ cells or $320 \times 168 \times 88$, respectively. Both FDTD(2,2) and FDTD(2,4) were used to compute the principal plane patterns of the monopole. The FDTD(2,2) code was run for both cell sizes (20 mm and 5 mm) whereas the FDTD(2,4) code was run only for the coarser mesh. The predictions of the simulation with the finer discretization (5 mm or $\lambda/30$) were used as a reference to determine the accuracy of all simulations performed with the coarser discretization (20 mm or $\lambda/7.5$). The results of FDTD(2,2) and FDTD(2,4) for the coarser mesh are compared in Figs. 4.6 and 4.7 with the FDTD(2,2) predictions obtained for the finer mesh. From these figures, it is obvious that even with such a coarse discretization of $\lambda/7.5$, FDTD(2,4) still predicted very accurately all principal patterns, whereas FDTD(2,2) failed to predict some of the peaks and nulls in these patterns. This example clearly illustrates that FDTD(2,4) outperforms FDTD(2,2) in terms of accuracy. Furthermore, it is expected that as frequency increases, the accuracy of FDTD(2,2) will decline even further whereas FDTD(2,4) will still provide satisfactory results. Additional simulations at higher

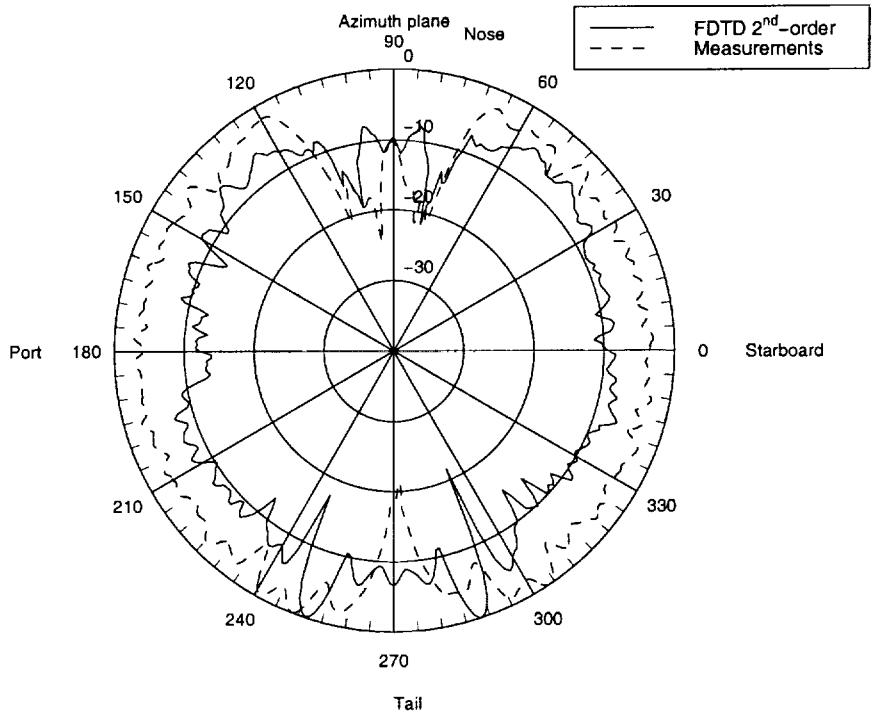

(a)

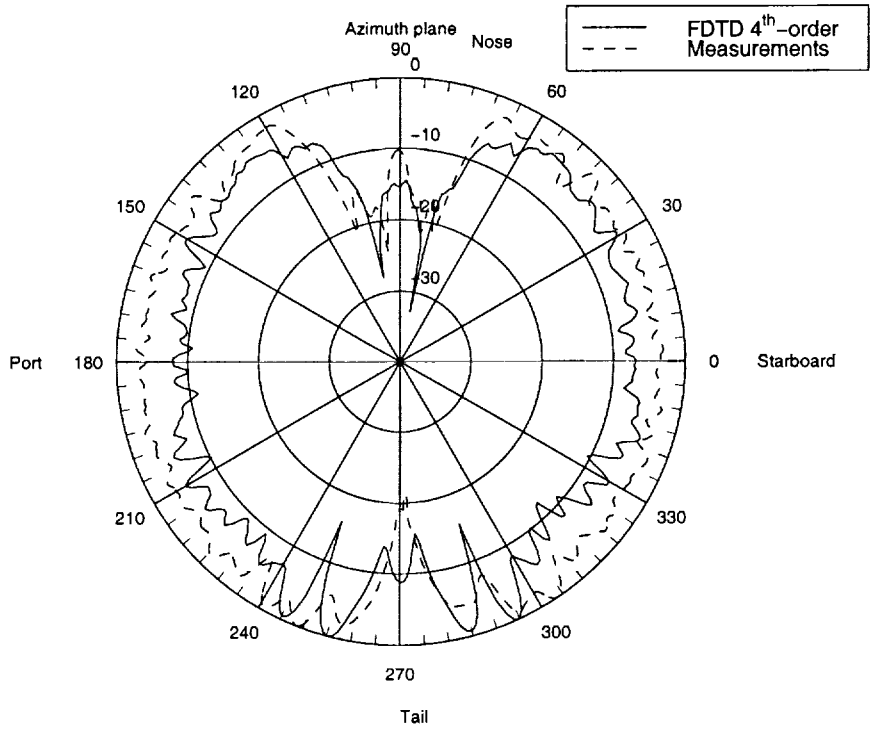

(b)

Figure 4.2: Yaw plane radiation patterns of a monopole mounted on the tail of the NASA scale-model helicopter at 9.18 GHz.

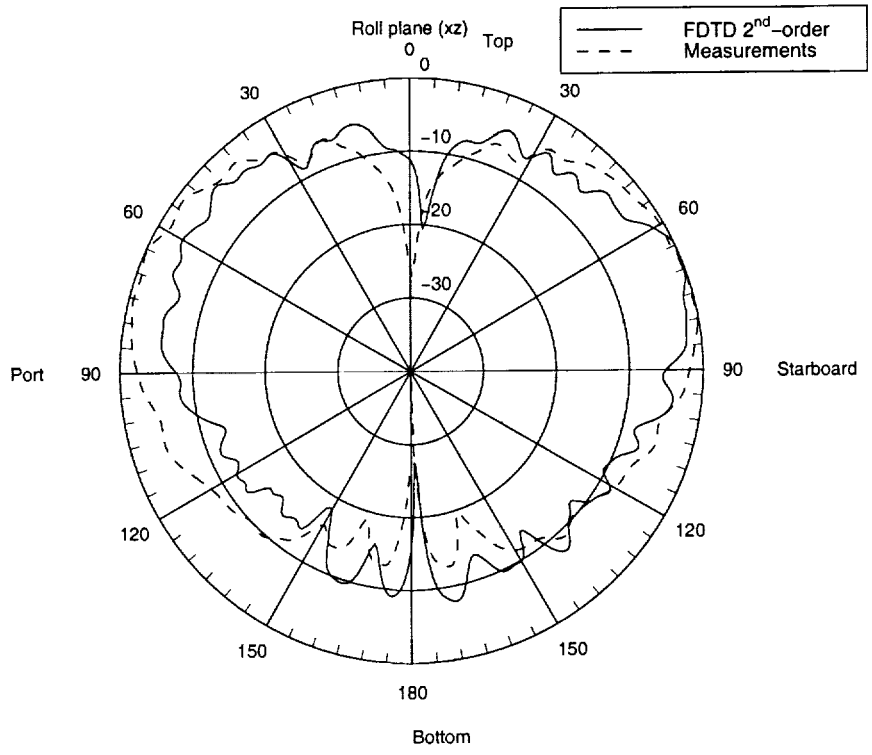

(a)

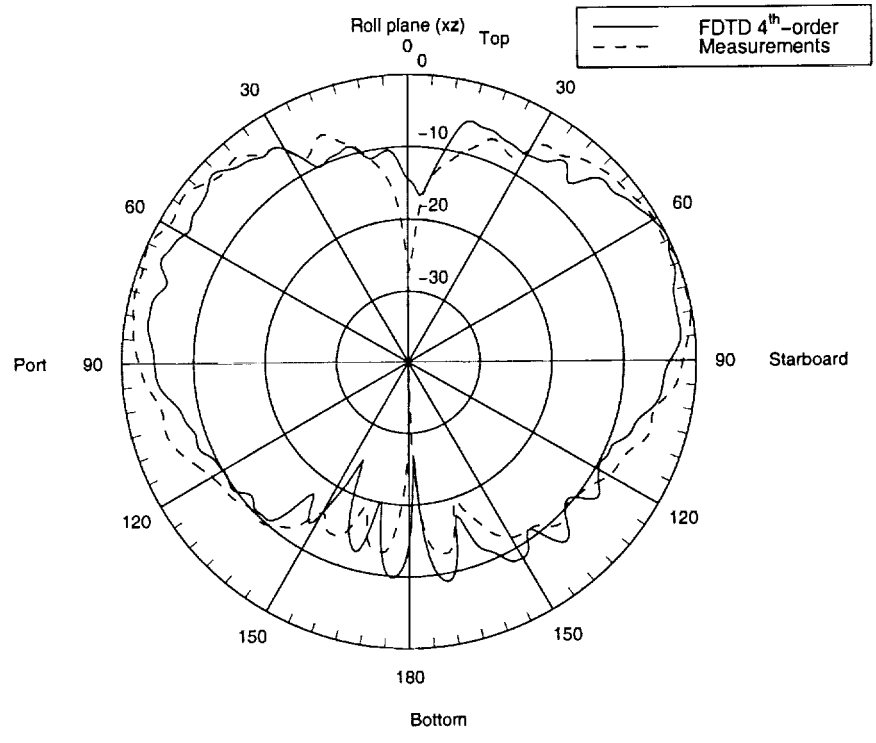

(b)

Figure 4.3: Roll plane radiation patterns of a monopole mounted on the tail of the NASA scale-model helicopter at 9.18 GHz.

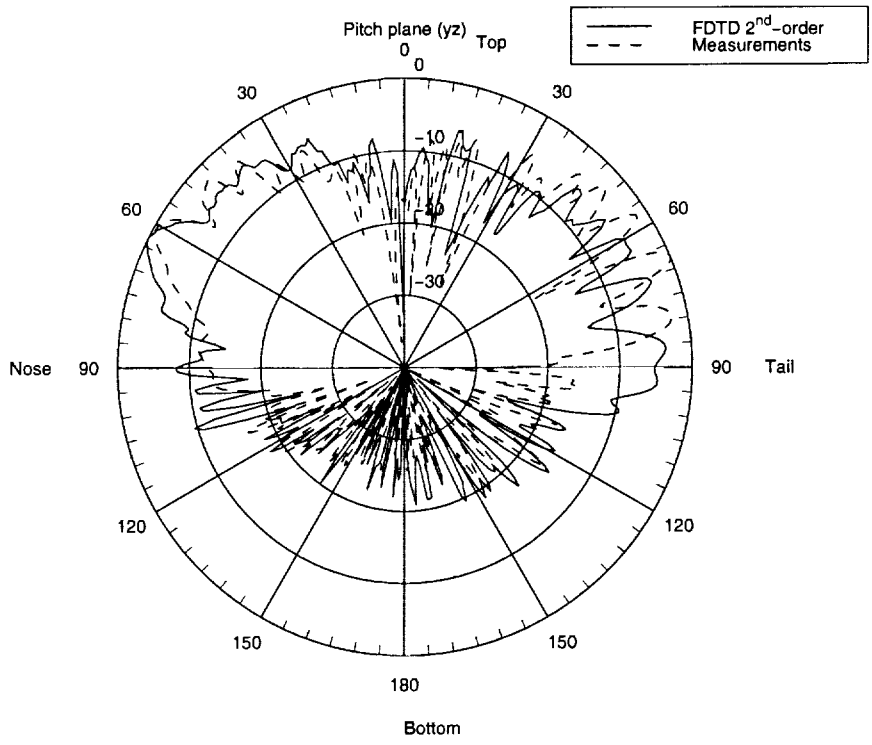

(a)

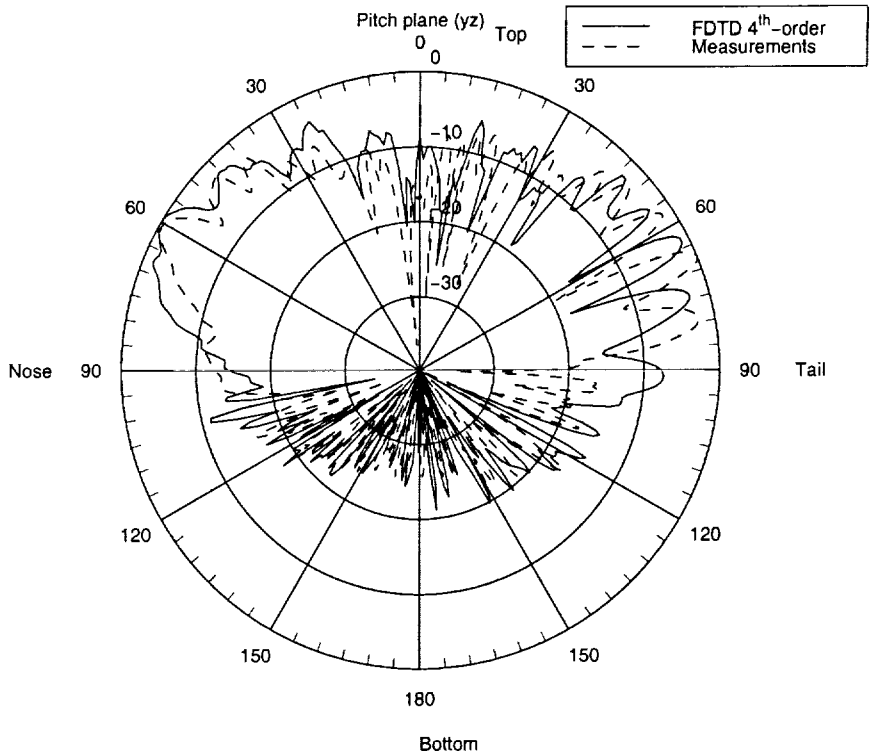

(b)

Figure 4.4: Pitch plane radiation patterns of a monopole mounted on the tail of the NASA scale-model helicopter at 9.18 GHz.

frequencies were not performed as it was impossible to run a fine enough mesh such as $\lambda/30$ at a frequency higher than 2 GHz with the available computational resources.

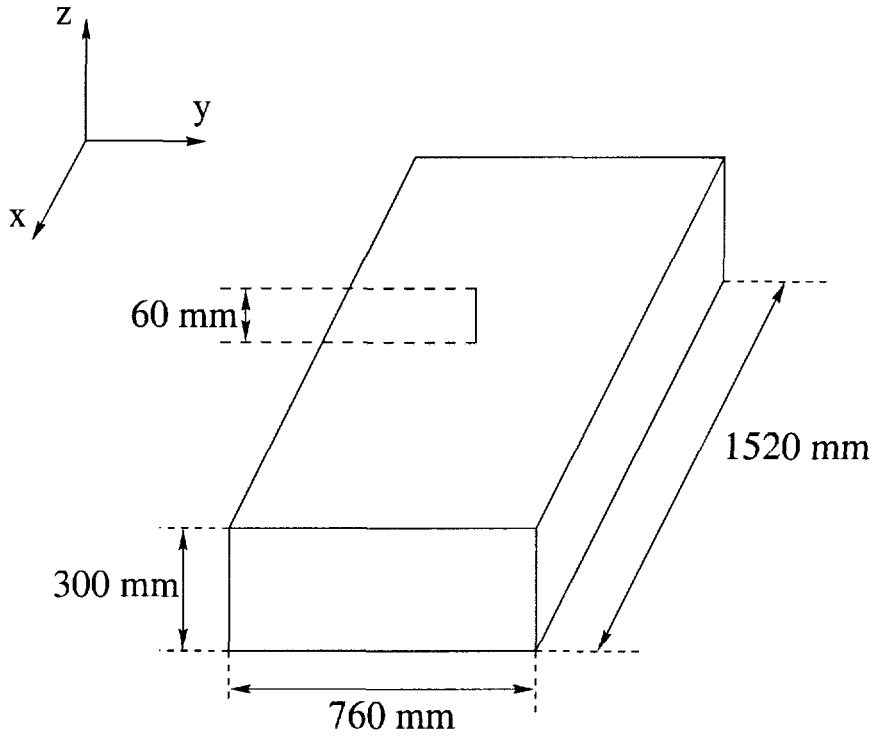

Figure 4.5: Geometry of a monopole mounted on a rectangular box.

III. Conclusions

Radiation patterns of monopoles on helicopters and rectangular boxes were computed using FDTD(2,2) and FDTD(2,4). It was shown that FDTD(2,4) outperforms FDTD(2,2) in terms of accuracy and overall computational efficiency.

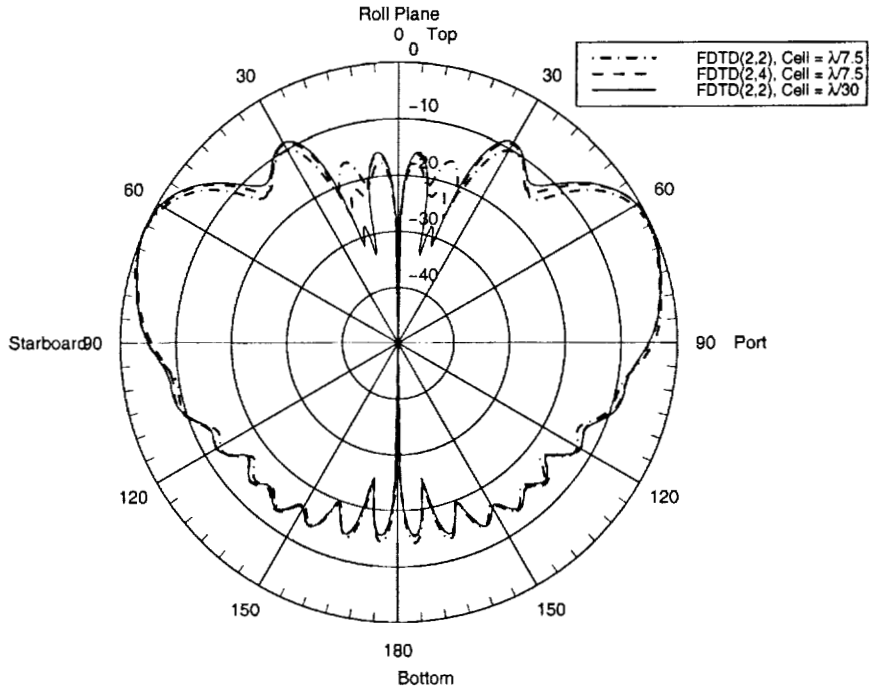

Figure 4.6: Roll plane radiation patterns of a monopole mounted on a rectangular box at 2 GHz.

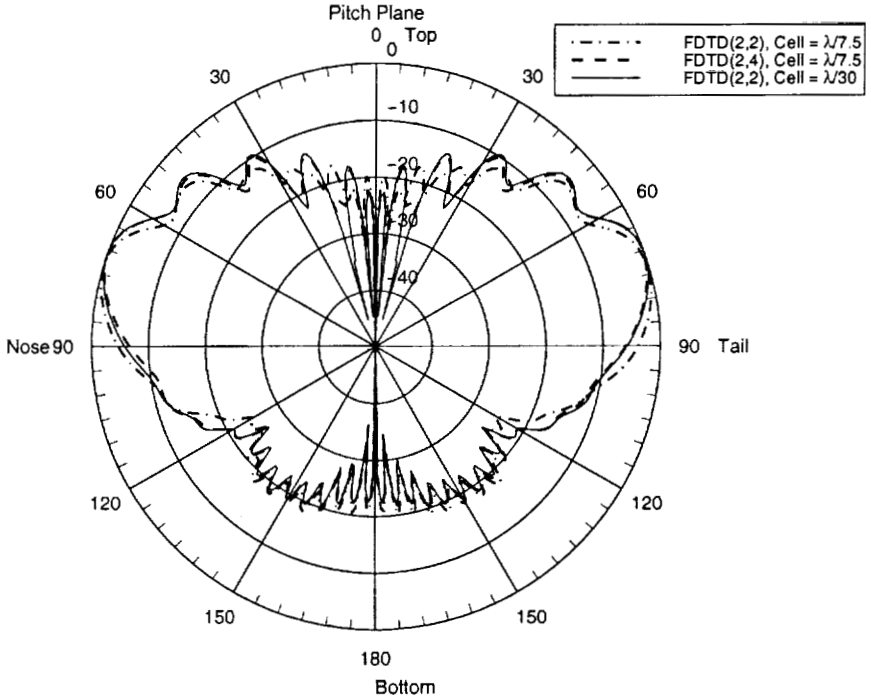

Figure 4.7: Pitch plane radiation patterns of a monopole mounted on a rectangular box at 2 GHz.

Chapter 5

A New Iterative Hybrid Method

I. Introduction

Analysis of slot antennas mounted on a flat conducting surface was performed in the past using a hybrid finite element/moment method (FE/MM) approach which is also referred to as the finite element/boundary integral (FE/BI) method. According to the FE/MM hybridization, the interior of the cavity is discretized using finite elements (tetrahedrons, prisms, bricks, etc.) whereas the exterior region is treated using a spectral or spatial domain moment method. As a result, the overall system matrix consists of the finite element matrix [A], which is highly sparse, and the admittance matrix [Y], which is dense; the two matrices are coupled through the unknowns in the aperture.

For the analysis of a single cavity-backed slot antenna, it was shown in previous reports that the hybrid FE/MM approach has enormous advantages over the pure FE or FDTD methods. The reason for that is because both the FE and FDTD methods require discretization not only in the interior of the cavity but also in the exterior region. The discretization in the exterior region needs to be fine enough so that the absorbing boundary conditions (ABC's), which are placed at some distance away from the slot, are accurate. This excessive discretization may become computational expensive, both in terms of CPU time and memory storage, since the number of unknowns could increase substantially. This computational load becomes even larger when coupling between two or multiple antennas needs to be computed. In such case, not only the interior of all slot antennas has to be discretized but also the free space surrounding them. Computer simulation of such a problem becomes almost

impossible using a pure FE or FDTD method. Even for the hybrid FE/MM approach, the computational burden becomes increasingly larger as the number of slot antennas increases.

In this chapter, a *new iterative hybrid* FE/MM approach is proposed to compute efficiently and fast coupling among multiple cavity-backed slots that are placed arbitrarily with respect to each other and flushmounted on a flat conducting surface. Electromagnetic coupling among these antennas is computed through an iteration algorithm. For simplicity, assume that there exist two cavity-backed slots spaced a given distance apart. For coupling computations, one antenna is excited with a constant voltage V_o whereas the other one is left open circuit. The new algorithm is as follows: at the first iteration, the antenna that is excited radiates in space in the absence of the second antenna. The radiated field induces a field in the aperture of the second antenna which propagates through its cavity. The second antenna, in turn, scatters the incident field in all directions thus affecting the field distribution in the aperture of the radiating slot. This perturbation in the field of the radiating element also changes the input impedance. The new field distribution is re-radiated toward the second antenna and the iteration process continues until convergence of the field in the two apertures is achieved. Once we reach convergence, the self and mutual impedances can be computed.

The new algorithm becomes extremely advantageous when the two antenna configurations are identical; thus, reducing (as it will be discussed later in this chapter) memory requirements and CPU time. It also provides a mechanism to achieve a full hybridization of FE/MM with other numerical techniques such as the GTD, PO, or even FDTD. In this chapter, we will present the formulation of this iterative method and apply it to the problem of computing coupling parameters of two identical cavity-backed slots flushmounted on an infinite conducting ground plane. The results obtained using the proposed iterative method will be compared with results obtained using the direct FE/MM approach. A comparison of CPU times and memory storage will also be provided.

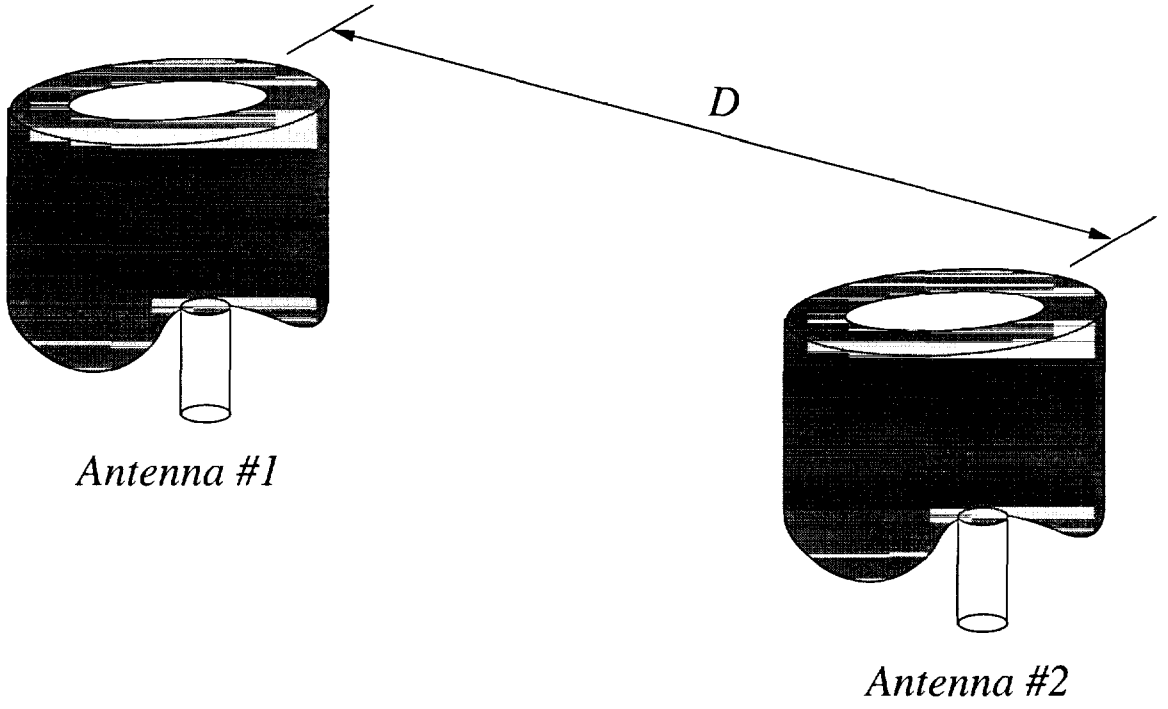

Figure 5.1: Geometry of two identical cavity-backed slot antennas mounted on an infinite ground plane.

II. Formulation

The problem under investigation is coupling among multiple cavity-backed slot antennas flushmounted on a conducting ground plane. For simplicity, we will first formulate the problem of coupling between two cavity-backed slot antennas similar to the ones shown in Figure 5.1. In order to compute the coupling parameters for such a configuration, one antenna is usually excited at the input terminal using a constant current I_1 whereas the input terminal of the second antenna is left as an open circuit. Radiation by the first antenna induces a voltage V_2 at the input terminal of the second antenna. Thus, the mutual impedance Z_{21} can be calculated using

$$Z_{21} = \frac{V_2}{I_1} \tag{5.1}$$

Similarly, the self impedance Z_{11} is equal to

$$Z_{11} = \frac{V_1}{I_1} \tag{5.2}$$

Due to reciprocity, $Z_{12} = Z_{21}$ and $Z_{22} = Z_{11}$. Knowing the complete set of Z-parameters, the corresponding S-parameters can be computed in a straightforward manner using standard transformation formulas found in microwave books.

Using the hybrid FE/MM approach to solve this coupling problem, the interior of the two cavities, including the apertures, is discretized using tetrahedral elements. The free space in between the two slots will not be discretized but rather the interaction between the two slots is taken into account through an integral formulation using the respective half-space Green's function. This approach certainly provides an advantage over the FDTD and pure FE methods since they both require a brute force discretization in free space. By renumbering the unknowns inside the finite element volume so that the unknowns in the aperture appear first whereas the unknowns inside the cavity appear last, the corresponding matrix system for a single radiating antenna is given by

$$\begin{bmatrix} M^{a/a} & M^{a/c} \\ M^{c/a} & M^{c/c} \end{bmatrix} \begin{bmatrix} E^a \\ E^c \end{bmatrix} = \begin{bmatrix} 0 \\ b^c \end{bmatrix} \tag{5.3}$$

where the superscript a stands for aperture and c for cavity. The non-zero excitation vector b^c is part of the finite element volume inside the cavity. In addition, the matrix $M^{a/a}$ is a pure method of moments matrix and is dense; $M^{c/c}$ is a pure finite element matrix and is highly sparse; the other two matrices $M^{a/c}$ and $M^{c/a}$ provide coupling between the field inside the cavity and the field in the aperture. Now, in case there are two cavity-backed slots in close proximity, the combined matrix system, after renumbering the unknowns, is given by

$$\begin{bmatrix} M_1^{a/a} & M_1^{a/c} & T_{12}^{a/a} & 0 \\ M_1^{c/a} & M_1^{c/c} & 0 & 0 \\ T_{21}^{a/a} & 0 & M_2^{a/a} & M_2^{a/c} \\ 0 & 0 & M_2^{c/a} & M_2^{c/c} \end{bmatrix} \begin{bmatrix} E_1^a \\ E_1^c \\ E_2^a \\ E_2^c \end{bmatrix} = \begin{bmatrix} 0 \\ b_1^c \\ 0 \\ 0 \end{bmatrix} \tag{5.4}$$

The subscript 1 denotes *antenna #1* and 2 denotes *antenna #2*. Note that for coupling calculations, when *antenna #1* is excited, *antenna #2* is left open circuit and vice versa. Thus, the right-hand side vector of the matrix system for *antenna #2* is

zero. The above matrix system can be written in a more compact and convenient form as follows:

$$\begin{bmatrix} M_1 & T_{12} \\ T_{21} & M_2 \end{bmatrix} \begin{bmatrix} E_1 \\ E_2 \end{bmatrix} = \begin{bmatrix} b_1 \\ 0 \end{bmatrix} \tag{5.5}$$

Matrix M_1 is the self matrix of *antenna #1*, M_2 is the self matrix of *antenna #2*, T_{12} and T_{21} are the interaction matrices between slots 1 and 2, and b_1 is the right-hand side vector corresponding to the excitation of *antenna #1*. It is important to mention here that the matrices T_{12} and T_{21} are transpose of each other, thus only one of them is stored in memory. In case the two cavities/slots are identical, and therefor their mesh information must be identical, these two matrices are symmetric which means only half of the matrix entries need to be saved.

As seen from the matrix system in (5.5), the electric fields E_1 and E_2 are coupled only through the dense interaction matrices T_{12} and T_{21}. If those interaction matrices were to be zero, matrices M_1 and M_2 would be completely decoupled, therefore, allowing us to solve for E_1 and E_2 independently and more efficiently. However, since these matrices are not zero, we need to take into account the interaction between the two slots and the governing fields.

The matrix system in (5.5) can be efficiently solved through an iteration algorithm. The iteration starts by setting the field E_2 to zero. This implies that *antenna #1* radiates in space as if *antenna #2* was not present. In other words, for iteration $k = 0$

$$E_2^{(0)} = 0 \tag{5.6}$$

and, therefore, we can write that

$$M_1 \cdot E_1^{(0)} + T_{12} \cdot E_2^{(0)} = b_1 \tag{5.7}$$

$$M_1 \cdot E_1^{(0)} = b_1 - T_{12} \cdot E_2^{(0)} \tag{5.8}$$

$$M_1 \cdot E_1^{(0)} = b_1 - 0 \tag{5.9}$$

where the superscript (0) indicates iteration $k = 0$. Thus, after the matrix system in (5.9) is solved, we can obtained $E_1^{(0)}$ which simply represents the governing field

distribution of *antenna #1* in the absence of *antenna #2*. Then, from (5.5) we can write that

$$M_2 \cdot E_2^{(1)} = 0 - T_{21} \cdot E_1^{(0)} \tag{5.10}$$

where the product of $T_{21} \cdot E_1^{(0)}$ requires $N_1^a \times N_2^a$ operations; N_1^a is the number of unknowns in the aperture of *antenna #1* and N_2^a is the number of unknowns in the aperture of *antenna #2*. Once the value of E_2 is updated, the iteration algorithm may continue on by updating E_1 using

$$M_1 \cdot E_1^{(1)} = b_1 - T_{12} \cdot E_2^{(1)} \tag{5.11}$$

The updating of the vectors E_1 and E_2 will continue until an acceptable convergence tolerance is obtained. A measure of convergence can be defined based on the 2-norm residual given by

$$\rho_1 = \|E_1^{(k)} - E_1^{(k-1)}\|_2 \tag{5.12}$$

$$\rho_2 = \|E_2^{(k)} - E_2^{(k-1)}\|_2 \tag{5.13}$$

When both ρ_1 and ρ_2 are less than a given tolerance, it means that convergence has been achieved.

This hybrid method, which takes into account coupling between antennas through an iterative algorithm, is extremely advantageous when it is necessary to compute the coupling parameters of two identical antennas as a function of distance. For two identical cavity-backed slot antennas, only one geometry needs to be discretized since $M_1 = M_2 = M$. Also, $T_{12} = T_{21} = T$ which, in this case, is a square symmetric matrix. Thus, when coupling versus distance is calculated, the system matrix M does not change as a function of distance; the only matrix that changes versus distance is the interaction matrix T, which is relatively small ($N_a \times N_a$) and calculated using a spatial or spectral domain method of moments. As a result of this observation, the matrix M needs to be inverted only once, possibly using a sparse LU decomposition, whereas the updating of the fields E_1 and E_2 is done relatively fast using a simple backward substitution. Even when the relative distance between the two antennas is changing, the matrix M does not need to be inverted again. Consequently, the coupling parameters as a function of distance may be computed with only minimum

computational effort which corresponds to the CPU time needed by the sparse LU algorithm to invert the matrix M. In addition, the memory requirements for storing the system matrix are reduced considerably, compared to a brute force discretization of the original two-antenna configuration. Memory savings also occur in storing other finite element arrays such as the connectivity information, nodal coordinates, edges, etc.

More pronounced improvements in terms of CPU time and memory storage can be observed when the number of antennas is increased to three. In such a case, the self matrix M is identical for all radiating elements and, thus, it needs to be inverted only once for coupling versus distance calculations. In contrast, the number of interaction matrices increases from one to a total of three; i.e., $T_{12} = T_{21}$, $T_{13} = T_{31}$, and $T_{23} = T_{32}$. Filling though these matrices as a function of distance is not computationally expensive, especially when using a spatial domain method of moments.

III. Results

In the previous section, the idea of field interaction between two distant radiating elements through a novel iterative hybrid approach has been introduced and formulated for a generic problem. Each of the radiating objects is treated separately using the method of choice, whereas the coupling between the two objects is taken into account at subsequent iterations to correct the field distribution obtained from a previous iteration step. This approach is innovating and potentially powerful because it allows field interaction not only between two FEM domains, or an FEM and a MM domain, but also between FEM and GTD or FEM and PO.

Since this is the first time that this iterative approach is presented to the AHE program, it will be initially applied to the problem of coupling between two cavity-backed slot antennas mounted on an infinite ground plane, as is shown in Figure 5.2. The two cavity-backed slots are placed a distance D apart whereas the transverse dimensions of each slot correspond to those of an X-band waveguide. The depth of the cavity is 7.7559 cm and the probe is located in the center of the horizontal dimension at a distance of 1.905 cm from the bottom face. The length of the probe is 0.6985 cm.

The most obvious approach to solve for the coupling parameters of the two slots is

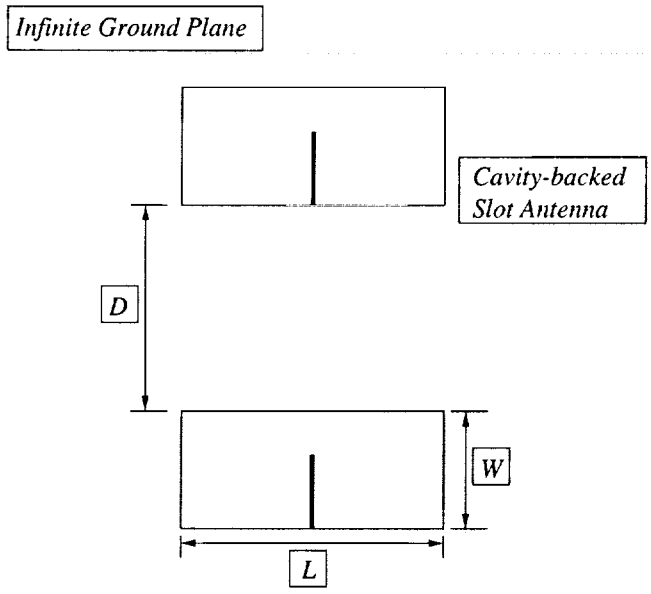

Figure 5.2: E-plane configuration of two identical cavity-backed slot antennas mounted on an infinite ground plane ($L = 2.286$ cm, $W = 1.016$ cm).

to perform a brute-force discretization in both cavities and apply the hybrid FE/MM approach. The interaction between the two slots is implicitly taken into account in the formulation. This approach has the disadvantage of creating twice as many unknowns, compared to the proposed iterative method, therefore requiring excessive memory storage and a long CPU time to solve the final matrix system. Besides, the matrix system needs to be re-solved every time the separation distance D between the slots is changed. In contrast, using the iterative approach, only one cavity needs to be discretized, thus saving memory storage and generating a smaller matrix system, which can be solved faster and more efficiently. Also, every time the separation distance is changed, the new field distribution can be conveniently computed using a simple back-substitution since the original self matrix is not a function of separation distance. This back-substitution can be performed provided the sparse LU or ILU factorization of the original matrix was obtained at the first iteration step. More substantial computational savings, both in terms of memory and CPU time, can be obtained when coupling among a larger number of identical cavity-backed slot antennas is computed.

Using the iterative approach to calculate coupling, the two antennas are basically

treated separately whereas the field interaction between the slots is accounted for through an iteration procedure. It is not clear, however, how many iterations it takes for the field distribution in the two domains to actually converge. The first experiment performed in this study was to calculate the real and imaginary parts of the self and mutual impedances as a function of iteration number k at a frequency of 8 GHz and a separation distance of 1 cm along the E-plane. These results are illustrated in Figs. 5.3 and 5.4. For the sake of clarity, $k = 0$ indicates that the self impedance of antenna 1 was calculated assuming antenna 2 was not present. For $k = 1$, the field radiated by antenna 1 induced a field distribution on antenna 2 which was then scattered and altered the field distribution of antenna 1. This iteration procedure continues for a higher values of k. In both these figures, it is clear that the self and mutual impedances converge to a value at $k = 3$. For $k = 0$, which basically means that there is no interaction between the two antennas, the real part of the self impedance was found to be 37 ohms whereas the imaginary part was -86.15 ohms; the converged values, however, at $k = 3$ are 41.3 and -85.4 ohms, respectively. For a smaller separation distance D, these discrepancies between first and second iterations are even larger. Similar observations are made for the mutual impedance, too. For $k = 0$, the mutual impedance is absolute zero since the interaction has not yet been accounted for. As the iteration number increases, both real and imaginary parts of the mutual impedance converge to a constant value.

This iterative technique was applied on the same antenna configuration, however with slot separation $D = 2$ cm, to calculate the self and mutual impedances as a function of frequency. The self impedance as a function of frequency is shown in Figure 5.5. The results obtained using the iterative technique for $k = 5$ are compared with the FE/MM direct approach which was validated against measurements and presented in Chapter 3. As illustrated, the comparison between the two techniques is excellent; note that the iterative technique is computationally more efficient. The mutual impedance as a function of frequency is shown in Figure 5.6. The agreement between the two methods is fairly good although there are some discrepancies for frequencies close to the parallel resonance of the slot. The reason is related to the accuracy of computing the coupling matrix between the two slots. This matrix is similar to a transfer function; knowing the input, the accuracy of the output is

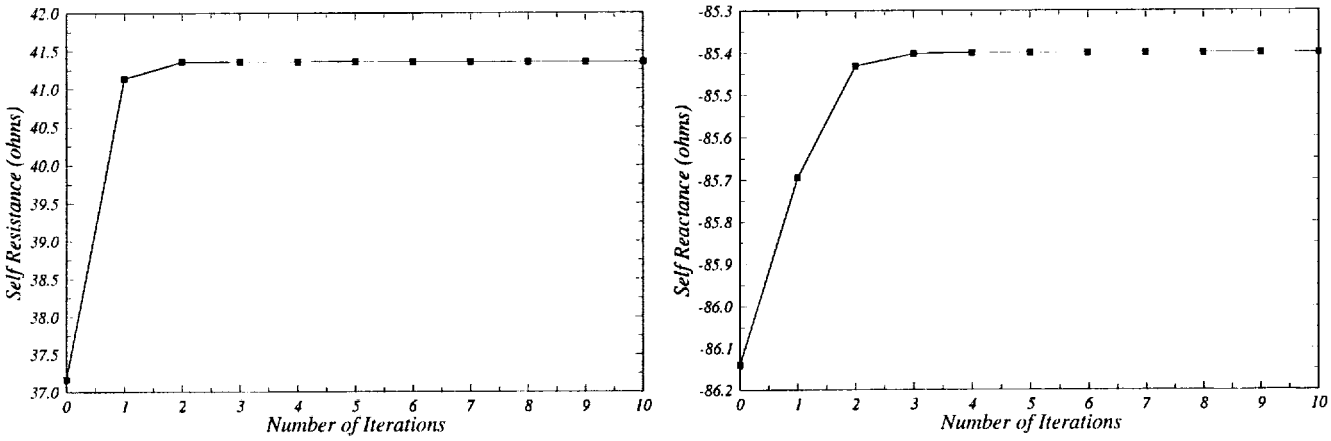

Figure 5.3: Real and imaginary parts of the self impedance as a function of iteration number. The two slots are placed in an E-plane configuration with separation distance of 1 cm. The frequency of operation is 8 GHz.

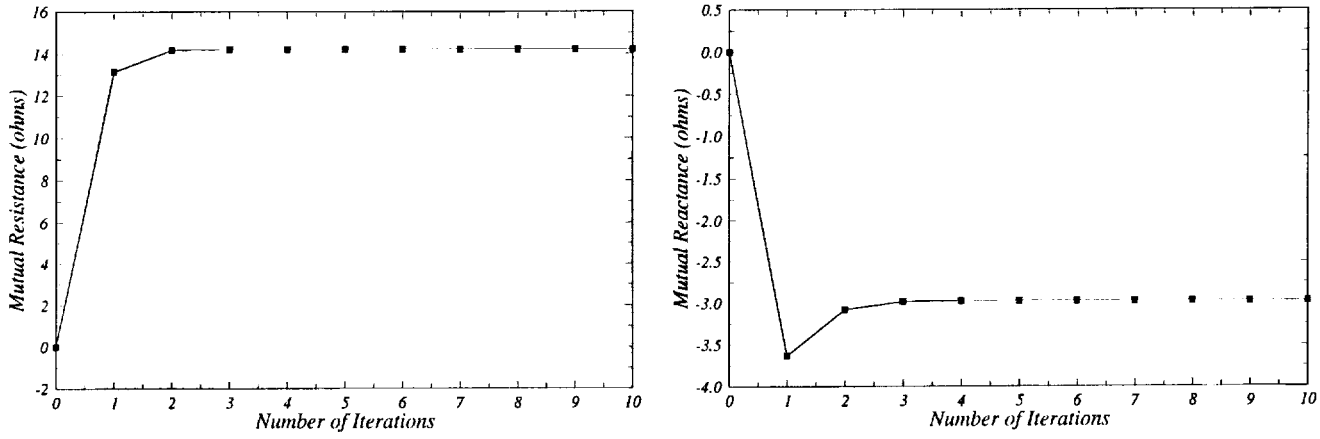

Figure 5.4: Real and imaginary parts of the mutual impedance as a function of iteration number. The two slots are placed in an E-plane configuration with separation distance of 1 cm. The frequency of operation is 8 GHz.

solely determined by the accuracy of the transfer function. This coupling matrix was computed using a spatial domain method of moments which involves integration over triangular surfaces. These integrals are evaluated using a 13-point Gauss quadrature which is not strictly accurate, especially for large separations. In order to more accurately compute the mutual impedance, the 13-point Gauss quadrature needs to be improved by a higher-order integration.

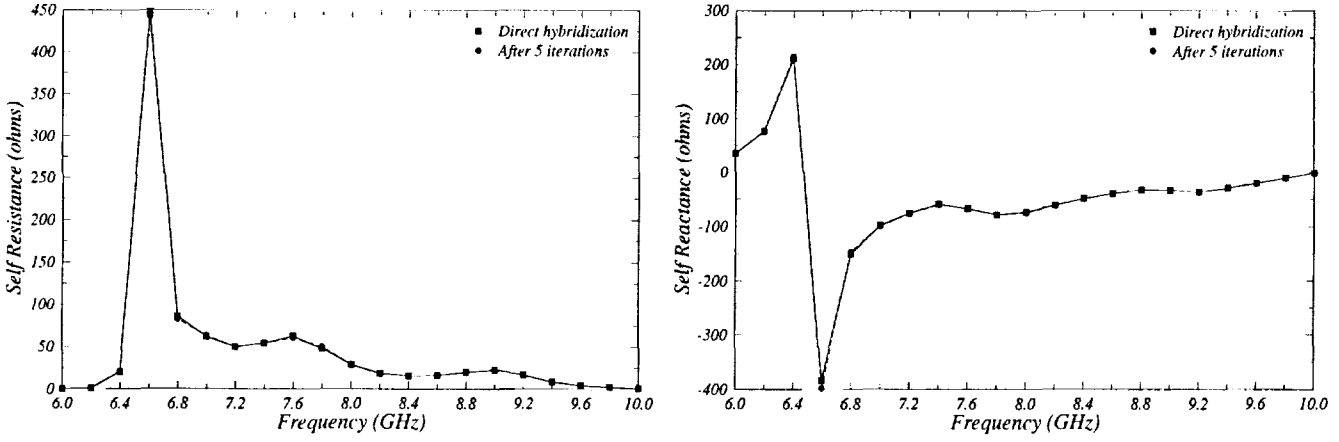

Figure 5.5: Real and imaginary parts of the self impedance as a function of frequency. The two slots are placed in an E-plane configuration with separation distance of 2 cm.

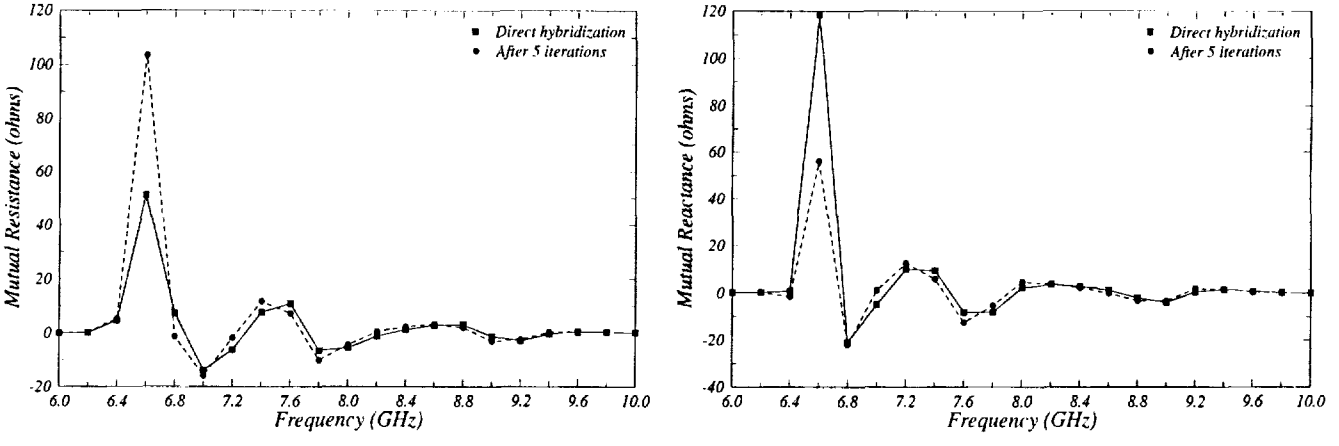

Figure 5.6: Real and imaginary parts of the mutual impedance as a function of frequency. The two slots are placed in an E-plane configuration with separation distance of 2 cm.

The return loss and mutual coupling as a function of frequency are depicted in

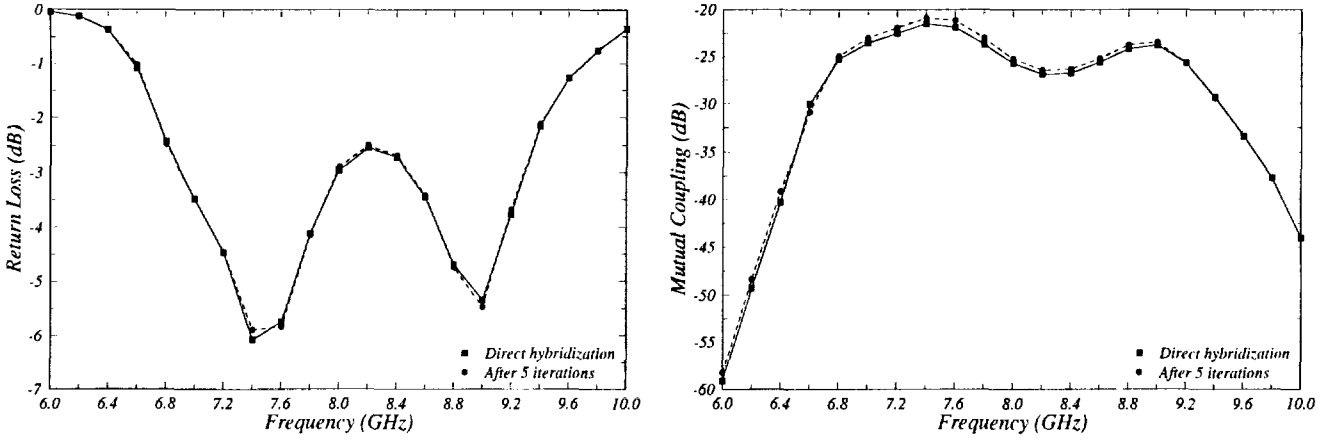

Figure 5.7: Return loss and mutual coupling as a function of frequency. The two slots are placed in an E-plane configuration with separation distance of 2 cm.

Figure 5.7 for a separation distance of 2 cm along the E-plane. The iteration technique is compared with the hybrid FE/MM direct approach which is considered accurate enough. As illustrated, the agreement between the two methods is excellent. Even with one iteration the mutual coupling as a function of frequency compares very well. However, since the computational effort required for subsequent iterations is minimal, we often choose to compute the coupling parameters after 5 iterations have past.

The most noticeable computational savings in terms of CPU time are realized when computing coupling parameters as a function of distance. The reason for achieving such computational speed-up is because the system matrix is factorized (either using LU or ILU) only once. As the separation distance is varied, the updated field distribution inside the cavities is computed by using only a simple back-substitution which involves order of N operations, where N is the number of unknowns for the self matrix. Simply stated, the self matrix M is not a function of the distance between the two slots.

The real and imaginary parts of the mutual impedance as a function of distance between the two slots are plotted in Figure 5.8. Three line traces are shown in each graph: one representing the direct approach and the other two representing the iterative approach. For the iterative approach, we chose to show the results for both "iteration 1" and "iteration 5" although there are no substantial discrepancies between the two traces. As those are compared with the direct approach, there exist

some small differences which are mostly attributed to the accuracy of the coupling matrix formulated through a spatial domain integral boundary equation.

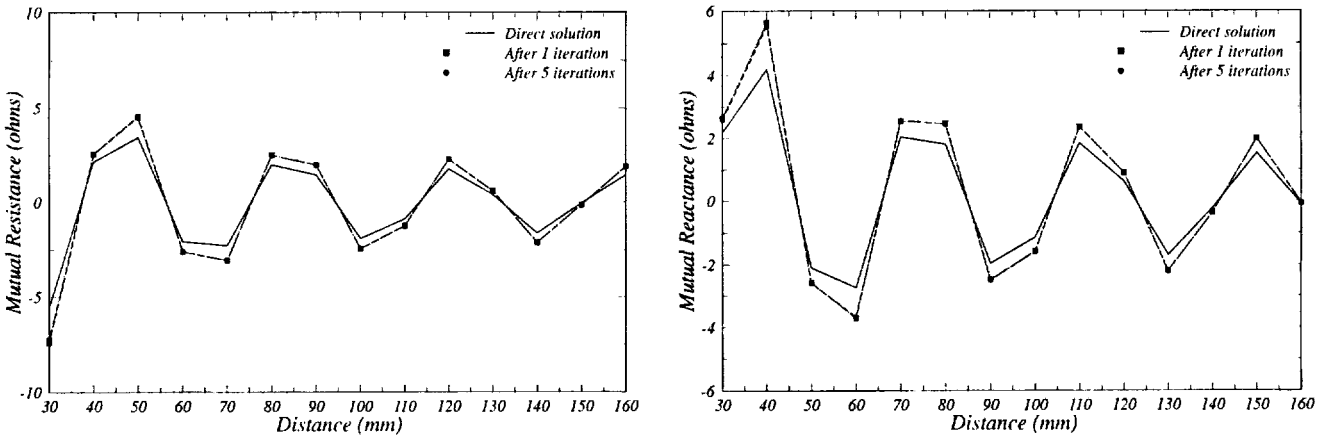

Figure 5.8: Real and imaginary parts of mutual impedance as a function of distance. The two slots are placed in an E-plane configuration and the frequency of operation is 8 GHz.

Although Figure 5.8 illustrates some minor discrepancies between the direct and iterative hybrid techniques, as those were used to compute the real and imaginary parts of the mutual impedance, their comparison for mutual coupling (S_{12}) as a function of distance is very good. The corresponding graph is shown in Figure 5.9 for a separation distance ranging between 30 and 160 mm. As illustrated, both methods give almost identical results. As far as the iterative technique is concerned, the difference in the predictions when using only 1 iteration versus when using 5 iterations is more noticeable for relatively small separation distances.

Before concluding this chapter, it is important that we discuss the computational requirements of the techniques used in this report to predict coupling of slot antennas. Basically, we have used two methods: a direct FE/MM hybridization and an iterative FE/MM hybridization. For the first method, the coupling mechanism between the two antennas is implicitly built into the matrix system, whereas for the second method, this coupling mechanism is explicitly taken into account through an iteration process. For the same discretization, the iterative method requires less than half the memory requirements compared to the direct method. Concerning computational time, it is good that we consider the case discussed in Figure 5.9. For this problem, the number of tetrahedrons used in the direct approach was 39,046 whereas the number

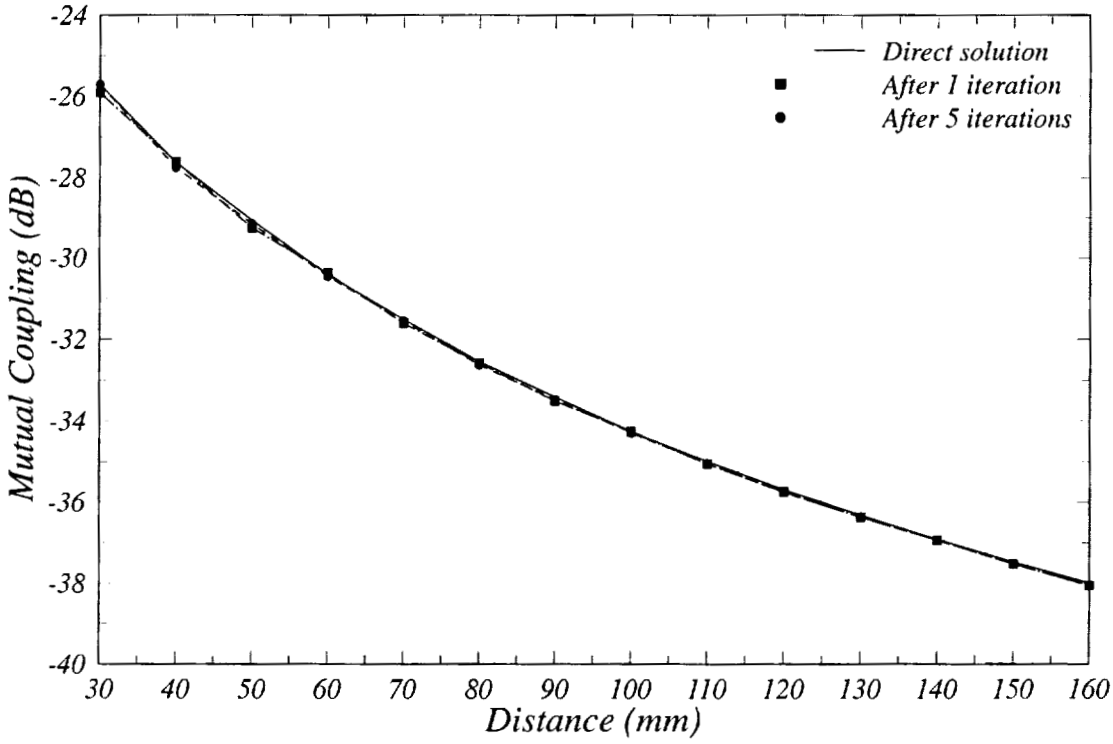

Figure 5.9: Mutual coupling as a function of distance. The two slots are placed in an E-plane configuration and the frequency of operation is 8 GHz.

of unknowns was 41,120. For the iterative approach and using the same element mesh size, the number of tetrahedrons used in the computational domain was 19,543 whereas the total number of unknowns was 20,583. Solving the matrix system for the FE/MM direct approach, a Conjugate Gradient Square (CGS) algorithm was used. The total CPU time spent to compute the mutual coupling between the two slots for a total of 14 points, as shown in Figure 5.9, was 288 minutes. For the FE/MM iterative approach, we had the choice of either using a sparse ILU decomposition to factor the matrix once and then use back-substitutions for the remaining iteration process, or using the CGS algorithm for all iterations. Both options were followed. When the sparse ILU decomposition was used, it took 134 minutes to obtain the matrix factorization; the remaining computations were performed within a very small time period (1-2 minutes, assuming 1 iteration per point). When the CGS was used, again assuming only 1 iteration per point, the total CPU time for 14 evaluation points was 83 minutes. However, as the number of iterations increases, the CPU time increases accordingly. For example, if 5 iterations are used, the total CPU time increases to 265 minutes.

As seen from these numbers, the FE/MM iterative approach results in both memory savings and CPU speed-up. Specifically, if our main objective is to compute mutual coupling versus distance for a large number of points, the iterative approach using ILU factorization first and then back-substitutions might be the most attractive choice. On the other hand, if the number of evaluation points is small, the iterative approach using CGS might be preferred.

IV. Conclusions

In this chapter, we introduced a novel hybrid iterative approach to efficiently calculate coupling between two or more cavity-backed slot antennas mounted on an infinite ground plane. Each cavity is independently analyzed using the hybrid FE/MM approach, whereas the field interaction between the antennas is taken into account through an iteration algorithm. This results in substantial computational savings both in terms of memory storage and CPU time. It was observed that this algorithm converges within only a few iterations. The results compare favorably with the hybrid FE/MM direct approach which has been used in the past to compute self and mutual

impedances of two cavity-backed slots.

Another advantage of this new iterative approach is the potential for further hybridization of finite element with other methods such as the geometrical theory of diffraction (GTD) and/or the physical optics (PO). Field interaction between an antenna and an electrically large object in close proximity can be accounted for through this iterative approach in order to compute the overall radiation pattern as well as the input impedance. Most hybrid techniques only consider one-way interaction between the antenna and the object. In other words, the scattered fields by the object are not allowed to change the field distribution of the antenna and, therefore, its input impedance is the same as that one in the absence of the object. Using this innovative iterative algorithm, a full interaction between the two objects is possible.

Chapter 6

Hybrid Techniques for Scattering and Radiation Problems

I. Introduction

Increasing the frequency of operation in helicopter communications provides a way of overcoming the limitations of line-of-sight communication. Satellite communication is an area from which modern helicopter technology is seeking for solutions to reach out over-the-horizon. In satellite communications usually higher than UHF frequencies are used, which results in the enormous size of computational domain. Therefore, it hinders use of a rigorous numerical method in the analysis of an antenna mounted on an airframe. As second choice, the adoption of hybrid techniques has been suggested.

In fact, the FEM and PO were hybridized to analyze a monopole antenna on the APACHE helicopter in the UHF band. Its predictions for simple structures were provided along with measurements and exact solutions to validate the code. At the same time, the limitation of the method was also revealed; mainly due to having no account for diffractions and higher order interactions. Instead of using PO, the use of PTD allows inclusion of the diffractions in the analysis. However, the PTD solution is available only for simple structure; therefore, the implementation of PTD for a helicopter structure may take considerable amount of effort. Therefore, main focus of this report is on investigating and taking into account the higher order interactions through a hybrid technique. Here, higher order interaction means only the interaction between the antenna and its lit zone on the airframe. The diffractions can also be thought of as higher order interactions, but these are not included yet.

In this report, to get a better insight of the problem, a 2D hybrid code was developed and used. As for the FEM analysis, more accurate boundary conditions than ABCs were implemented, referred to here as BIE (Boundary Integral Equation). Using both truncation schemes, the FEM is hybridized with the PO which corresponds to the first order interactions. The reformulation was needed to account for higher than the first order interactions. In order to take the higher order interaction systematically, an iterative algorithm is presented. It is also explained that the consideration for higher order interactions can be achieved using other than PO, e.g., GTD. The iterative algorithm shows that it allows the modification of equivalent currents at each iteration by having an updated right-hand side vector.

II. 2D Radiation and Scattering

The 2D-radiation problem can be decomposed into two decoupled TE_z and TM_z polarization analyses. For both cases, the scalar Helmholtz equation is given by

$$-\frac{\partial}{\partial x}(\alpha\frac{\partial\phi}{\partial x})+-\frac{\partial}{\partial\phi}(\alpha\frac{\partial\phi}{\partial y})+\beta\phi=f \tag{6.1}$$

where

$$\phi=E_z,\quad \alpha=\frac{1}{\mu_r},\quad \beta=-k_o^2\epsilon_r,\quad f=-jk_oZ_oJ_z \tag{6.2}$$

for E_z-polarization and

$$\phi=H_z,\quad \alpha=\frac{1}{\epsilon_r},\quad \beta=-k_o^2\mu_r,\quad f=\frac{\partial}{\partial x}(\frac{J_y}{\epsilon_r})-\frac{\partial}{\partial y}(\frac{J_x}{\epsilon_r}) \tag{6.3}$$

for H_z-polarization. The equation can be solved in conjunction with a boundary condition which can be derived from an ABCs or BIE [16]. For the finite element, triangular elements or quadrilateral elements are used to discretize the computational domain. If the triangular elements are used, a much larger number of unknowns will be generated compared to the quadrilateral elements. However, triangular elements do not require any computational effort to evaluate the integrals for the element matrix because all these integrals can be evaluated in an analytic way. In contrast, the quadrilateral elements lead to a smaller number of elements than the triangular elements, but the evaluation of the element matrix has to be performed in a numerical way. The truncation of the computational domain can be achieved by using ABCs.

The two ABCs implemented here are those of first (γ_1, q_1) and second order (γ_2, q_2)

$$\alpha\frac{\partial\phi}{\partial n}+\gamma_{(1,2)}\phi = q_{(1,2)} \tag{6.4}$$

$$\gamma_1 = \alpha[jk_\circ+\frac{1}{2\rho}] \tag{6.5}$$

$$\gamma_2 = \gamma_1+\alpha\left[\frac{-j}{8\rho^2(j/\rho-k_\circ)}-\frac{j}{2(j/\rho-k_\circ)}\frac{\partial^2}{\rho^2\partial\varphi^2}\right] \tag{6.6}$$

$$q_1 = \frac{\partial\phi^{inc}}{\partial n}+[jk_\circ+\frac{1}{2\rho}]\phi^{inc} \tag{6.7}$$

$$q_2 = q_1+\alpha\left[\frac{-j}{8\rho^2(j/\rho-k_\circ)}\right]\phi^{inc}-\frac{j\alpha}{2(j/\rho-k_\circ)}\frac{\partial^2\phi^{inc}}{\rho^2\partial\varphi^2} \tag{6.8}$$

This formulation is for the scattering problem; however, it can also be used for the radiation problem by setting ϕ^{inc} to zero. Based on this formulation, a 2D-FEM code was written. To validate the 2D-scattering code, scattering from a square cylinder was considered. The schematic of the problem is depicted in Figure 6.1. The FEM code does not have limitations in terms of coated materials on the scatterer, but a PEC square cylinder was chosen to compare with MOM solutions. Both triangular elements and quadrilateral finite elements were used in conjunction with the 2nd order ABCs. The mono-static echo width of a square cylinder predicted with the FEM is compared with the MOM results in Figure 6.2. The echo width can be computed from

$$\sigma(\varphi)=\lim_{\rho\to\infty}2\pi\rho\frac{|\phi^{sc}|^2}{|\phi^{inc}|^2} \tag{6.9}$$

Because of symmetry in the geometry, the echo width (σ) in other ranges is a repeating of Figure 6.2. As can be seen, the agreement between the FEM and MOM is very good, let alone the agreement between triangular and quadrilateral elements. The ABCs was applied at the distance of 0.35λ away from the scatterer. It will also be interesting to test the accuracy of the 1st and 2nd order ABCs because the shape of ABC surface is almost square. Figure 6.3 shows that both the 1st and 2nd order ABCs work well for this problem, though all coefficients of the ABCs are derived from an assumption that the ABCs surface is a circular cylinder.

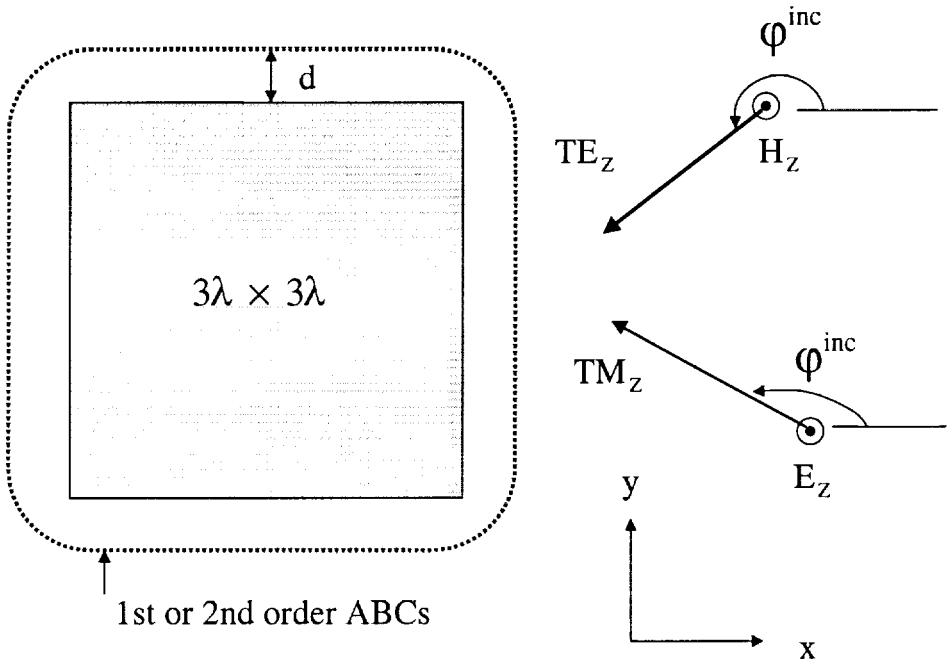

Figure 6.1: Scattering from a square cylinder when a plane wave is incident from an angle of ϕ^{inc} with respect to the x-axis.

III. Boundary Integral Formulation

When the FEM is used with ABCs to analyze an elongated geometry, there is always additional number of unknowns. However, the ABCs is a local boundary condition; therefore, the sparsity of the system matrix can be reserved. In other situation, such as two independent radiation systems are located close to each other, but it cannot be solved as one combined system, then ABCs may not be possible to apply because of the requirement of minimum distance. For this case, it is necessary to have a boundary condition that can be applied to the geometry as close as it can be. Having such a boundary condition, the overall radiation problem may be able to be represented through a coupling mechanism occurred between the two independent systems. Alternative boundary condition can be obtained from surface integral

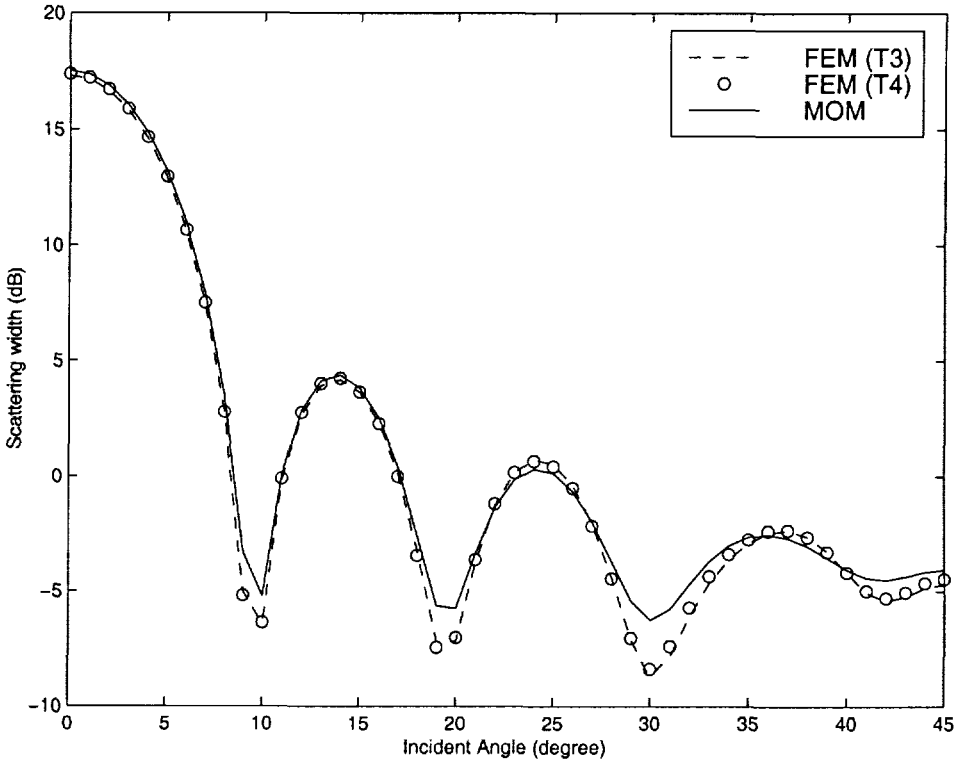

Figure 6.2: Comparison of monostatic echo widths ($\frac{\sigma}{\lambda}$) calculated by the FEM and MOM.

equations. Although, these are exact prior to discretization, they suffer from the fact that they are global conditions and create full matrices. However, if they are used just to obtain equivalent sources of the original source as an intermediate step, it may provide better conditions for the exterior region than ABCs.

In the exterior region, the total field can be represented by the superposition of the original incident fields and scattered fields. Both are due to the source in the FEM domain, but it will be represented by the equivalent source. Therefore, the equivalent source may be arisen from an interior source or an interior scatterer. For the TM_z polarization, these equivalent sources are expressed as

$$J_z = \hat{z} \cdot \hat{n} \times (\hat{t} H_t) = H_t = \frac{1}{jk_o\eta} \frac{\partial E_z}{\partial n} \quad on \quad \partial\Gamma \tag{6.10}$$

$$M_z = \hat{t} \cdot (\hat{n} E_t) \times \hat{n} = E_z \quad on \quad \partial\Gamma \tag{6.11}$$

For the TE_z polarization, the equivalent sources are given by

$$J_t = \hat{t} \cdot \hat{n} \times (\hat{z} H_t) = -H_z \quad on \quad \partial\Gamma \tag{6.12}$$

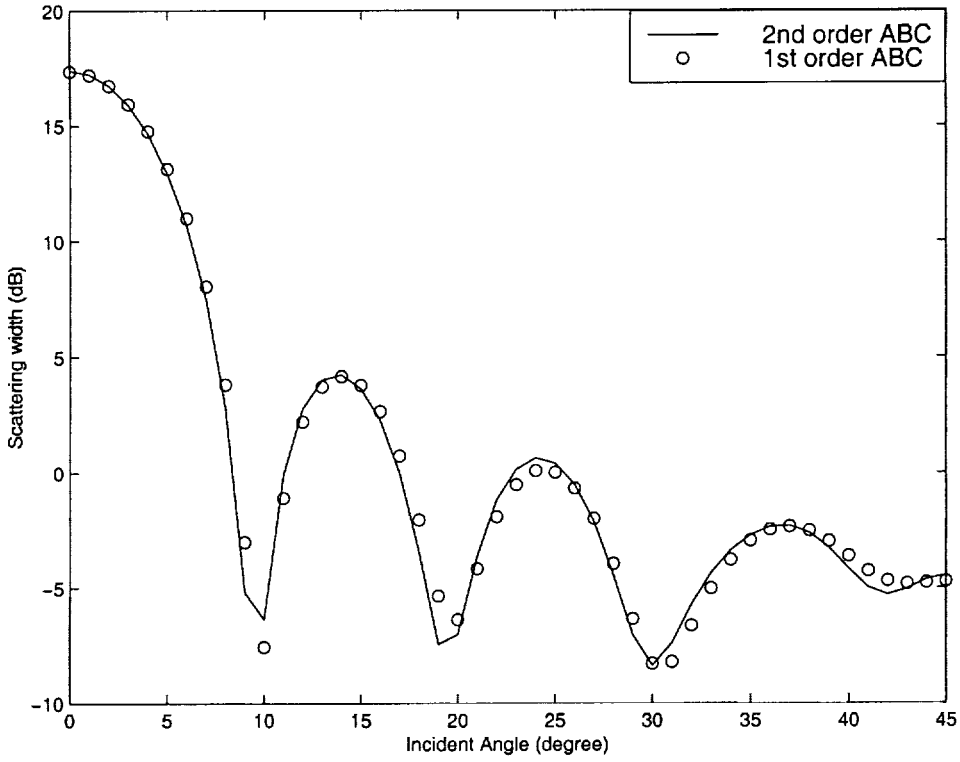

Figure 6.3: Comparison of monostatic echo widths ($\frac{\sigma}{\lambda}$) calculated by FEM using 1st order ABC and the 2nd order ABCs.

$$M_z = \hat{z} \cdot (\hat{t} H_t) \times \hat{n} = -E_t = -\frac{j\eta}{k_o} \frac{\partial H_z}{\partial n} \quad on \quad \partial\Gamma \tag{6.13}$$

where $\hat{n}$ is the outward unit normal vector to the surface, and $\hat{t}$ is the unit tangent vector defined so that $\hat{n} \times \hat{t} = \hat{z}$. In the exterior region, the equivalent source must satisfy EFIE for TM_z polarization or MFIE for TE_z polarization, which are given by

$$E_z^{inc}(\rho) = M_t(\rho) + \hat{z} \cdot \nabla \times \int_{\partial\Gamma} \bar{M}_t(\rho') \frac{1}{4j} H_0^{(2)}(kR) d\rho' + jk\eta \int_{\partial\Gamma} J_z(\rho') \frac{1}{4j} H_0^{(2)}(kR) d\rho' \tag{6.14}$$

$$H_z^{inc}(\rho) = -J_t(\rho) - \hat{z} \cdot \nabla \times \int_{\partial\Gamma} \bar{J}_t(\rho') \frac{1}{4j} H_0^{(2)}(kR) d\rho' + \frac{jk}{\eta} \int_{\partial\Gamma} M_z(\rho') \frac{1}{4j} H_0^{(2)}(kR) d\rho' \tag{6.15}$$

Let's consider the TM_z polarization case shown in Figure 6.4. The interior region is discretized with a linear basis function of triangular elements. As consequence, the boundary Γ is broken into N_b short segments. The electric field on the boundary is piecewise-linear whereas the magnetic field is piecewise-constant; therefore, the basis function for EFIE requires the same type of basis function in order to provide

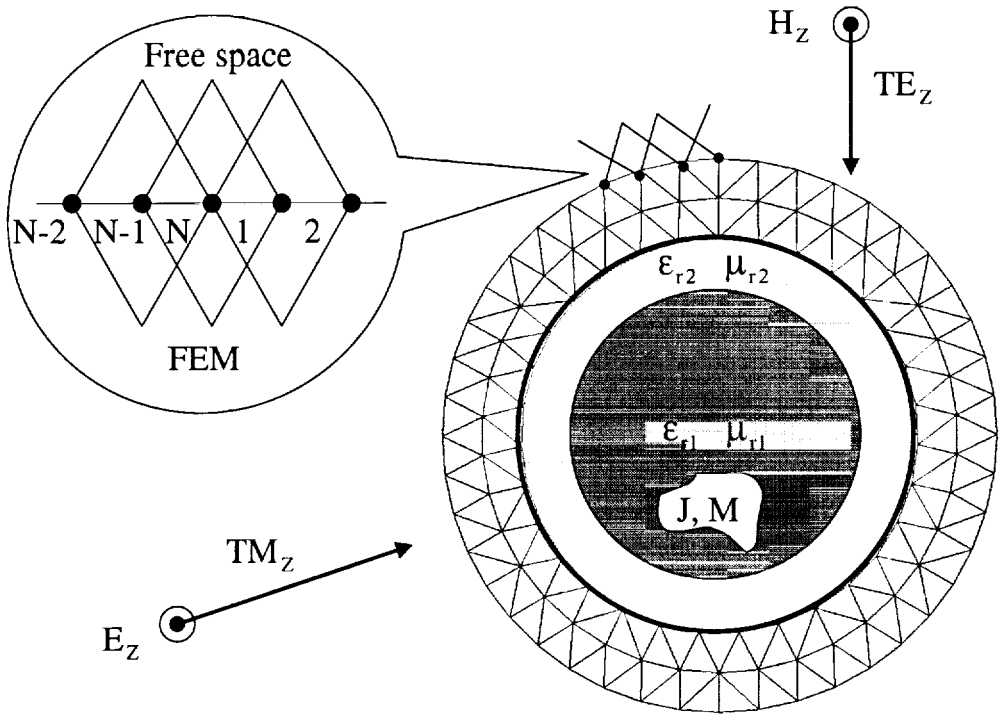

Figure 6.4: Hybrid between an FEM and an integral equation using linear basis functions on the boundary.

continuity conditions for both fields. Moreover, using the simple testing function, such as Dirac delta functions located in the center of each cell, (6.14) can be expressed as a matrix equation

$$\mathbf{e}^{inc} = \mathbf{L}\mathbf{k}_t + \mathbf{M}\mathbf{j}_z \tag{6.16}$$

where $\mathbf{L}$ and $\mathbf{M}$ are square matrix and $\mathbf{e}^{inc}$, $\mathbf{k}_t$ and $\mathbf{j}_z$ are all column vectors. The equation can be solved for $\mathbf{j}_z$ to get

$$\mathbf{j}_z = \mathbf{M}^{-1}\mathbf{e}^{inc} - \mathbf{M}^{-1}\mathbf{L}\mathbf{k}_t \tag{6.17}$$

In fact, this is another type of radiation boundary condition and can be applied to FEM formulation instead of ABCs. Moreover, it is more general than the ABCs, since the shape of the boundary is not restricted.

In order to hybridized with the FEM, rewrite the discretized weak form of the Helmholtz equation in a matrix form

$$\begin{bmatrix} \mathbf{I}_{ii} & \mathbf{I}_{ib} & \mathbf{0} \\ \mathbf{I}_{bi} & \mathbf{E} & \mathbf{J} \end{bmatrix} \begin{bmatrix} \mathbf{e}_{in} \\ \mathbf{e}_b \\ \mathbf{j}_z \end{bmatrix} = \begin{bmatrix} \mathbf{0} \\ \mathbf{0} \end{bmatrix} \tag{6.18}$$

where the entries of $I_{i,i}$, $I_{i,b} = I_{b,i}$ and $\mathbf{E}$ represent interior interactions and can be obtained from

$$\int\int_{\Gamma} \frac{1}{\mu_r} \nabla N_i \cdot \nabla N_j - k^2 \epsilon_r N_i N_j dA \tag{6.19}$$

and the entries of $\mathbf{J}$ can be expressed as

$$J_{i,j} = -jk_o\eta \int_{\partial\Gamma} B_i \tilde{B}_j d\Gamma \tag{6.20}$$

The basis function B_i is the projection of N_i on the boundary, and $\tilde{B}_i$ is the linear basis function for the electric equivalent current J_z given by

$$J_z(\rho) = \sum_{n=1}^{N_b} j_{zn} \tilde{B}_n \tag{6.21}$$

Finally, substituting (6.17) into (6.18) will lead to

$$\begin{bmatrix} \mathbf{I}_{ii} & \mathbf{I}_{ib} \\ \mathbf{I}_{bi} & \mathbf{E} - \mathbf{J}\mathbf{M}^{-1}\mathbf{L} \end{bmatrix} \begin{bmatrix} \mathbf{e}_{in} \\ \mathbf{e}_b \end{bmatrix} = \begin{bmatrix} \mathbf{0} \\ -\mathbf{J}\mathbf{M}^{-1}\mathbf{e}^{inc} \end{bmatrix} \tag{6.22}$$

The combined system (6.22) forms a complete system for the solution of the total fields. Because of the global condition in the radiation condition, the part of the matrix with rows and columns associated with nodes on the boundary will be fully populated. The sparsity pattern of an example problem is depicted in Figure 6.5.

It should be mentioned that care must be exercised in the computation of $\mathbf{L}$ and $\mathbf{M}$ matrix. Specifically, there are three cases, as can be seen in Figure 6.6, where the integrand becomes singular in every row, because the argument of 2D Green's function becomes zero. To undertake more accurate evaluation, an asymptotic form of singular parts are subtracted from the original integral which results in an integral that can be computed by a numerical way. The remaining term which has to be added to the first integral contains the singularity but can be evaluated analytically. After calculating the total field, the equivalent current $\mathbf{j}_z$ can be calculated from (6.17). Once the J and M are known, the scattered fields in the exterior region can

be obtained using EFIE. In the far-field range, the scattered field can be calculated using the following formulae:

$$E_s = I_1 + I_2 \tag{6.23}$$

$$I_1 = -\frac{k_o \eta}{4}\sqrt{\frac{2j}{\pi k_o}}\sum_{n=1}^{N_b} j_{zn}\int_{cell}\tilde{B}_n e^{jk_o r'\cos(\varphi-\varphi')}d\Gamma' \tag{6.24}$$

$$I_2 = \frac{k_o}{4}\sqrt{\frac{2j}{\pi k_o}}\sum_{n=1}^{N_b} e_{bzn}\int_{cell} B_n \cos(\varphi-\varphi')e^{jk_o r'\cos(\varphi-\varphi')}d\Gamma' \tag{6.25}$$

The above formulation for TM_z-polarization is implemented to predict the scattering width of an arbitrary shape of cylinder. To validate the BIE 2D code, the bistatic scattering width of a circular cylinder having 2λ radius is predicted. Figure 6.7 shows the bistatic echo width obtained by the BIE method in comparison with MOM results.

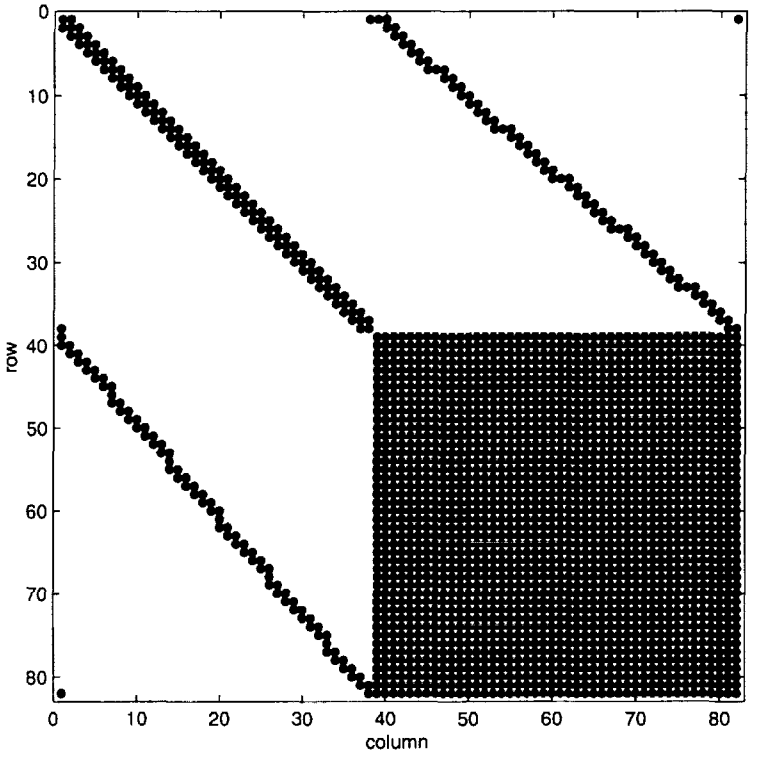

Figure 6.5: Matrix sparsity pattern after the hybridization.

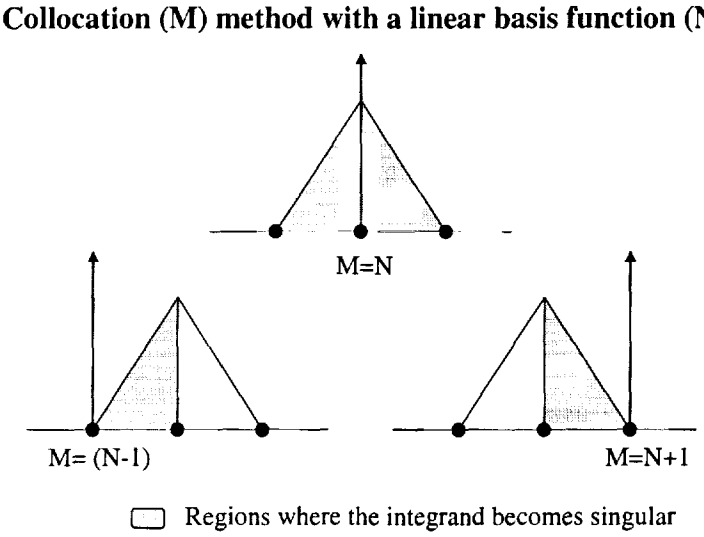

Figure 6.6: Cases where **M** and **L** elements become singular.

IV. Hybridization of FEM with PO

Although a hybridization of FEM with PO for 3D geometries was presented by the authors elsewhere, it was not a complete formulation. Three major issues pointed out to be improved are:

a. Inclusion of higher order interactions between the source and the obstacle

b. Augmentation of diffractions in the analysis

c. Improvement of computation time needed for the PO integration

With an aim to finding causes of those problems and hopefully provide solutions, it was necessary to simplify the problem in terms of size and complexity. Therefore, a good starting point was to develop an FEM/PO code in 2D-space. The geometry and coordinate system of the problem is shown in Figure 6.8. In the absence of any obstacle, the line source produces cylindrical waves. The exact solution for an electric line source in a cylindrical coordinate system is given by

$$E_z = -I\frac{k_\circ \eta}{4} H_0^{(2)}(k_\circ \rho) \tag{6.26}$$

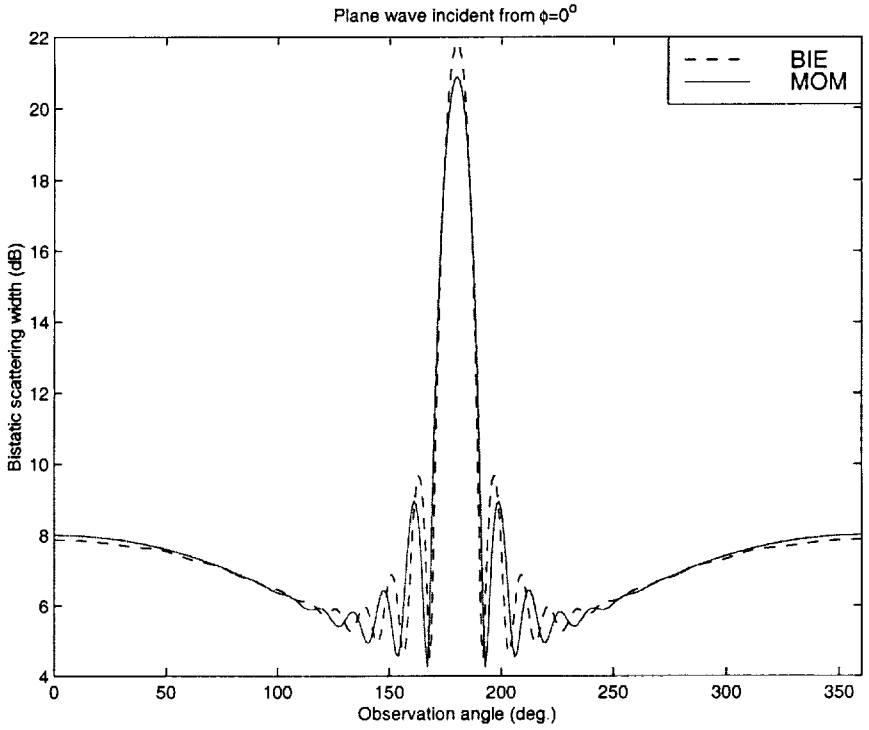

Figure 6.7: Bistatic echo widths ($\frac{\sigma}{\lambda}$) predicted by BIE and MOM when the plane wave is incident from $\varphi = 0°$.

$$H_\phi = -jI\frac{k_\circ}{4}H_1^{(2)}(k_\circ\rho) \tag{6.27}$$

Using the 2D FEM for TM_z polarization, the radiated field due to a line source in the absence of an obstacle can be calculated from (6.1) with $f = -jk_\circ Z_\circ J_z$. By setting discretization size of $\lambda/20$, the error of the fields for all observation angles was confined within 3%. In the presence of the obstacle, here a PEC body, the radiated fields will induce an electric current on the surface which may be evaluated using the PO approximation. Once the PO currents are available then, the scattered fields from the obstacle can be calculated from the EFIE with zero magnetic currents:

$$E_s = -jk_\circ\eta\int_{lit} J_{PO}(\rho')\frac{1}{4j}H_0^{(2)}(k_\circ|\rho-\rho'|)d\Gamma' \tag{6.28}$$

where J_{PO} is the PO current defined by

$$J_{PO} = 2(\hat{n}\times H_f) \quad if\ \hat{k}\cdot\hat{n} < 0 \tag{6.29}$$

The corresponding magnetic fields on the surface of the obstacle can be obtained using Maxwell equations:

$$H_f = \frac{-j\eta}{k_\circ}\hat{z} \times \nabla E_f \tag{6.30}$$

Since the derivative of the 2D Green's function with respect to the observation points can be carried out with ease, the magnetic fields can be calculated without any approximation. Owing to the PO approximation which is denoted as a forward reaction in the figure,the obstacle is replaced by the PO current in free-space; therefore, the exterior of the FEM domain must satisfy (6.14). At this time, E_z^{inc} should be replaced by E_s in (6.28). If the source were given, such as $f(\rho)$, the E_s would be calculated exactly without the PO approximation using

$$E_z^{inc}(\rho) = -\int\int f(\rho')\frac{1}{4j}H_0^{(2)}(k_\circ|\rho - \rho'|)d\Gamma' \tag{6.31}$$

It is also possible that other basis functions may be applied on the obstacle in order to get even better current approximation; however, they should be included in the matrix system, so their application will be limited only to small obstacles. Figure 6.9 shows the backward reactions, which represent backward radiations from the PO source to the FEM domain and eventually perturb previous FEM solutions. The reaction between the forward and backward direction can be expressed as a matrix equation

$$\begin{bmatrix} \mathbf{I}_{ii} & \mathbf{I}_{ib} \\ \mathbf{I}_{bi} & \mathbf{E} - \mathbf{J}\mathbf{M}^{-1}\mathbf{L} \end{bmatrix} \begin{bmatrix} \mathbf{e}_{in} \\ \mathbf{e}_b \end{bmatrix} = \begin{bmatrix} \delta_\mathbf{m} \\ \mathbf{0} \end{bmatrix} + \begin{bmatrix} \mathbf{0} \\ -\mathbf{J}\mathbf{M}^{-1}\mathbf{e}_s \end{bmatrix} \tag{6.32}$$

where $\delta_\mathbf{m}$ is a column vector having only one nonzero element at the node where the electric line source is located; whereas, $\mathbf{e}_s$ is a column vector whose entries are scattered fields evaluated on the boundary nodes. Note that the second vector on the right-hand side account for the presence of an obstacle. In fact, the system matrix on the left-hand side and the first source vector on the right-hand side were already used to calculate the equivalent currents around the line source in the absence of the obstacle. Therefore, the matrix equation can be rewritten as

$$\mathbf{A}_1[\mathbf{e}_1 + \delta\mathbf{e}] = \mathbf{A}_1\mathbf{e}_2 = \mathbf{b}_1 + \delta\mathbf{b} \tag{6.33}$$

$$\mathbf{e}_2 = \mathbf{e}_1 + \delta\mathbf{e} = \mathbf{e}_1 + \mathbf{A}_1^{-1}\delta\mathbf{b} \tag{6.34}$$

Note that the system matrix **A** will be the same as for the first step even for further iterations. From a computational efficiency point of view, **LU** factorization should be utilized to inverse the matrix **A**. The reason is that all that is required to obtain new $\delta\mathbf{e}$ will be just backward and forward substitutions, if both **L** and **U** are stored from the first step.

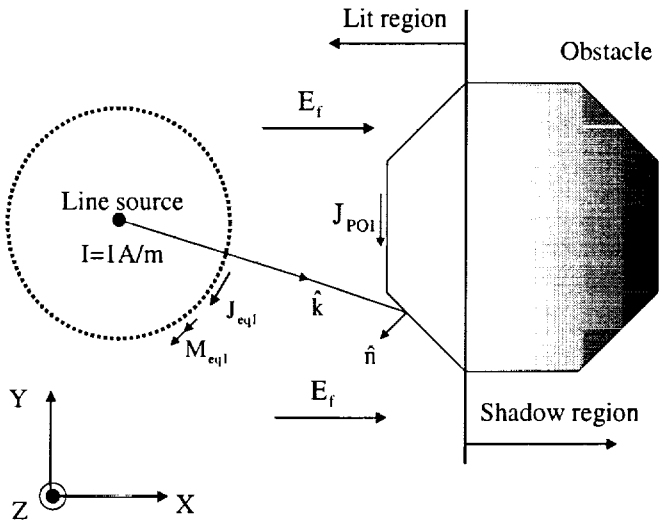

Figure 6.8: Electric line source near an obstacle (forward reaction).

The first example considered here is a line source near a strip. The distance between the source and the strip was 1.0 λ and the width of the strip was 2.0 λ. Figure 6.10 shows total fields computed by the FEM/PO in comparison to MOM predictions. The second order ABCs was used with the FEM/PO. The agreement between both results is shown to be excellent for both lit and shadow zones, even though the FEM/PO was performed without higher order iterations. From the width of the strip and the distance, the shadow region can be calculated in terms of φ angle as can be seen in the figure. It should be mentioned that the inclusion of higher oder effects will improve mainly the predictions in the lit zone. The improvement of the fields in the shadow zone can be accomplished only by supplementation of diffractions. Total field prediction for another example is shown in Figure 6.11. In this problem, the obstacle is chosen to be a circular cylinder having a radius of 1.0λ. Based on

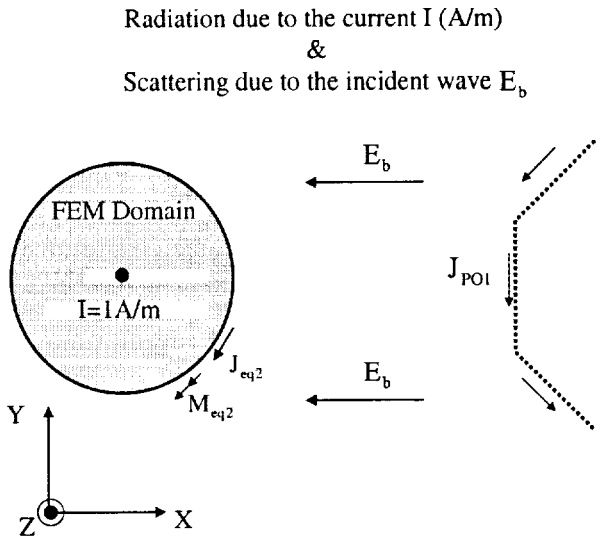

Figure 6.9: Electric line source near an obstacle (backward reaction).

the geometry, the lit and shadow region can be defined as marked in Figure 6.11. The comparison to the exact solution exhibits good agreement in most of the lit zone except near boundary called transition regions. Again, the higher order interactions are not yet included, since those are not incorporated into our 2D FEM/PO code. Instead of using ABCs to calculate the equivalent source, the 2D-BIE code is used to calculate PO currents. The comparison between the BIE/PO and ABC/PO is depicted in Figure 6.12. Basically, the total fields predicted by both scheme were identical. However, the BIE/PO will be used as for the future analysis, because it saves lots of computation efforts when higher oder interactions are taking into account. The main reason is its use of collocation method. Because of that, the calculations of the interactions are needed only at the matching points.

V. Hybridization of FEM with GTD or PTD

For the case where the obstacle has smooth and flat surface, the FEM/PO works well. If the body has more lit region from the source point of view, the performance of the FEM/PO would be even better. However, for the special geometry such as wedges,

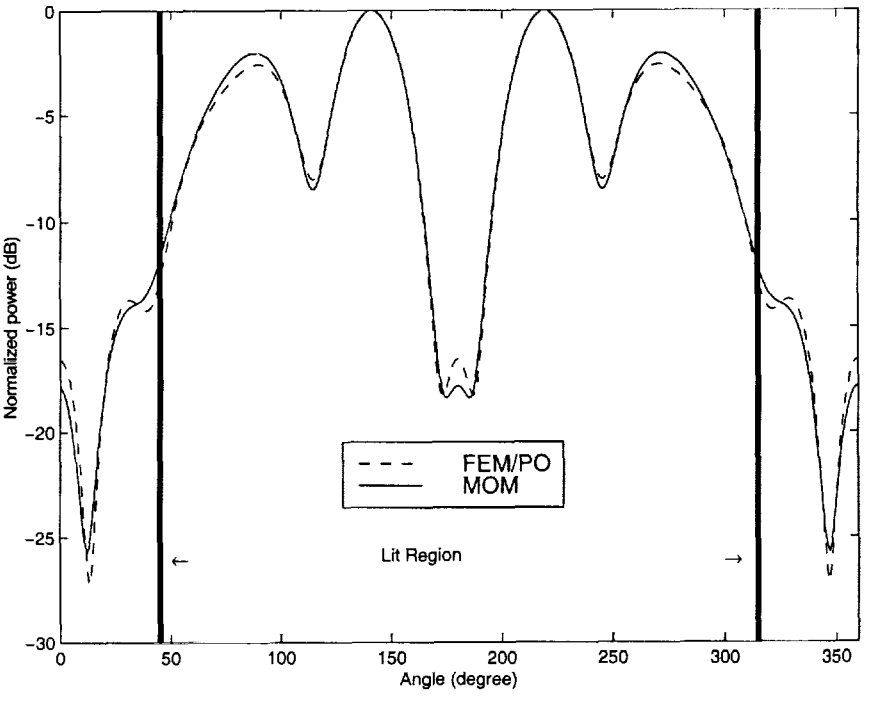

Figure 6.10: Total radiation fields due to a line source near a strip. The distance between the source and plate is 1.0λ and the width of the plate is 2.0λ. Comparison between FEM/PO and MOM predictions

the FEM/PO may fail but GTD solutions may be valid. The same approach used for the hybridization between the FEM and PO can be expanded for GTD as well. The problem under consideration is shown in Figures 6.13 and 6.14. In fact, the exact modal solutions are available in the form of an infinite series [17].

$$E_z^t = E_z^i + E_z^s = \begin{cases} \sum_\upsilon a_\upsilon J_\nu(\beta\rho) H_\upsilon^{(2)}(\beta\rho') \sin[\upsilon(\phi' - \alpha)] \sin[\upsilon(\phi - \alpha)] & \rho \leq \rho' \\ \sum_\upsilon a_\upsilon J_\nu(\beta\rho') H_\upsilon^{(2)}(\beta\rho) \sin[\upsilon(\phi' - \alpha)] \sin[\upsilon(\phi - \alpha)] & \rho \geq \rho' \end{cases} \tag{6.35}$$

where a_υ and υ are

$$a_\upsilon = \frac{-\omega\mu\pi I_e}{2(\pi - \alpha)} \tag{6.36}$$

$$\upsilon = \frac{mu}{2(\pi - \alpha)} \tag{6.37}$$

The magnetic field components can be obtained by using the Maxwell's equation as

$$H_\rho^t = \frac{-1}{j\omega\mu\rho} \begin{cases} \sum_\upsilon \upsilon a_\upsilon J_\nu(\beta\rho) H_\upsilon^{(2)}(\beta\rho') \sin[\upsilon(\phi' - \alpha)] \cos[\upsilon(\phi - \alpha)] & \rho \leq \rho' \\ \sum_\upsilon \upsilon a_\upsilon J_\nu(\beta\rho') H_\upsilon^{(2)}(\beta\rho) \sin[\upsilon(\phi' - \alpha)] \cos[\upsilon(\phi - \alpha)] & \rho \geq \rho' \end{cases} \tag{6.38}$$

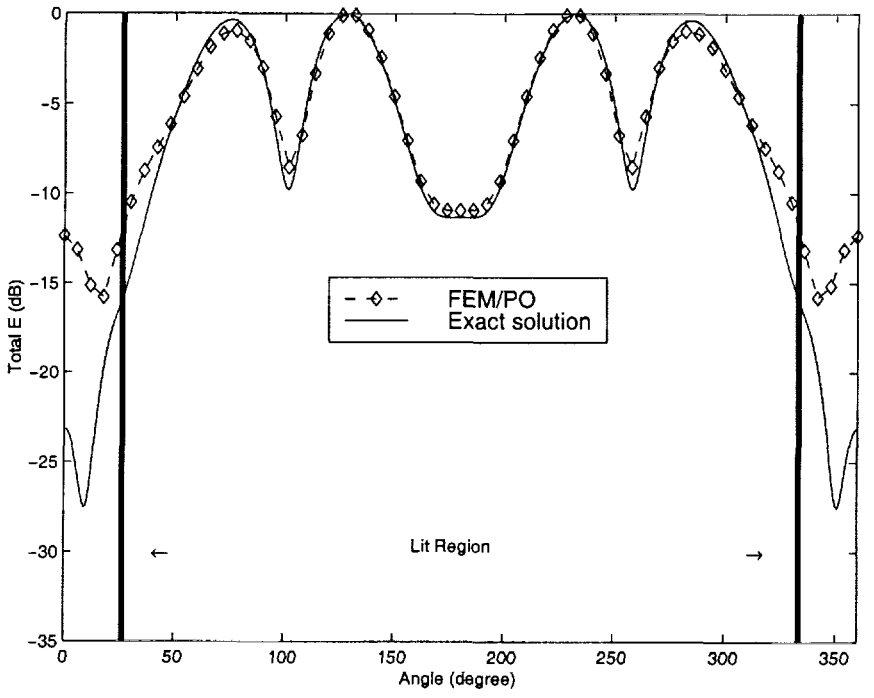

Figure 6.11: Total radiation fields due to a line source near a cylinder. The distance between the source and the cylinder is 2.0λ and the radius of the cylinder is 1.0λ. Comparison between FEM/PO predictions and the exact solution.

$$H_\phi^t = \frac{k_\circ}{j\omega\mu} \begin{cases} \sum_\upsilon a_\upsilon J'_\nu(\beta\rho) H_\upsilon^{(2)}(\beta\rho') \sin[\upsilon(\phi' - \alpha)] \sin[\upsilon(\phi - \alpha)] & \rho \leq \rho' \\ \sum_\upsilon a_\upsilon J_\nu(\beta\rho') H_\upsilon'^{(2)}(\beta\rho) \sin[\upsilon(\phi' - \alpha)] \sin[\upsilon(\phi - \alpha)] & \rho \geq \rho' \end{cases} \tag{6.39}$$

Using the above total magnetic fields, the surface currents on the wedge can be obtained by

$$J_{GTD} = \hat{n} \times (\hat{\rho} H_\rho^t + \hat{\phi} H_\phi^t) = (\hat{n} \times H_\rho^t)_z \tag{6.40}$$

Instead of using J_{PO} in (6.28), J_{GTD} can be substituted to get scattered fields which will allow us to calculate higher order interactions in the FEM analysis. However, if both source and observation points are in the far-field range at the frequency of operation, then the asymptotic solution or GTD should be used because of its high convergence rate and accuracy. In GTD, the total scattered fields consist of GO fields and diffracted fields. At the given source point and observation points, GO fields can be calculated easily using geometrical optics; whereas diffractions fields are obtained using the diffraction coefficients which are available in [17].

The physical theory of diffraction (PTD) for the wedge can also be applied in conjunction with the FEM. Based on the PTD theory [18], the PO current needs to

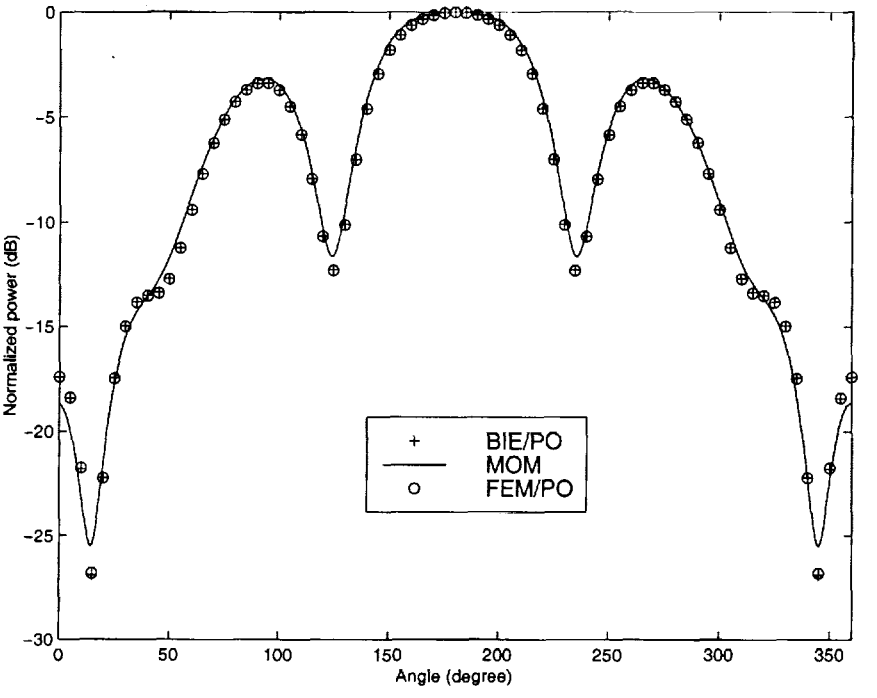

Figure 6.12: Total radiation fields due to a line source near a cylinder. The distance between the source and the cylinder is $\frac{5}{3}\lambda$ and the radius of the cylinder is $\frac{5}{6}\lambda$. Comparison among FEM/PO, BIE/PO predictions and the exact solution.

be supplemented by the contributions from the nonuniform current

$$E^s_{total} = E_{PO} + (E^d_K - E^d_{PO}) = E^{unif} + E^{nu} \tag{6.41}$$

where the E^d_K represents diffracted fields calculated from Keller's diffraction coefficients. The electric field due to the physical optics current on the illuminated face is already calculated, so here only the diffracted field due to the PO current will be addressed. Based on the method of stationary phase, the fields due to the PO current is referred to as the end-point contribution. Using the geometry shown in Figure 6.13, the nonuniform current [19] is known to be

$$J_{nu} = -2J_{PO}\frac{j}{\pi}\left[F(x) - \frac{e^{-jx^2}}{2jx}\right] \tag{6.42}$$

where $F(x)$ is the Fresnel function and defined by

$$F(x) = \int_x^\infty e^{-jt^2}dt \tag{6.43}$$

More general expressions for other than the half-plane are also available. In order to treat the obstacle using the PTD, the approximated PO current in (6.28) should be

replaced by the PTD currents given by

$$J_{PTD} = J_{PO} + J_{nu} \tag{6.44}$$

If the obstacle is a cylindrical body, the UTD can provide the scattered field not only in the lit and shadow regions but also in the transition regions without any discontinuity. Figure 6.14 shows a detailed geometry for scattering from a cylinder. For an observation point in the lit region, the reflected field is given by

$$E^r(\rho) = E^i(Q^r) R_s \sqrt{\frac{\rho^r}{\rho_r + s^r}} e^{-jks^r} \tag{6.45}$$

where $E^i(Q^r)$ is the incident field at the reflection point at Q_r, and here only TM_z or soft-polarization is considered. Distance parameters are defined in the Figure 6.14. The generalized reflection coefficient for this polarization is given by

$$R_s = -\sqrt{\frac{-4}{\zeta_p}} e^{-j(\zeta_p)^3/12} \left\{ \frac{e^{-j\pi/4}}{2\zeta_p\sqrt{\pi}} [1 - F(X_p)] + \hat{P}_s(\zeta_p) \right\} \tag{6.46}$$

where

a. $F(x)$ is the transition function already used in connection with edge diffraction in GTD and PTD.

b. The argument of the transition function is $X_p = 2k_o L_p \cos^2(\theta_i)$ and the distance parameter L_p is given by

$$L_p = \frac{s^r s^i}{s^r + s^i} \tag{6.47}$$

c. The ζ_p is the Fock parameter associated with the reflected field in the lit region

$$\zeta_p = -2m(Q_r)\cos\theta_i \tag{6.48}$$

d. The value of the curvature parameter at the reflection point is expressed as a function of the radius of curvature a_o of the surface at Q_r

$$m(Q_r) = \left[\frac{k_o a_o(Q_r)}{2} \right]^{1/3} \tag{6.49}$$

e. Finally, the function $\hat{P}_s$ is the *Pekeris caret function* and can be written in terms of *Fock scattering function* $p^*(x)$ [20].

$$\hat{P}_s(x) = p^*(x)e^{-j\pi/4} - \frac{e^{-j\pi/4}}{2x\sqrt{\pi}} \tag{6.50}$$

In the shadow region, the diffracted field is given by

$$E^d(\rho_d) = E^i(Q')T_s\frac{e^{-jks^d}}{\sqrt{s^d}} \tag{6.51}$$

$E^i(Q')$ is a GO type incident field at the attachment point Q'. Observation point ρ_d may be in the shadow region and even on the shadow boundary. The UTD surface diffraction coefficient, T_s, calculates the surface waves launched from two detachment points on the circular cylinder. Figure 6.15 shows decomposed GO field and the diffracted fields due to a line source in the presence of a circular cylinder. The distance between the source and the cylinder was 2.0λ and the radius of the cylinder was 1.0λ. As can be seen, the GO fields are zero in the shadow zone, so that the diffractions will be the main contribution for the interactions.

VI. Conclusions

In this report, an iterative algorithm was developed to analyze the radiation due to a source in the presence of a large body. In order to take the presence of an obstacle into account, the right-hand side vector of the system equation is modified at each iteration. Updated right-hand side vector contains scattering fields which represent backward radiation due to an induced current on an obstacle. To get a better insight of the problem, a 2D hybrid code was developed and used. As for the FEM analysis, BIE formulation was added to the conventional mesh truncation scheme, ABCs.

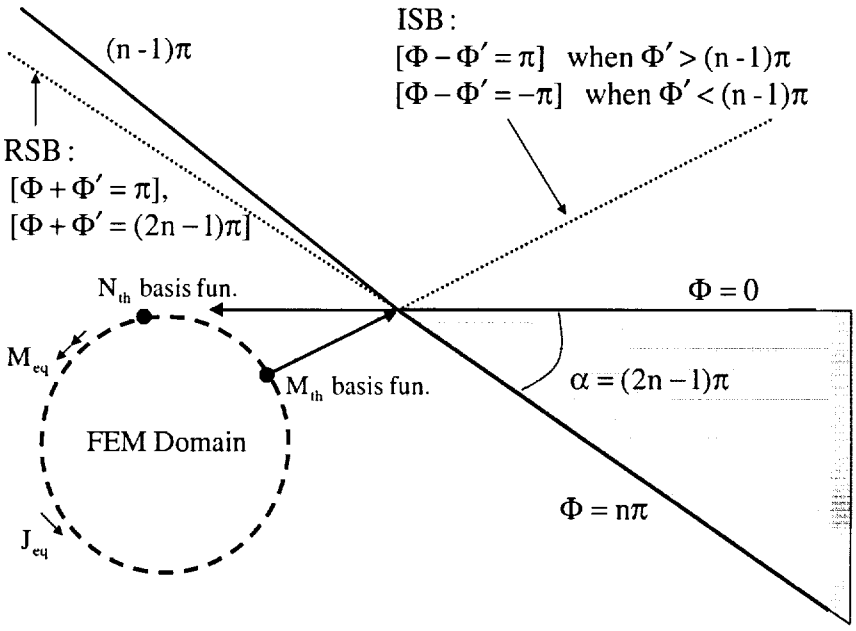

Figure 6.13: FEM analysis in the presence of wedge.

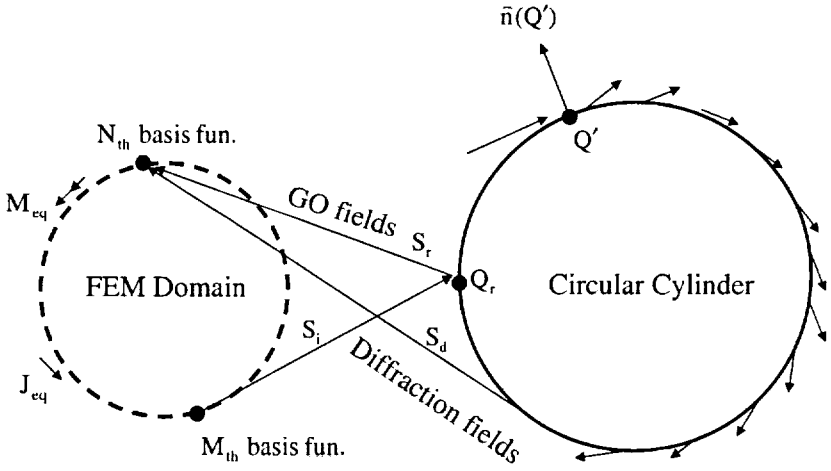

Figure 6.14: FEM analysis in the presence of a circular cylinder.

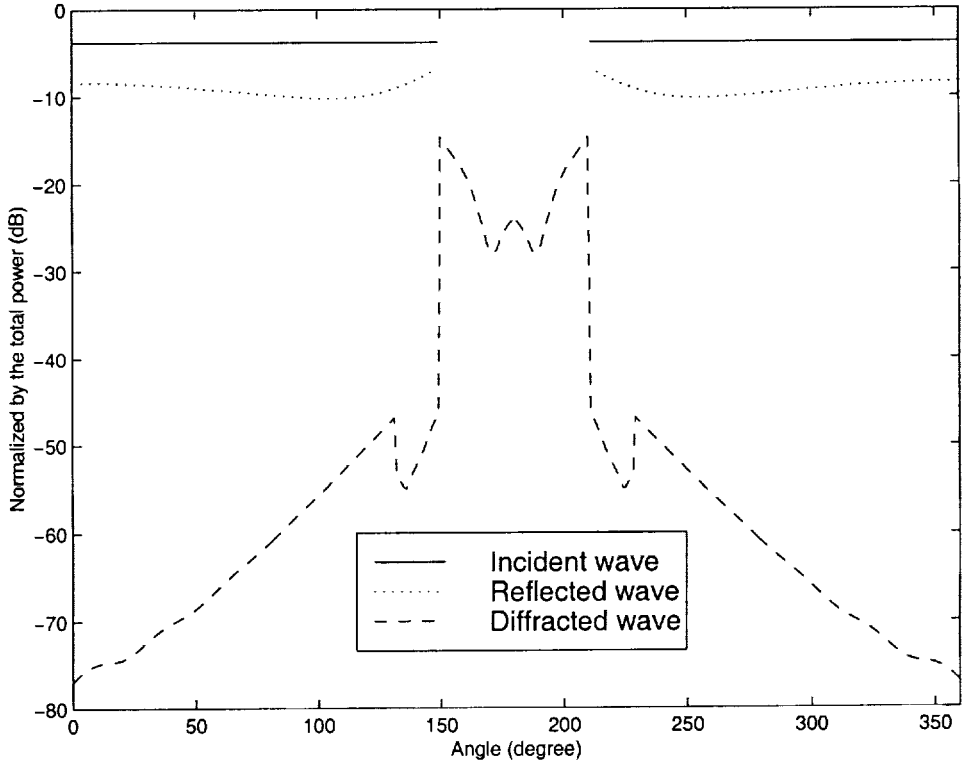

Figure 6.15: Decomposed GO fields and diffracted fields due to a line source in the presence of a circular cylinder. The distance between the source and the cylinder was 2.0λ and the radius of the cylinder was 1.0λ.

Chapter 7

Spectral Methods

I. Introduction

In the past, the authors introduced a family of spectral methods to provide an alternative way to handle efficiently electrically large computational domains, such as helicopter airframes. Spectral methods are very powerful due to their high accuracy, exponential convergence, and negligible dispersion and dissipation. All these attributes are extremely important in computational electromagnetic problems. Some of the key elements in the formulation of spectral methods were presented by the authors elsewhere. The high accuracy of the spectral methods was demonstrated through numerical experiments and compared to the accuracy of the finite-difference methods.

In this report, the spectral methods are applied for the first time to the solution of one-dimensional electromagnetic problems. Here, the ability of spectral methods to solve electromagnetic problems will be demonstrated, and their accuracy will be illustrated through numerical experiments. Their accuracy will also be compared to the one of the standard FDTD algorithm. Spectral methods, as expected, will exhibit orders of magnitude better accuracy than FDTD because of their negligible dispersion. Different types of numerical experiments are presented here. Initially, the entire domain Chebychev collocation method is applied to solve an 1-D TM^z-mode propagation problem. Furthermore, the PML technique is used in the context of spectral methods to simulate "open space" problems. Then, the ideas of interior domain grids and fictitious points are presented and applied to a multi-domain approach in the last two sections. This material is based on a recently published paper [21].

From the material presented here, it will be shown that the spectral methods are very promising for numerical electromagnetic analysis. Our ultimate goal is to apply and extend these methods initially to generic 2-D and 3-D problems and then to radiation problems.

II. Solving Maxwell's Equations

Here, the one-dimensional (1-D) Maxwell's equations for the TM^z mode given by

$$\frac{\partial H_y}{\partial t} = \frac{1}{\mu}\left(\frac{\partial E_z}{\partial x} - \rho H_y\right) \tag{7.1}$$

$$\frac{\partial E_z}{\partial t} = \frac{1}{\epsilon}\left(\frac{\partial H_y}{\partial x} - \sigma E_z\right) \tag{7.2}$$

are examined. Direct application of the entire domain Chebychev collocation method is quite straightforward. The spatial derivatives are approximated by using the differentiation matrices (DM) and an appropriate grid. Assuming a Chebychev grid $x_i,\ i = 0, 1, ..., N$ and assuming grid values for the fields E_{z_i} and $H_{y_i},\ i = 0, 1, ..., N$ we can write the *semi-discrete* form of Maxwell's equations as:

$$\frac{\partial \underline{H}_y}{\partial t} = \frac{1}{\mu}\left(D\underline{E}_z - \rho\underline{H}_y\right) \tag{7.3}$$

$$\frac{\partial \underline{E}_z}{\partial t} = \frac{1}{\epsilon}\left(D\underline{H}_y - \sigma\underline{E}_z\right) \tag{7.4}$$

where $\underline{H}_y$ and $\underline{E}_z$ are the vectors containing the grid values of the field components and D the differentiation matrix.

The first numerical experiment simulates a 1-D domain, one wavelength long, for the TM^z-mode. The domain was excited with a sinusoidal source at the left hand side, and was terminated at the right boundary using the exact solution. This problem was solved using either the Chebychev collocation method or the FDTD second-order accurate scheme for different number of points. The error was computed in the maximum norm at time t = 2T, where T is one period. Figure 7.1 compares the FDTD results with the ones of the spectral method. Obviously, the spectral method outperforms the FDTD method in terms of accuracy. It is quite impressive that in order to get the same accuracy as the one that the spectral method provides with

a computational domain of 70 points, an FDTD domain of 1024 points is needed. Therefore, by using spectral methods, high accuracy can be achieved without very fine spatial discretization. The main drawback though of spectral methods is that they exhibit very restrictive stability criteria, forcing us to discretize very finely in time. However, there have been proposed approaches that deal successfully with this problem and accomplish to relax the time-step restrictions.

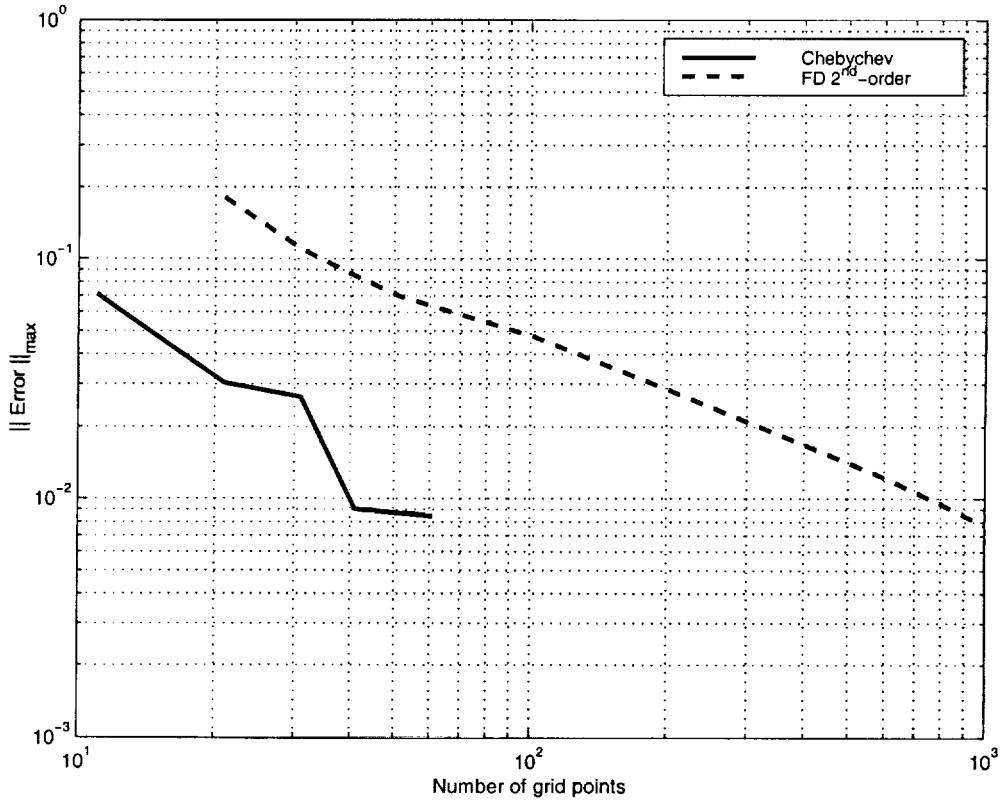

Figure 7.1: Maximum error in the solution of the 1-D TM mode at t=2T.

One main concern in electromagnetic simulations is the solution of unbounded space problems, often called "open-space" problems. The correct treatment of such problems is to simulate a computational domain large enough to enclose the structure of interest, and truncate it by applying appropriate artificial boundary conditions on the outer perimeter of the domain, which simulate its extension to infinity. These boundary conditions should allow the outward propagating wave to exit the domain and suppress spurious reflections of this wave to an acceptable level. Depending upon their theoretical basis, outer grid boundary conditions of this type have been

called either radiation boundary conditions (RBCs) or absorbing boundary conditions (ABCs). Initially, ABCs were obtained by applying the theory of one-way wave equations derived by Engquist and Majda [22]. Recently, a novel and pioneering ABC was introduced by Berenger [23], who used a non-physical absorbing (lossy) material adjacent to the computational boundary to truncate the domain, and he called this approach *Perfectly Matched Layer* (PML). The PML exhibits characteristics that permit electromagnetic waves of arbitrary frequency and angle of incidence to be absorbed while maintaining the impedance and velocity of a lossless dielectric. Berenger reported reflection coefficients for PML in two dimensions significantly better than second- and third-order one-way wave equation (OWWE) based ABCs.

Here, the PML concept is applied in the context of spectral methods to truncate an 1-D domain. According to Berenger the PML material should have properties so that the following relation is satisfied:

$$\frac{\sigma}{\epsilon} = \frac{\sigma^*}{\mu} \tag{7.5}$$

where ϵ and μ are the properties of the material we want to match, e.g., in the case of free space $\epsilon = \epsilon_0$ and $\mu = \mu_0$. To implement the PML we just need to assign to some of the grid points towards the end of the domain such material properties. Two are the key elements in an effective PML implementation:

- Define a desirable and acceptable reflection coefficient.
- Define an appropriate conductivity grading so that no rapid changes in conductivities occur in the domain creating numerical reflections.

The effectiveness of PML is shown here by solving again an 1-D domain which is terminated by PML with a desirable reflection coefficient 10^{-6} and backed by PEC walls. The grading of the conductivity is quadratic. The Chebychev collocation method again is used to solve a half-wavelength long domain. The right hand side end of the computational space is the PML, and a Gaussian pulse was excited at the left hand side end. The pulse propagates along the domain (towards the right) until it enters the PML where is gets absorbed. Many simulations were performed with different number of grid points for the PML, and it was found that PML works equivalently well in the spectral methods as in the FD methods. A sample of these

results is shown in Figure 7.2 where frames of the propagating pulse are plotted in the same graph for a case where 16 points were used for the PML termination. Clearly, this figure illustrates the absorption of the pulse in the PML. Therefore, PML can be used to terminate effectively computational domains in the context of spectral methods.

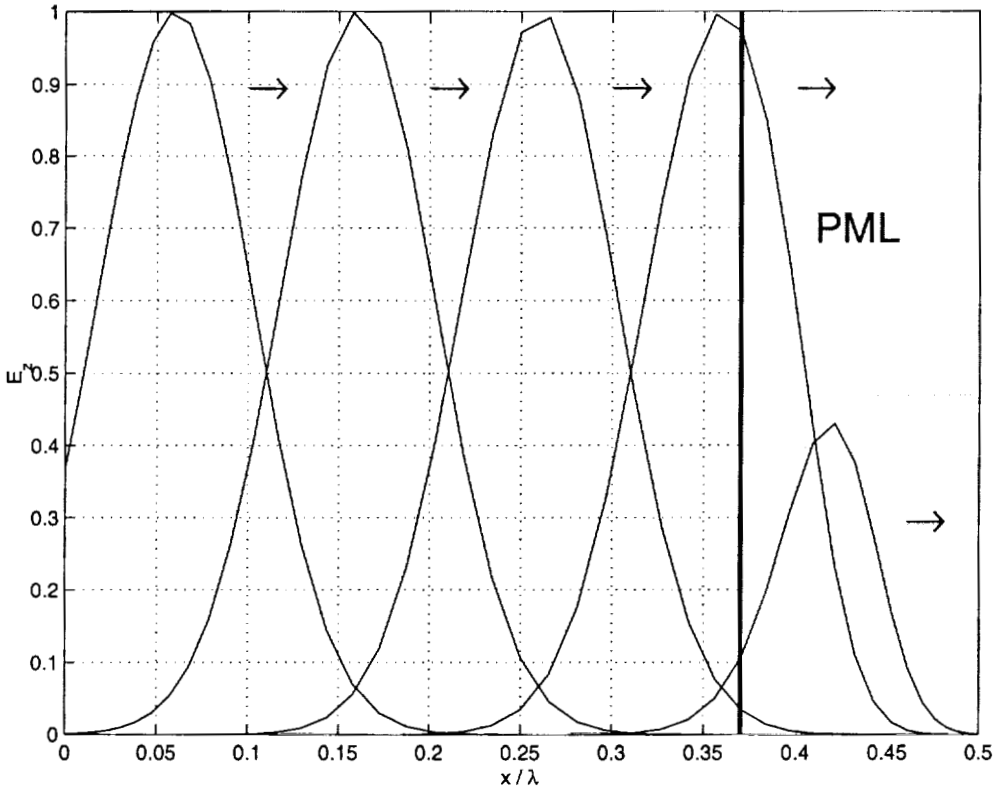

Figure 7.2: Traveling pulse in 1-D domain terminated with PML.

III. Interior Domain Grids and Fictitious Points

The material that is illustrated here is based on a recently published paper [21]. As claimed in this paper, "Accuracy can be gained by clustering a grid less and using the approximations only well within the interior". Given a grid of points x_j, $j = 1, ..., N$, the interpolation error for a smooth function is given by:

$$f(x) - p_{N-1}(x) = \frac{f^{(N)}(\xi)}{N!} \prod_{j=1}^{N} (x - x_j) = \frac{f^{(N)}(\xi)}{N!} \psi(x) \tag{7.6}$$

for some $\xi \in [x_1, x_N]$. The $\psi(x)$ is called the remainder, and it is known from interpolation theory that it is minimized in the max-norm over [-1,1] when the nodes are forming a Chebychev grid. Figure 7.3 illustrates the remainder for a Chebychev and an equispaced grid for $N = 10$. Notice that both grids are interior meaning that they do not contain the ends of the interval. Notice that the remainder of the equispaced grid is large near the ends of the interval (Runge phenomenon) whereas the remainder of the Chebychev is larger over most of the interval. Thus, maybe a better choice for a grid is to have node distribution between the Chebychev and the equispaced ones.

Other node distributions are defined in [21]. According to this paper a closed grid, meaning that the endpoints are included, is defined implicitly by

$$\frac{j}{N} = \int_{-1}^{x_j} c_\gamma (1 - x^2)^{-\gamma} dx \tag{7.7}$$

$$c_\gamma = \frac{\Gamma\left(\frac{3}{2} - \gamma\right)}{\sqrt{\pi}\Gamma\left(1 - \gamma\right)} \tag{7.8}$$

where x_j for $j = 0, 1, ..., N$ are the grid points. However, an open grid, i.e., not containing the end points, is defined by

$$\frac{j - \frac{1}{2}}{N} = \int_{-1}^{x_j} c_\gamma (1 - x^2)^{-\gamma} dx \tag{7.9}$$

where x_j for $j = 1, ..., N$ are the grid points. These equations for either the open or the closed grids can be solved numerically for a specific $\gamma < 1$ to obtain the grid points. Notice that $\gamma = 0$ corresponds to the equispaced grid and $\gamma = 0.5$ corresponds to the Chebychev grid. Even though the optimal choice of grid in terms of error is the Chebychev one ($\gamma = 0.5$), it was suggested in [21] that a different choice of $0 < \gamma < 0.5$ can possibly have some advantages. To show how the locations of the nodes are changing, depending on the choice of γ, the equations corresponding to the open grid were solved for $N = 20$ and for different γ. The results are plotted in Figure 7.4 where each contour illustrates the positions of each node versus γ.

Another idea used in [21] is the concept of fictitious points, which is simply to augment a grid with additional nodes at which the function values are not directly known nor updated. This yields an interpolant that is used only in the interior of the extended interval. To illustrate this, we construct a grid by taking a 10-node open grid

for $\gamma = 0.35$ and by adding to it one fictitious point per side of the interval by reflecting the outer points about ± 1. Then, we plot the interpolation remainder for this grid and compare it with the one of the corresponding Chebychev grid ($N = 10$ and open grid) in Figure 7.5. It is seen that the fictitious point grid has a decreased error even though the minimum spacing between true points has increased by approximately a factor of 1.5.

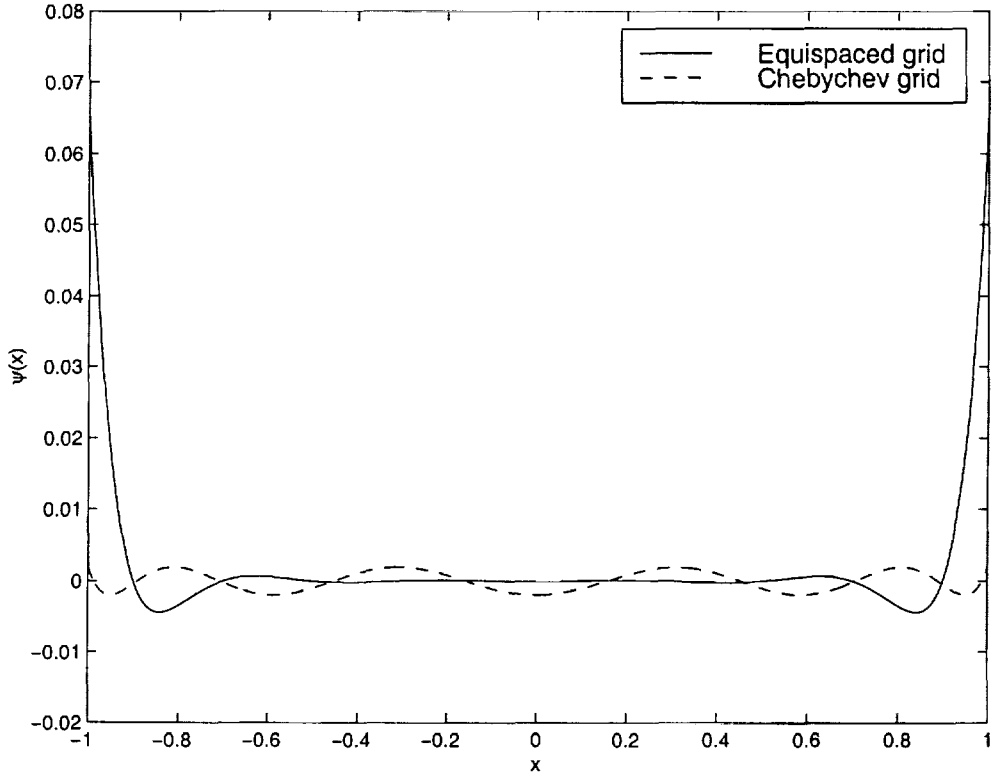

Figure 7.3: Interpolation remainder for N = 10.

IV. Multi-domain

In this section the multi-domain approach proposed by Driscoll in [21] is presented. The formulation will not be presented here but only briefly discussed. Basically, this multi-domain method breaks the domain under analysis into a number of sub-domains. The grid of each sub-domain is constructed by an interior node distribution (open grid) and m fictitious points determined by reflection of grid points about the boundaries of the sub-domain. The values of the fields at the fictitious points

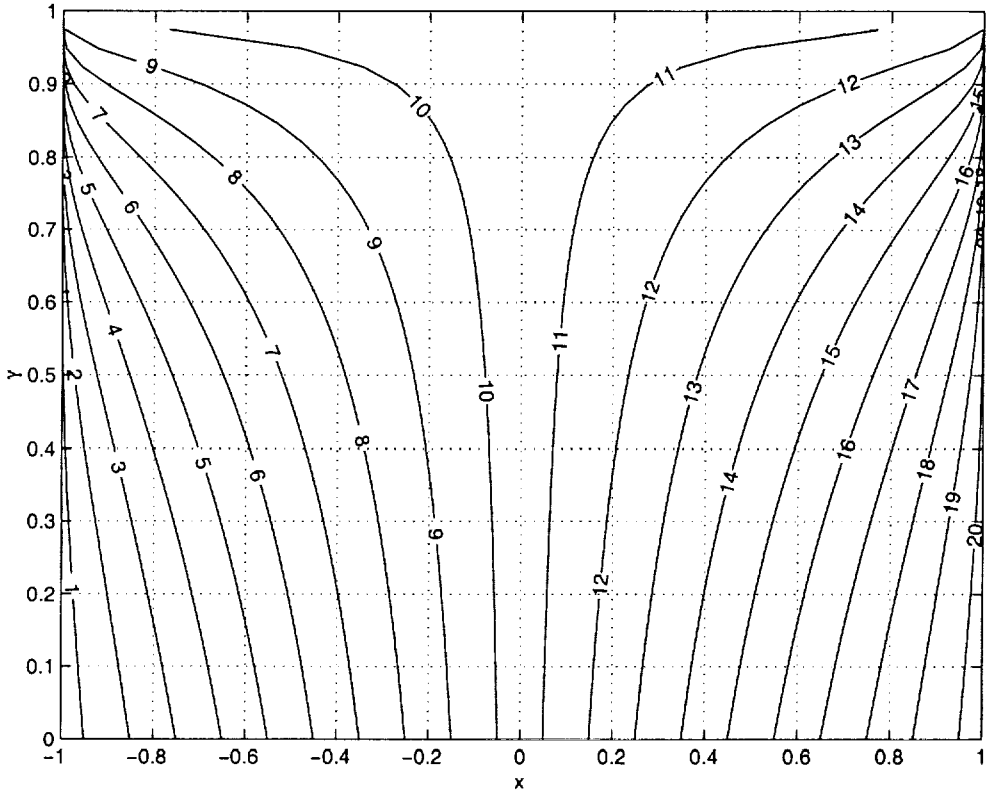

Figure 7.4: Positions of the nodes for different γ and for $N = 20$.

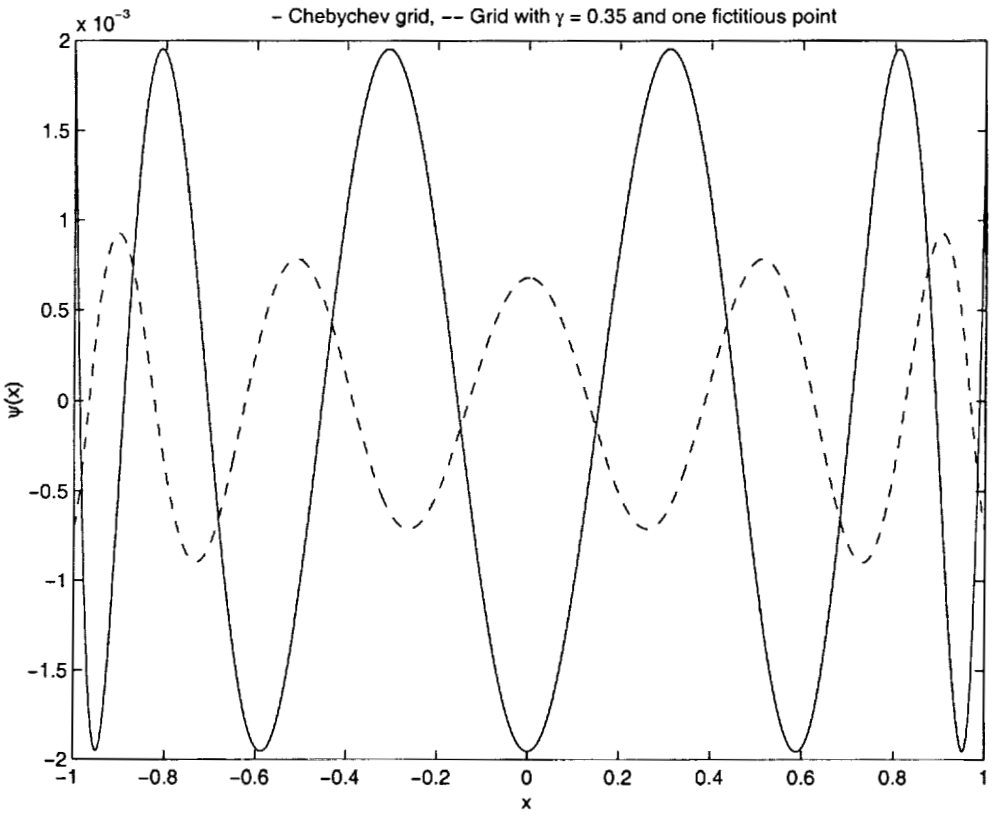

Figure 7.5: Interpolation remainder for N = 10.

are determined by enforcing certain conditions, such as the continuity of the fields, their first time derivative, etc., or by enforcing the boundary conditions known by electromagnetic theory in case the boundary occurs between two different media. Details of the approach are described in [21].

The multi-domain approach has the advantage of using smaller differentiation matrices and a larger time-step because each sub-domain is formed by a number of points considerably smaller than the one of the entire domain method. Note that in all the numerical simulations illustrated in this section one fictitious point per side of a subdomain is used.

The first numerical experiment was based on a three sub-domain code which was written for validation. The entire free-space computational domain was divided into three sub-domains and a pulse was excited at the left boundary of the domain. The right boundary of the domain was terminated with PEC. A sample of the computations is shown in Figure 7.6 where different frames of the propagating pulse, as well as the reflected one by the PEC, are shown. It seems that the coupling of the sub-domains was successfully implemented and there are no spurious reflections occurring at the interfaces. Here, a 17-node Chebychev grid was used in each subdomain (including the fictitious points). The matching of the sub-domains (related to the determination of the field values at the fictitious points) at each interface was implemented such that it was dependent on the matching at other interfaces. The same experiment was also performed with the matching between two neighbor subdomains (related to the determination of the field values at the fictitious points) not being dependent on the matching at other interfaces. The computations are shown in Figure 7.7 where different frames of the propagating pulse, as well as the reflected one by the PEC, are shown. It is observed that both approaches of matching the interfaces give very similar results. Therefore, for the following experiments it is chosen to do the matching at each interface independently of the others. This makes the coding of a general sub-domain program much more simple and practical.

The next simulation examines a 1-D domain divided into two sub-domains where one is free-space and the other one is PML. This is done to investigate how coupling between two sub-domains with different material properties is done. Following again the method proposed in [21], continuity of the fields as well as of their first time

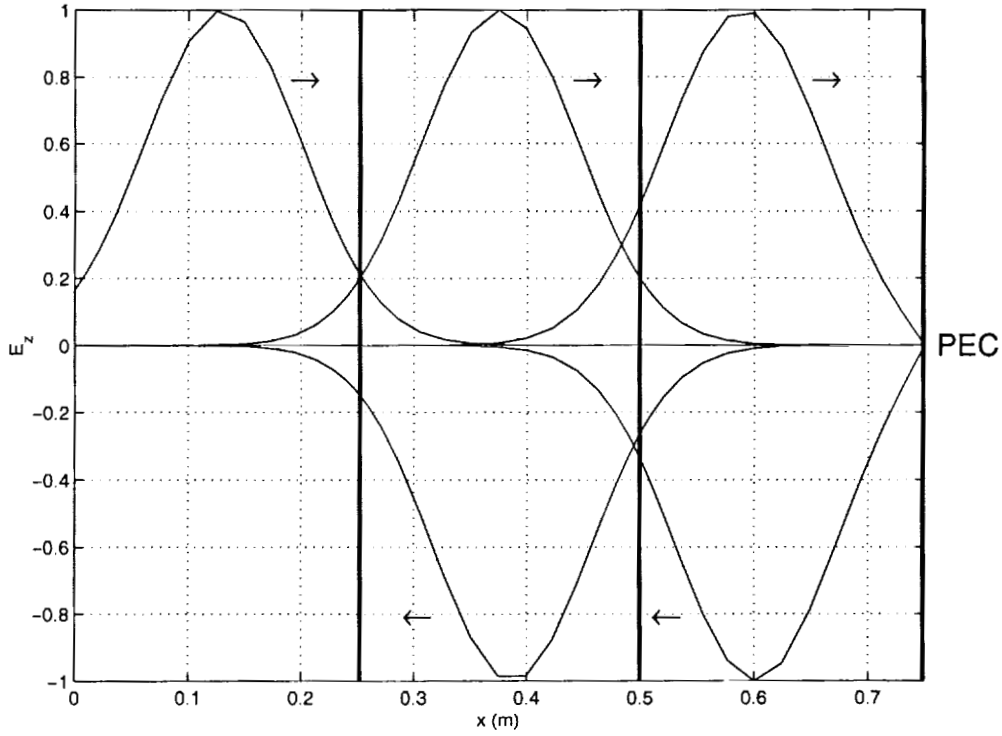

Figure 7.6: Traveling pulse in 1-D domain terminated with PEC (matching at one interface depends on the others).

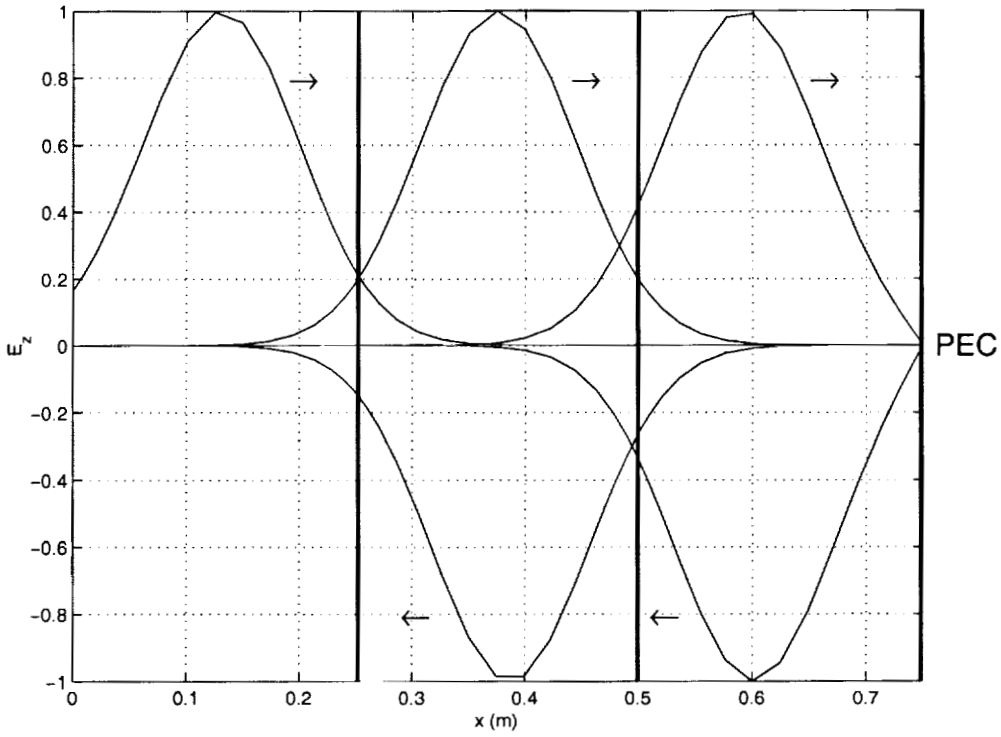

Figure 7.7: Traveling pulse in 1-D domain terminated with PEC (matching at one interface is independent of the others).

derivative is enforced because the PML has the same permittivity ϵ and permeability μ with the free-space. However, in this case the continuity conditions are more complicated than the ones in the case of materials with no magnetic or electric conductivity. The reason is that in this case these conditions now involve both E and H fields coupled in the same equations. A sample of the simulation results are shown in Figure 7.8 where different frames of the propagating pulse are shown. As expected, when the pulse enters the PML it gets absorbed without creating any reflections.

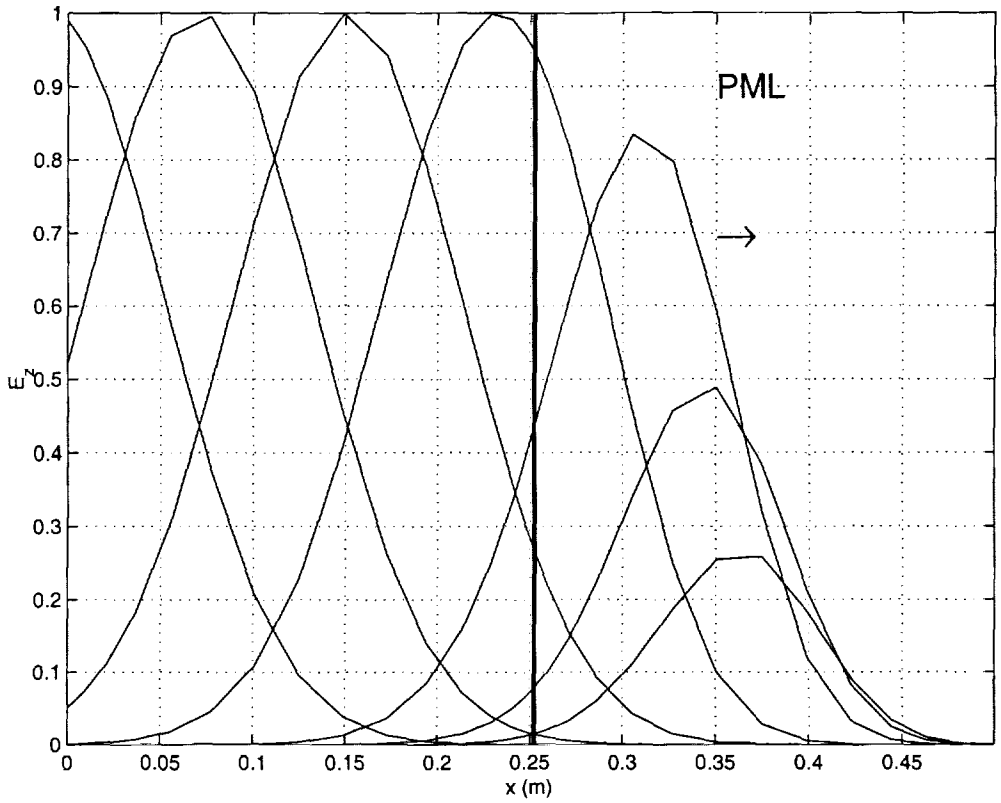

Figure 7.8: Traveling pulse in 1-D domain terminated with PML.

Finally a general multi-domain code was written that can divide a domain into a number of sub-domains which have the same number of points. This code works only for homogeneous regions, i.e., all sub-domains must have the same material properties in addition to zero electric and magnetic conductivities. However, the code can be generalized for different types of materials. To illustrate the high accuracy of the Chebychev collocation method, a free-space domain was analyzed. The domain was two meters long and was excited at the left boundary with a Gaussian pulse that

had significant frequency components up to 1.5 GHz (10% bandwidth). On the right boundary the domain was terminated on PEC, but the simulation time was chosen so that the pulse does not reach this end creating reflections. This problem was analyzed first using the Chebychev collocation method for a different number of subdomains and grid points, and second, using a second-order accurate FDTD scheme. The results are shown in Figure 7.9 and we observe that additional subdomains do not necessarily provide better accuracy. Also, the high accuracy of the spectral methods compared to the second-order FDTD scheme is again observed.

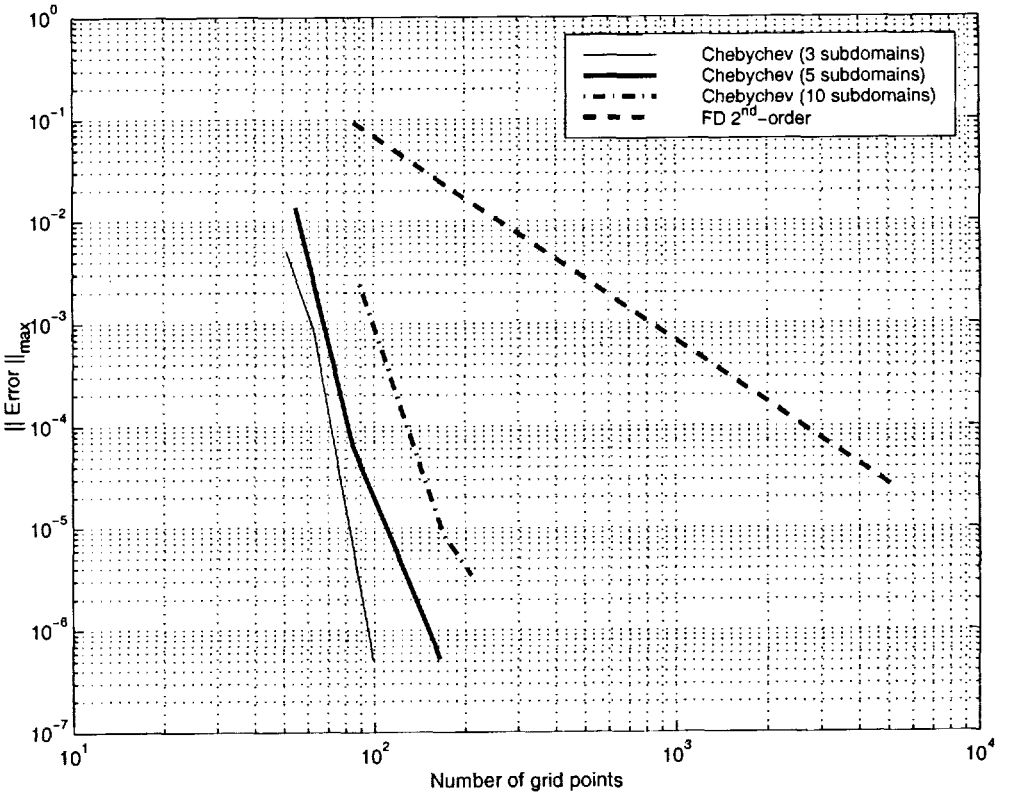

Figure 7.9: Maximum error in the solution of the 1-D TM mode.

V. Conclusions

In this report, spectral methods have been applied for the first time in the context of electromagnetics. The 1-D Maxwell's equations were successfully solved by these methods, and the PML was used to simulate open-space problems. The numerical

simulations illustrated that spectral methods outperform the standard FDTD algorithm in terms of accuracy, as they exhibit exponential convergence, i.e., the error drops exponentially as the number of discretization points increases. Furthermore, these methods exhibit negligible dispersion and therefore can simulate accurately electrically large domains. The main drawback of them is their restrictive stability criteria which require a very small time-step in order for them to be stable. However, there have been a few proposed methods that deal successfully with this problem and accomplish to relax the time-step restrictions.

Moreover, the concepts of interior domain grids and fictitious points were introduced. These principles were applied in the multi-domain formulation that was presented. A multi-domain approach has the advantage of using smaller differentiation matrices and it can also use larger time-step due to the fact that each sub-domain is formed by a number of points considerably smaller than the one of the entire domain method. This can lead to computational savings as a significantly larger time-step can be used without substantial loss of accuracy.

The spectral methods seem to be very promising for the analysis of electromagnetic problems. They can handle efficiently large domains because of their high accuracy, exponential convergence, and negligible dispersion and dissipation. Our ultimate goal is to apply and extend these methods initially to generic 2-D and 3-D problems and then to radiation problems.

Bibliography

[1] S. V. D. Berghe *et al.*, "Accurate modeling of thin conducting conducting layers in fdtd.," *IEEE Microwave and Guided Wave Letters*, vol. 8, pp. 75–77, February 1998.

[2] M. Robinson, T. Benson, C. Christopoulos, J. Dawson, M. Ganley, A. Marvin, S. Porter, and D. Thomas, "Analytical formulation for the shielding effectiveness of enclosures with apertures," *IEEE Trans. Electromagn. Comp.*, vol. 40, pp. 240–247, Aug. 1998.

[3] D. M. Sheen, S. M. Ali, M. D. Abouzahra, and J. A. Kong, "Application of the three-dimensional finite-difference time-domain method to the analysis of planar microstrip circuits," *IEEE Trans. Microwave Theory Tech.*, vol. 38, no. 7, pp. 849–857, 1990.

[4] J. G. Maloney, G. S. Smith, and W. R. Scott, Jr., "Accurate computation of the radiation from simple antennas using the finite-difference time-domain method," in *IEEE Antennas and Propagat. Soc. Int. Symposium*, (San Jose, CA), pp. 42–45, 1989.

[5] M. A. Jensen and Y. Rahmat-Samii, "Performance analysis of antennas for hand-held transceivers using FDTD," *IEEE Trans. Antennas Propagat.*, vol. 42, no. 8, pp. 1106–1113, 1994.

[6] R. Luebbers, L. Chen, T. Uno, and S. Adachi, "FDTD calculation of radiation patterns, impedance, and gain for a monopole antenna on a conducting box," *IEEE Trans. Antennas Propagat.*, vol. 40, no. 12, pp. 1577–1583, 1992.

[7] V. Jandhyala, E. Michielssen, and R. Mittra, "FDTD signal extrapolation using the forward-backward autoregressive (AR) model," *IEEE Microwave Guided Wave Lett.*, vol. 4, no. 6, pp. 163–165, 1994.

[8] J. Chen, C. Wu, T. K. Y. Lo, K.-L. Wu, and J. Litva, "Using linear and nonlinear predictors to improve the computational efficiency of the FD-TD algorithm," *IEEE Trans. Microwave Theory Tech.*, vol. 42, no. 10, pp. 1992–1997, 1994.

[9] A. Reineix and B. Jecko, "Analysis of microstrip patch antennas using finite difference time domain method," *IEEE Trans. Antennas Propagat.*, vol. 37, no. 11, pp. 1361–1369, 1989.

[10] M. Piket-May, A. Taflove, and J. Baron, "FD-TD modeling of digital signal propagation in 3-D circuits with passive and active loads," *IEEE Trans. Microwave Theory Tech.*, vol. 42, no. 8, pp. 1514–1523, 1994.

[11] R. J. Luebbers and H. S. Langdon, "A simple feed model that reduces time steps needed for FDTD antenna and microstrip calculations," *IEEE Trans. Antennas Propagat.*, vol. 44, no. 7, pp. 1000–1005, 1996.

[12] A. Polycarpou, *Finite-Element Analysis of Microwave Passive Devices and Ferrite Tuned Antennas.* PhD thesis, Arizona State University, 1998.

[13] S. M. Rao, D. R. Wilton, and A. W. Glisson, "Electromagnetic scattering by surfaces of arbitrary shape," *IEEE Trans. on Antennas and Propagation*, vol. AP-30, pp. 409–418, May 1982.

[14] K. McInturff and P. S. Simon, "The Fourier transform of linearly varying functions with polygonal support," *IEEE Trans. Antennas Propagat.*, vol. AP-39, pp. 1441–1443, Sep. 1991.

[15] J. T. Aberle, "Spectral domain method of moments," June 1994. Personal notes.

[16] J. M. Jin, *The Finite Element Method in Electromagnetics.* New York: Wiley, 1993.

[17] C. A. Balanis, *Advanced Engineering Electromagnetics.* New York: Wiley, 1989.

[18] P. Y. Ufimtsev, "Approximate computation of the diffraction of plane electromagnetic waves at certain metal bodies. parti. diffraction pattern at a wedge and a ribbon," *Zh. Tekhn. Fiz. (USSR)*, vol. 27, pp. 1708–1718, 1957.

[19] K. M. Pasala, "Closed-form expression for nonuniform currents on a wedge illuminated by tm plane wave," *IEEE Trans. on Antennas and Propagation.*, vol. 36, pp. 1753–1759, Dec. 1988.

[20] P. H. Pathak and R. G. Kouyoumjian, "An analysis of the radiation from aperture in curved surfaces by the geometrical theory of diffraction," *IEEE Trans. on Antennas and Propagation.*, vol. 62, pp. 1438–1447, Nov. 1974.

[21] T. A. Driscoll and B. Fornberg, "A block pseudospectral method for maxwell's equations: I. one dimensional case.," *J. Comput. Phys.*, vol. 140, pp. 47–65, 1998.

[22] B. Engquist and A. Majda, "Absorbing boundary conditions for the numerical simulation of waves," *Math. Comp.*, vol. 31, pp. 629–651, 1977.

[23] J.-P. Berenger, "A perfectly matched layer for the absorption of electromagnetic waves," *J. Comput. Phys.*, vol. 114, no. 1, pp. 185–200, 1994.